Investigation of laser-induced structures on metal surfaces produced via two-beam and laser-plasmon interference

Dissertation
zur Erlangung des mathematisch-naturwissenschaftlichen
Doktorgrades

"Doctor rerum naturalium"

der Georg-August-Universität Göttingen

im Promotionsstudiengang "Physik"
der Georg-August University School of Science (GAUSS)

vorgelegt von
Jens Oltmanns

aus Norden
Göttingen, 2022

Betreuungsausschuss

apl. Prof. Dr. Alexander Egner
(Institutsdirektor, Institut für Nanophotonik Göttingen e.V.)

Prof. Dr. Claus Ropers
(Direktor, Max-Planck-Institut für Multidisziplinäre Naturwissenschaften)

Dr. Peter Simon
(Abteilungsleiter Kurze Pulse/Nanostrukturen,
Institut für Nanophotonik Göttingen e.V.)

Mitglieder der Prüfungskommission

Referent: apl. Prof. Dr. Alexander Egner
(Institutsdirektor, Institut für Nanophotonik Göttingen e.V.)

Korreferent: Prof. Dr. Hans-Christian Hofsäss
(II. Physikalisches Institut, Georg-August-Universität Göttingen)

Weitere Mitglieder der Prüfungskommission:

Prof. Dr. Claus Ropers
(Direktor, Max-Planck-Institut für Multidisziplinäre Naturwissenschaften)

Prof. Dr. Stefan Mathias
(I. Physikalisches Institut, Georg-August-Universität Göttingen)

Prof. Dr. Angela Rizzi
(VI. Physikalisches Institut, Georg-August-Universität Göttingen)

Dr. Peter Simon
(Abteilungsleiter Kurze Pulse/Nanostrukturen,
Institut für Nanophotonik Göttingen e.V.)

Tag der mündlichen Prüfung: 09. Dezember, 2022

Zusammenfassung

Mithilfe periodischer Strukturen lassen sich die Eigenschaften einer Oberfläche vielfältig verändern, dabei hängt es stark von der Art der Strukturen ab, welche Eigenschaften die Materialoberfläche annimmt.
In dieser Arbeit geht es um die Erzeugung von periodischen Strukturen auf Metalloberflächen mit Hilfe von Ultrakurzpulslasern. Dabei werden sowohl deterministische Strukturen durch Überlagerung miteinander interferierender Strahlen, wie auch Rippelstrukturen (eng. Laser-induced periodic surface structures, LIPSS) durch eine einfache Bestrahlung, generiert.
Im Folgenden wird auf beide Methoden eingegangen und die Eigenschaften der jeweils erzeugten Strukturen untersucht. Dabei werden externe Parameter wie die Wellenlänge des Lichts, die Pulsdauer, die Energieverteilung, als auch das Umgebungsmedium variiert und die Veränderungen der Strukturen untersucht.
Zusätzlich werden die Ergebnisse mit Simulationen verglichen, um die zugrundeliegenden Prozesse der Strukturierung besser zu verstehen.
Unter festen und flüssigen transparenten Deckschichten unterschiedlicher Dicke wurden Strukturen auf Gold durch Zweistrahlinterferenz erzeugt. Dabei wurde ein Femto- und ein Pikosekundenlaser verwendet. Es zeigt sich, dass Strukturen unter einer transparenten Deckschicht eine geringere Höhe der Strukturen und weniger Debris aufweisen. Für den Femtosekunden-Puls unter flüssiger Deckschicht zeigte sich eine inhomogene Strukturverteilung, was auf die Entstehung einer Druckblase in der Deckschicht zurückgeführt werden kann, die die entstehenden Strukturen nach unten und zur Seite. Bei Pikosekunden-Pulsen und bei fester Deckschicht bildeten sich homogene Strukturen.
Ebenfalls wurden mit Femtosekunden-Pulsen unterschiedlicher Wellenlänge (UV, grün, IR) Rippelstrukturen auf Gold erzeugt, auch hier mit und ohne transparente Deckschicht. Es zeigt sich, dass die Eigenschaften der erzeugten Strukturen gut mit der Plasmonentheorie erklärbar sind, was einen weiteren Hinweis dafür liefert, dass LIPSS als Ergebnis einer Interferenz zwischen SPP und dem einfallenden Licht entstehen. Außerdem wird eine Methode vorgestellt, um die Höhenverteilung der Strukturen zu verändern.

Abstract

Periodic surface structures can change the properties of material surfaces. The obtained various functionalities strongly depend on the type of the specific structures. This work deals with the generation of periodic structures on metal surfaces using ultrashort pulse lasers. Both, deterministic structures by superposition of mutually interfering beams, as well as ripple structures (laser-induced periodic surface structures, LIPSS) by a single beam irradiation, are generated and the resulting structures are evaluated.

The parameters such as the wavelength of the laser, the pulse duration, the fluence distribution and the surrounding medium are changes in the experiments and the changes in the structures analysed.

In addition, the experimental findings are compared to simulation results to understand the fundamental processes of the structure formation.

Structures were obtained using single pulse interference patterning on gold under solid and liquid confinement layers with different thicknesses. Femtosecond and picosecond laser pulses are used. The structures forming under the confinement layer have a smaller height and less debris. The height distribution under the liquid confinement layer are inhomogeneous when using the femtosecond pulse, attributed to a pressure bubble in the confinement layer, which is pushing the developing structures down- and sidewards. But with the picosecond pulse and under the solid layer the structures are homogeneous.

LIPSS were produced on a gold surface using femtosecond pulses at different wavelengths (UV, green, IR), also with and without a confinement layer. The measured properties of the structures are in accordance with those predicted by the plasmonic theory, thus providing further evidence that LIPSS emerge as a result of interference between SPP and the incoming light. Furthermore, a method of controlling the structure heights is presented.

Contents

1. Introduction

Technological developments lead to a requirement for special properties of the used materials. One method known to modify specific material properties is the structuring of their surfaces. In particular, periodic surface structures are known to provide versatile functionalities. Though, depending on the wanted properties very specific changes of the surface may be needed.
In the realm of periodic nano-structuring of surfaces, there are two methods that mainly use ultrashort laser pulses. These are interference techniques [1, 2] and laser-induced periodic surface structures (LIPSS) [3].
The interference techniques rely on interfering laser beams to produce a periodic intensity pattern on a samples surface. This pattern, given the right fluence, imprints periodic structures on the surface. In this case, the period of the structures is determined by the wavelength of the laser beam, as well as the angle at which the beams interfere. As the period in this method does not depend on the sample itself, this method will be called two-beam interference method.
The other method of surface structuring was developed after the findings of Birnbaum [4] in 1965, where periodic structures appeared on a germanium surface after irradiating it with a single laser beam. These structures are called LIPSS. Though, a universal explanation of LIPSS is not found, many LIPSS on metals are attributed to an interference between the laser beam and a coherent electron oscillation, called surface plasmon polariton (SPP). The period of these structures does also depend on the wavelength of the laser and the angle of incidence, but also on the number of pulses, the material parameters and the environment of the sample.
Plasmons themselves are already established and widely used in a field called Plasmonics, using plasmons for various technical applications. These contain on-chip optical computing [5–7], nano-antennas [8, 9], wireless communication [10–13], wave guides [14, 15] and others [16]. These applications require only low laser energies and thus there are no permanent changes of the surface morphology, therefore no LIPSS are produced.

Also the introduction of permanent changes on the surface have a wide range of applications. There are rather coarse treatments, like laser cutting [17, 18], drilling [19, 20] and welding [21] or more filigree treatments concerning nanostructures. For the production of nanostructures, often the used lasers have a small wavelength and a short pulse duration.
Nanostructuring with lasers is most often done using one of the above mentioned methods. The properties of the sample with the structures are not reliant by the method of production. So are the structures from two-beam interference used for the production of hydrophobic surfaces [22–24], diffractive colouring surfaces [25], as well as to control cell growth on surfaces [26] and change the tribological properties of a surface [27]. Just like the usages of LIPSS which also include hydrophobic surfaces [28, 29], diffractive colouring [30–33], cell growth [34] and tribology [33].
Though the method of production is not of importance, the topological properties of the surface structures greatly influence the resulting functionalities. As an example, the contact angle of water on a material first increases with the depth of the surface structures, but decreases again for deeper structures [35]. Also do different cell types react differently to specific structures and on different materials [36].
In this work the properties of structures produced by both methods, two-beam interference and LIPSS are investigated, which form on metal surfaces. In case of the two-beam interference method, structures forming under a transparent confinement layer are also investigated. The LIPSS are compared to the predictions from the plasmonic theory, as well as possible ways of altering the structures are presented.
Overall this work aims to present different ways how periodic surface structures may be produced and manipulated as well as making it possible to predict the resulting structure parameters for a given experiment.
The work is structured as follows. In Chapter 2, the theoretical background for the used methods will be explained. This is starting with describing the interactions between light and matter via the Maxwell equations and the materials response through the dielectric function. Here also the three basic forms of interaction between light and matter, reflection, transmission and absorption are described. Afterwards, the Maxwell equations are used to describe SPPs. In the next section of this chapter, the phenomenon of LIPSS is introduced and the different types of LIPSS are differentiated and theories trying to explain the phenomenon are presented.
The following section explains the reflectrometric thin film analysis and its usage. Afterwards the interactions of laser with matter are described, with an additional

focus on periodic laser structuring. The last section of this chapter gives an overview over the structuring process under a transparent confinement layer.
In Chapter 3 the formerly developed resources are presented that were used in the experiments. The chapter starts with presenting the laser sources, "Pharos" and "Hyper Rapid" and the important parameters of the two systems. In the next section, the frameworks of the simulations are shortly explained, together with the underlying principles. The chapter concludes with a short description of the microscopes (scanning electron microscope and the atomic force microscope) used for the analysis of the sample.
Chapter 4 presents the setups for performing the experiments. It begins with the experimental setup for producing the structures using the two-beam interference technique. Included in this section is a description of the sample observation during the experiments, used to position the sample and view the surface.
Than the setup constructed for investigating the LIPSS is discussed. As these experiments are done using different wavelengths of the light source, two different beams lines were needed. The last section in this chapter contains the film thickness measurement setup, that was used based on the concepts described in Chapter 2. Afterwards a short characterisation of the used samples is given concerning the different layers and the surface properties of the samples, as well as material properties at the used wavelengths in the experiments. Chapter 5 presents the results of the experiments creating periodic structures using the two-beam interference method under transparent confinement layers. The first section discusses the results of two-beam interference experiments under a thin liquid layer. Thereby, the two different laser sources are used, which differ in the pulse duration. The next section contains the results using the two-beam interference method to produce structures under a thin solid SiO_2 layer and again determine the influence of the layer as well as the pulse duration, by using both laser sources.
Chapter 6 includes the results of the LIPSS experiments. The presented results obtained by the short wavelength and small pulse duration and are compared with simulations of the structuring process. This provides evidence of the plasmonic nature of LIPSS. Afterwards the fluence dependence of the period of the structures for all wavelengths are presented. Also the influence of the beam profile in evaluated and a possible way of shaping the beam for more homogeneous structures is presented. In the end, also the LIPSS forming under confinement layers are evaluated.
The last Chapter 7 contains the conclusion of the findings in this work.

2. Theoretical Background

2.1. Light-Matter Interaction

In this section the principles necessary to explain the interactions between light and matter will be presented. The first subsections shows the Maxwell equations, which describe the behaviour of electromagnetic waves. The original equations are only valid in vacuum but can be modified to describe the interactions of light and matter. Afterwards, based on the Maxwell equations the theory of surface plasmon polaritons will be discussed. In the next section, the phenomenon of creating laser-induced periodic surface structures will be presented and different theories shown, aiming at explaining the origin of these structures, with the main emphasis on surface plasmon polaritons.
The following section explains the principles behind the reflectrometric thin film analysis that may be used to measure the thickness of thin transparent layers. Afterwards, structure formation on metals after irradiation with lasers will be described with the last section presenting the results, when the irradiation is performed under a confinement layer.

2.1.1. Maxwell Equations

A fundamental description of the interaction between light and matter is given by the Maxwell equations. This chapter is based on [16, 37, 38], a more in-depth treatment of the topic can be found in that sources.
The Maxwell equations are a set of four equations describing the behaviour of components of the electric field $\mathbf{E}$ and the magnetic induction field $\mathbf{B}$. The microscopic

Maxwell equations read as

$$\nabla \cdot \mathbf{E} = \frac{\rho}{\epsilon_0} \tag{2.1}$$

$$\nabla \cdot \mathbf{B} = 0 \tag{2.2}$$

$$\nabla \times \mathbf{E} = -\frac{\partial \mathbf{B}}{\partial t} \tag{2.3}$$

$$\nabla \times \mathbf{B} = \mu_0 \mathbf{j} + \mu_0 \epsilon_0 \frac{\partial \mathbf{E}}{\partial t}, \tag{2.4}$$

with ρ and $\mathbf{j}$ being the charge and current density, respectively. The constants ϵ_0 and μ_0 are the vacuum permittivity and permeability. The vacuum permittivity and permeability connect to the speed of light in vacuum c via

$$c = \frac{1}{\sqrt{\epsilon_0 \mu_0}}. \tag{2.5}$$

The microscopic Maxwell equations are used mainly to describe electromagnetic phenomena in vacuum, but it is also possible to describe effects in matter as well. Then the response of each molecule has to be taken into account, therefore one often uses the macroscopic Maxwell equations. For the transition form the microscopic to the macroscopic view, two additional fields are introduced, which contain the responses of the material. These fields are the polarisation $\mathbf{P}$ and the magnetisation $\mathbf{M}$.

In the presence of an electric field the bound charges of the material form a polarisation as response, therefore it makes sense to split the charge and current density into a bound and a free part, thus

$$\rho = \rho_f + \rho_b \tag{2.6}$$

$$\mathbf{j} = \mathbf{j}_f + \mathbf{j}_b. \tag{2.7}$$

The bound charge density is than defined via

$$\rho_b = -\nabla \mathbf{P}. \tag{2.8}$$

Combining the equations 2.1, 2.6 and 2.8 one obtains

$$\nabla \cdot \mathbf{E} = \frac{\rho_f + \rho_b}{\epsilon_0} = \frac{\rho_f - \nabla \cdot \mathbf{P}}{\epsilon_0}. \tag{2.9}$$

Now one may combine the electric field and polarisation to the electric displacement

$$\mathbf{D} = \epsilon_0 \mathbf{E} + \mathbf{P}, \tag{2.10}$$

which may be used to rewrite 2.9 as

$$\nabla \cdot \mathbf{D} = \rho_f. \tag{2.11}$$

A similar distinction may be done for the current density, with the bound current density coming from the magnetisation as well as the temporal change of the polarisation

$$\mathbf{j}_b = \nabla \times \mathbf{M} + \frac{\partial \mathbf{P}}{\partial t}, \tag{2.12}$$

thus the total current density containing a bound and free part is given by

$$\mathbf{j} = \mathbf{j}_f + \mathbf{j}_b = \mathbf{j}_f + \nabla \times \mathbf{M} + \frac{\partial \mathbf{P}}{\partial t}. \tag{2.13}$$

Inserting 2.13 into the Maxwell equation 2.4 and identifying the electric displacement 2.10 leads to the equation

$$\nabla \times \left(\frac{\mathbf{B} - \mathbf{M}}{\mu_0} \right) = \mathbf{j}_f + \frac{\partial \mathbf{P}}{\partial t}. \tag{2.14}$$

Defining the magnetic field $\mathbf{H}$ as

$$\mathbf{H} = \frac{\mathbf{B} - \mathbf{M}}{\mu_0}, \tag{2.15}$$

equation 2.14 becomes

$$\nabla \times \mathbf{H} = \mathbf{j}_f + \frac{\partial \mathbf{D}}{\partial t}. \tag{2.16}$$

Together with 2.2 and 2.3, the equations 2.11 and 2.16 form the macroscopic Maxwell equations

$$\nabla \cdot \mathbf{D} = \rho_f \tag{2.17}$$

$$\nabla \cdot \mathbf{B} = 0 \tag{2.18}$$

$$\nabla \times \mathbf{E} = -\frac{\partial \mathbf{B}}{\partial t} \tag{2.19}$$

$$\nabla \times \mathbf{H} = \mathbf{j}_f + \frac{\partial \mathbf{D}}{\partial t}. \tag{2.20}$$

In the following the indices "f" and "b" will be generally dropped and only used when necessary.

Fourier Transformed Maxwell-Equations

When working with the Maxwell equations, it is often useful to formulate them using the Fourier transformation. The formula for a Fourier transformation from the time to the frequency domain for an arbitrary field A is

$$\tilde{A}(\mathbf{r},\omega) = \frac{1}{2\pi}\int_{-\infty}^{\infty} A(\mathbf{r},t)\exp^{i\omega t}\, dt. \tag{2.21}$$

This procedure may be done with the time dependent variables in the Maxwell equations, the fields $\mathbf{E}, \mathbf{B}, \mathbf{D}$, and $\mathbf{H}$ as well as the charge and current ρ and $\mathbf{j}$. The equations 2.17-2.20 in the frequency domain have the form

$$\nabla \cdot \tilde{\mathbf{D}}(\mathbf{r},\omega) = \tilde{\rho}(\mathbf{r},\omega) \tag{2.22}$$

$$\nabla \cdot \tilde{\mathbf{B}}(\mathbf{r},\omega) = 0 \tag{2.23}$$

$$\nabla \times \tilde{\mathbf{E}}(\mathbf{r},\omega) = i\omega\tilde{\mathbf{B}}(\mathbf{r},\omega) \tag{2.24}$$

$$\nabla \times \tilde{\mathbf{H}}(\mathbf{r},\omega) = \tilde{\mathbf{j}}(\mathbf{r},\omega - i\omega)\tilde{\mathbf{D}}(\mathbf{r},\omega) \tag{2.25}$$

The inverse Fourier transformation back from the frequency to the time domain takes the form

$$A(\mathbf{r},t) = \frac{1}{2\pi}\int_{-\infty}^{\infty} \tilde{A}(\mathbf{r},\omega)\exp^{i\omega t}\, d\omega. \tag{2.26}$$

2.1.2. Dielectric Functions

For calculating the response of a material to external electric and magnetic field, the electric susceptibility χ_e and magnetic susceptibility χ_m are introduced. When limiting oneself to only linear terms of the susceptibilities one may link the polarisation and magnetisation to the electric and magnetic field via

$$\mathbf{P} = \chi_e \epsilon_0 \mathbf{E} \tag{2.27}$$

$$\mathbf{M} = \chi_m \mathbf{H}. \tag{2.28}$$

Inserting 2.27 into equation 2.10 and 2.28 into equation 2.15 one gets

$$\mathbf{D} = \epsilon_0\mathbf{E} + \mathbf{P} = \epsilon_0\mathbf{E} + \chi_e\epsilon_0\mathbf{E} = \epsilon_0(1+\chi_e)\mathbf{E} = \epsilon_0\epsilon\mathbf{E} \tag{2.29}$$

$$\mathbf{B} = \mu_0(\mathbf{H} + \mathbf{M}) = \mu_0(\mathbf{H} + \chi_m\mathbf{H}) = \mu_0(1+\chi_m)\mathbf{H} = \mu_0\mu_r\mathbf{H}, \tag{2.30}$$

with the dielectric constant ϵ and relative permeability μ_r. For non-magnetic elements like gold $\mu_r = 0$.
For interactions with light the dielectric constant ϵ is strongly dependent on the frequency, therefore the term "constant" is misleading and in the following it will be called dielectric function.
In general, the dielectric function is a complex function dependent on the frequency or wavelength of the electromagnetic wave and can be written as

$$\epsilon(\omega) = \epsilon_1((\omega)) + \mathrm{i}\epsilon_2((\omega)), \tag{2.31}$$

where ω is the angular frequency of the light and ϵ_1 and ϵ_2 the real and imaginary part of the dielectric function, respectively. Many optical properties are related to the dielectric function of a material.

Reflectivity, Absorption and Transmission

The complex refractive index $\tilde{n} = n + \mathrm{i}k$ is defined as $\tilde{n} = \sqrt{\epsilon}$, where n and k are the refractive index and extinction coefficient, respectively. These quantities are given by the dielectric function as:

$$n = \sqrt{\frac{|\epsilon| + \mathrm{Re}\ \epsilon}{2}} = \frac{\epsilon_1}{2} + \frac{1}{2}\sqrt{\epsilon_1^2 + \epsilon_2^2} \tag{2.32}$$

$$\kappa = \sqrt{\frac{|\epsilon| - \mathrm{Re}\ \epsilon}{2}} = \frac{\epsilon_2}{2n}. \tag{2.33}$$

This is revertible to calculate the values of the dielectric function from the refractive index and extinction coefficient as

$$\epsilon_1 = n^2 - \kappa^2 \tag{2.34}$$

$$\epsilon_2 = 2nk. \tag{2.35}$$

The absorption of light in a material occurs via exponential attenuation described by Beer's law

$$I = I_0 \exp^{-\alpha z}, \tag{2.36}$$

with the intensity of the light I and the initial intensity given by I_0. The absorption coefficient α is related to the extinction coefficient via

$$\alpha = \frac{2\kappa\omega}{c}. \tag{2.37}$$

Once light interacts with a material, it can be partly reflected from the surface, absorbed in its volume and transmitted through it. The transmission T can be defined via the initial intensity of the light and the intensity after the material I_{trans} as

$$T = \frac{I_{\text{trans}}}{I_0}. \tag{2.38}$$

A part of the light is reflected at the surface of the material. The reflectivity R at the surface between vacuum and the material under normal incidence can be calculated via

$$R = \frac{(n-1)^2 + \kappa^2}{(n+1)^2 + \kappa^2} = \frac{I_{\text{ref}}}{I_0}, \tag{2.39}$$

with I_{ref} being the intensity of the reflected light.
The light can also be absorbed by the material. The absorption A of the material is given by

$$A = \frac{I_{\text{abs}}}{I_0} = 1 - R - T, \tag{2.40}$$

where I_{abs} is the absorbed intensity.

2.1.3. Two-Photon-Absorption

Besides the absorption process described by Beer's law, there is also the possibility of absorbing two photons simultaneously, a process called two-photon absorption (TPA). This process was first described by Maria Göppert-Meyer in 1931 [39]. The probability of this effect depends strongly on the number of photons and thus on the intensity of the beam. Due to this process, transparent materials can absorb energy at the radiation wavelength. This makes it possible to process transparent materials, but can also cause unwanted attenuation of a laser beam. The intensity

of light after travelling through a layer of thickness d is given by [40, 41]

$$I_1 = \frac{I_0(1-R)^2 \exp(-\alpha d)}{1 + \beta/\alpha \; I_0(1-R)[1-\exp(-\alpha d)]} \tag{2.41}$$

with I_0 the incident intensity, R the reflectivity of the layer and α and β the linear absorption and two photon absorption coefficients, respectively. As the intensity of the beam is given by

$$I = \frac{F}{t_p} \tag{2.42}$$

with F the fluence of the beam and t_p the pulse duration. At constant fluence, a beam with a shorter pulse duration has a higher intensity and is thus more strongly absorbed in a medium due to TPA.

2.2. Surface Plasmon Polariton

The phenomenon of surface plasmons (SP) was first discussed in the context of energy loss in thin metal films in a paper by Ritchie from 1957 [42]. Surface plasmon polaritons are quasi-particles that are propagating on the interface between a conducting and a dielectric medium and are decaying exponentially in both media. Assuming that there are no external charges and currents, it is possible to combine the equations 2.19 and 2.20 to the equation

$$\nabla \times \nabla \times \mathbf{E} = -\mu_0 \frac{\partial^2 \mathbf{D}}{\partial t^2}. \tag{2.43}$$

Using identities and equation 2.17, 2.43 is identical to

$$\nabla \left(-\frac{1}{\epsilon} \mathbf{E} \cdot \nabla \epsilon \right) - \nabla^2 \mathbf{E} = -\mu_0 \epsilon_0 \epsilon \frac{\partial^2 \mathbf{E}}{\partial t^2}. \tag{2.44}$$

Under the assumption that there is a negligible change of the dielctric function of the material in the order of the optical wavelength it can be approximated that

$$\nabla \epsilon = 0. \tag{2.45}$$

With that and using $\mu_0 \epsilon_0 = c^{-2}$, 2.44 becomes

$$\nabla^2 \mathbf{E} = \frac{\epsilon}{c^2} \frac{\partial^2 \mathbf{E}}{\partial t^2}, \tag{2.46}$$

which is the wave equation. Under the same assumptions it is possible to get the wave equation for the magnetic induction field

$$\nabla^2 \mathbf{B} = \frac{\mu}{c^2} \frac{\partial^2 \mathbf{B}}{\partial t^2}. \tag{2.47}$$

If the electric field is a harmonic function of time, meaning that the time variations are sinusoidal, it can be expressed in complex coordinates as

$$\mathbf{E}(\mathbf{r}, t) = \mathbf{E}(\mathbf{r}) \exp(-i\omega t), \tag{2.48}$$

with the angular frequency ω.
Inserting 2.48 into 2.47 leads to

$$\nabla^2\mathbf{E} + k_0^2\epsilon\mathbf{E}, \tag{2.49}$$

with $k_0 = \frac{\omega}{c}$.

TM-Mode (p-Polarisation)

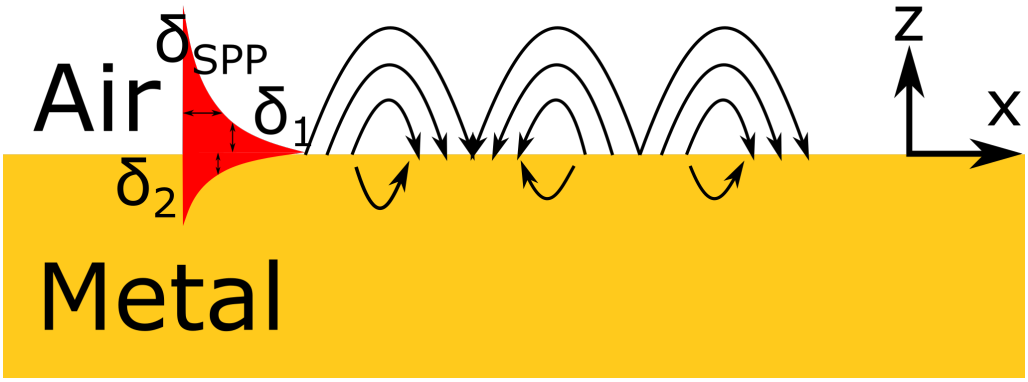

Figure 2.1.: Simplest geometry that allows the excitation of SPP propagation, showing an interface of a dielectric layer ($\epsilon_d < 0$) on a metal surface ($\epsilon_m > 0$). The SPP wave then propagates on the interface in x-direction. The damping of the SPP in each direction shown by δ_i, with $i = 1, 2$ in z-direction and $i =$ SPP in x-direction.

In case of p-polarised light, some components of the $\mathbf{H}$ and $\mathbf{E}$ fields are per definition zero. Under the conditions of a harmonic time dependence, propagation in x-direction and a homogeneous behaviour in y-direction, the fields have the form

$$\mathbf{H}_j = \begin{pmatrix} 0 \\ A_j \\ 0 \end{pmatrix} \exp(ik_{j,x}x + k_{j,z}z - i\omega t), \tag{2.50}$$

$$\mathbf{E}_j = \frac{A_j}{\omega\epsilon_j} \begin{pmatrix} k_{j,z} \\ 0 \\ k_{j,x} \end{pmatrix} \exp(ik_{j,x}x + k_{j,z}z - i\omega t), \tag{2.51}$$

where $j = d, m$ indicate the media in which the waves propagate, meaning either the dielectric medium or the metal and A is the amplitude of the wave in each medium. Due to momentum conservation in both media and with $k = \omega/c$ for the wave vector

in vacuum the following equations are obtained:

$$k_{d,x}^2 + k_{d,z}^2 = \epsilon_d k^2 \tag{2.52}$$

$$k_{m,x}^2 + k_{m,z}^2 = \epsilon_m k^2. \tag{2.53}$$

Also the in-plane wave vector is conserved, so

$$k_{d,x} = k_{m,x} = k_{\mathrm{SPP}} \tag{2.54}$$

For reasons of continuity, both field must be equal at the interface of the two media, therefore

$$A_d = A_m \tag{2.55}$$

$$A_d \frac{k_{d,z}}{\epsilon_d} = A_m \frac{k_{m,z}}{\epsilon_m} \tag{2.56}$$

so

$$\frac{k_{z,m}}{k_{z,d}} = \frac{\epsilon_m}{\epsilon_d}. \tag{2.57}$$

Now combining 2.52,2.53 and 2.57 leads to

$$k_{\mathrm{SPP}} = k\sqrt{\frac{\epsilon_m \epsilon_d}{\epsilon_m + \epsilon_d}} \tag{2.58}$$

which is the dispersion relation of the SPP wave.
Additionally, one can determine the wave vector component normal to the metal surface, which is given by

$$k_{z,j} = k\sqrt{\frac{\epsilon_j^2}{\epsilon_m + \epsilon_d}}. \tag{2.59}$$

The inverse of $|k_{j,z}|$ is the penetration depth δ of the SPP into the material

$$\delta_j = \frac{1}{|k_{j,z}|} = \frac{1}{k}\sqrt{\frac{\epsilon_j^2}{\epsilon_m + \epsilon_d}}. \tag{2.60}$$

As ϵ_m and ϵ_d are complex numbers, k_{SPP} will also be complex and can be written as

$$k_{\mathrm{SPP}} = k_x' + ik_x''. \tag{2.61}$$

TE-Mode (s-Polarisation)

In case of s-polarised light, the ansatz is the same as for p-polarised light. In the case of s-polarised light, the non-zero components are E_y, as well as H_x and H_z. Written out the field have the form

$$\mathbf{E}(\mathbf{r},t) = \begin{pmatrix} 0 \\ A_j \\ 0 \end{pmatrix} \exp(ik_x x + k_z z - i\omega t), \tag{2.62}$$

$$\mathbf{H}(\mathbf{r},t) = \frac{A_j}{\omega} \begin{pmatrix} -k_z \\ 0 \\ k_x \end{pmatrix} \exp(ik_{j,x} x + k_{j,z} z - i\omega t). \tag{2.63}$$

For reasons of continuity, at the interface of the dielectric medium and the metal at $z = 0$, for the tangential components of the two fields in x and y-direction follows:

$$A_d = A_m, \tag{2.64}$$

$$A_d k_{d,z} = A_m k_{m,z}. \tag{2.65}$$

As the $k_{j,z}$ components point in different directions, they need to be of opposing signs, thus the only solution for the two equations 2.64 and 2.65 is $A_d = A_m = 0$. Therefore it is not possible to excite SPP waves in case of s-polarised light.

2.2.1. Coupling Methods

Surface plasmons may be excited by irradiating a material with laser light, but can not occur on a smooth surface. To explain this, it is necessary to compare the dispersion relations of both the light and the SPP.
The dispersion relation of light is given by

$$k_{\text{light}} = \frac{\omega}{c}. \tag{2.66}$$

If light impinges on a surface with an incident angle of Θ, only the component parallel to the surface is of interest for the coupling to SPP, whose $k_{||}$ is given by

$$k_{||} = \sin(\Theta) k_{\text{light}}. \tag{2.67}$$

When comparing the dispersion relation of the SPP in equation 2.58 with the

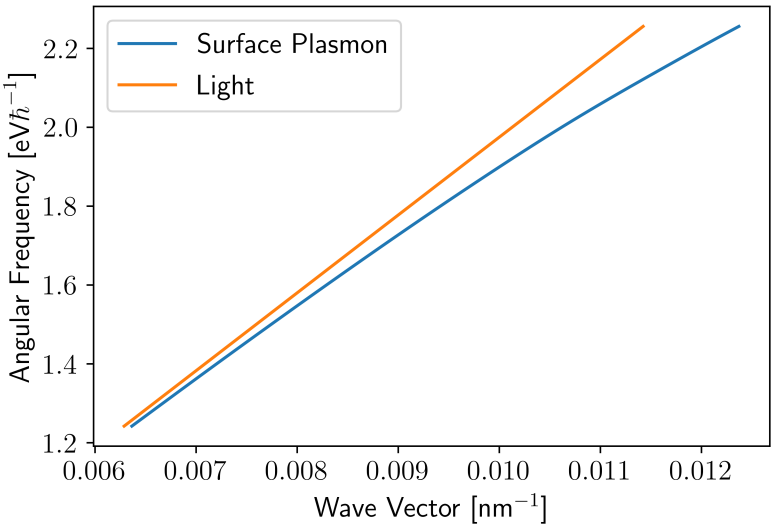

Figure 2.2.: The graph shows the dispersion relations of SPP (blue line) and light (orange line). It is visible that the SPP dispersion is lower than that of the light, which means that it is not possible that the two quantities, wave vector and angular frequency (or energy) can be conserved.

dispersion relation of light it shows that the wave vector of light and the SPP do not intersect, as can be seen in Figure 2.2. That means that the photons can not provide enough momentum needed for the SPP wave for gaining additional wave vector components and thus more momentum. The process of evoking a SPP wave with light is called coupling light to the SPP. To couple light to SPP waves, the additional amount of momentum required is given by

$$\Delta k = k_{\mathrm{SPP}} - k_{||}. \tag{2.68}$$

One way of overcoming the mismatch is via roughness of the surface in form of surface defects like edges. The defects are breaking the translation invariance of the system. As an edge has a complex shape in the Fourier space, it is capable of coupling a large range of wavelength to SPP. Klick et al. [43] looked at the influence of the height of a step edge on the amplitude of SPP waves. They found the relationship

$$\gamma = 2k_{\mathrm{las}} h \cos(\Theta), \tag{2.69}$$

here γ is the phase difference, k_{las} the wave vector of the laser beam, h the height of the step edge and Θ the angle of incidence. The maximum is expected for $\gamma = (2m)\pi$ and the minimum for $\gamma = (2m+1)\pi$, with m an integer number. Given equation 2.69, for normal incidence, the maximum is expected at a step edge height of $h_{\max} = \frac{m\lambda}{2}$ and the minimum at $h_{\min} = \frac{(2m+1)\lambda}{4}$.
Another way of coupling light to SPP waves is via a grating coupler [44, 45]. A grating can be regarded a periodic arrangement of edges, which has a narrow distribution in the Fourier space, thus only allowing for the coupling of a narrow wavelength range and for an infinitely large ideal grating only a single wavelength.
The momentum added due to the grating is given by

$$\Delta k = n\frac{2\pi}{a}, \tag{2.70}$$

where a is the period of the grating. Combing 2.68 and 2.70 leads to

$$n\frac{2\pi}{a} \stackrel{!}{=} \frac{\omega}{c}\sin(\Theta) - \frac{\omega}{c}\sqrt{\frac{\epsilon_m\epsilon_d}{\epsilon_m + \epsilon_d}}, \tag{2.71}$$

thus a matching grating period has to be chosen for a given material, wavelength and angle.

Prism Incoupling

Although not being used as a plasmon coupling method in this work, for the sake of completeness also the use of prisms for coupling shall be discussed.
As the problem concerning the coupling process comes from the mismatch in the wave vectors of the laser light and the SPP, gaining additional wave vector for the laser light is necessary. This is possible using a three layer system consisting of a metal layer between two insulators. A laser beam reflected between the metal and the prism has a wave vector given by

$$k_{\text{prism}||} = \sin(\Theta)\sqrt{\epsilon_{\text{prism}}}k_{\text{light}}. \tag{2.72}$$

There are two configurations where the coupling between the light and the SPP may take place. One is known as Kretschmann configuration [46] and the other is known as Otto configuration [47], a sketch of the two configurations in shown in Fig 2.3. The prism changes the wave vector of the SPP wave making it possible to couple

light to SPP waves. As it is shown in Figure 2.3, in the Kretchmer configuration the SPP can only form on the side of the metal film that is opposite to the prism, as the prism also alters the dispersion function of the SPP wave on the interface between the film and prism and the mismatch in wave vector stays the same as without the prism.

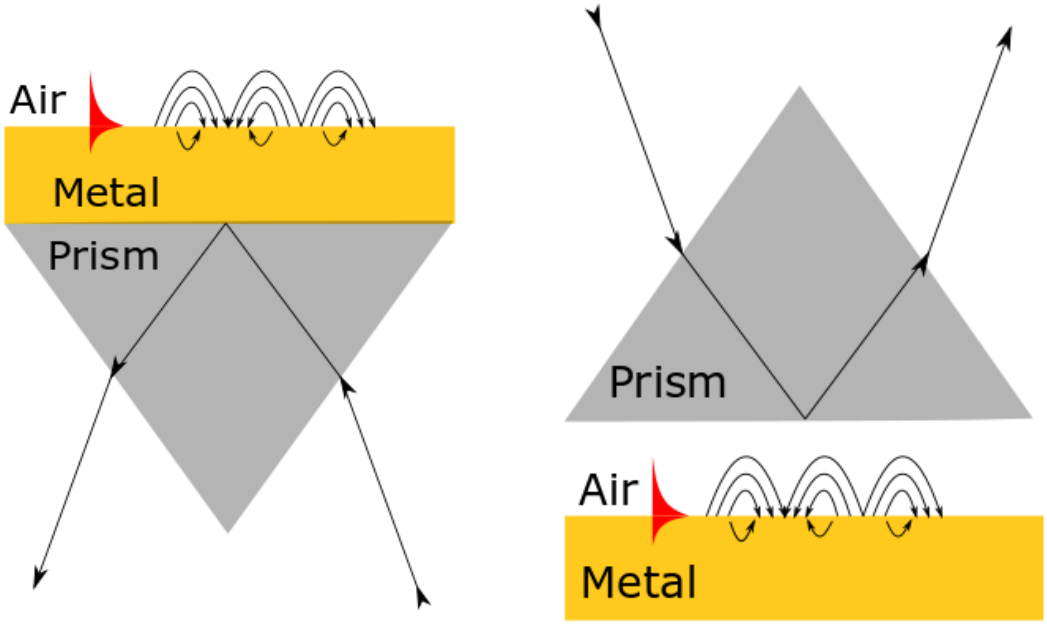

a) Kretschmann configuration

b) Otto configuration

Figure 2.3.: The two configurations that use a prism for the coupling of laser light and SPP waves. The sketch shows (a) the Kretschmann [46] configuration, where the SPP appear on the side on the surface, which is away from the prism.
Sketch (b) shows the Otto [47] configuration with a gap between the metal surface and the prism. Here the SPP do form on that side of the metal that is facing the prism.

2.3. Laser-Induced Periodic Surface Structures

Upon irradiating a surface with a laser pulse, periodic structures may appear on the surface. These structures are called laser-induced periodic surface structures (LIPSS) or sometimes ripples. The first reported observation of LIPSS was in 1965 [4] after irradiating a germanium surface with a ruby laser at a wavelength of 694 nm. LIPSS have been found on all types of material and found with various properties

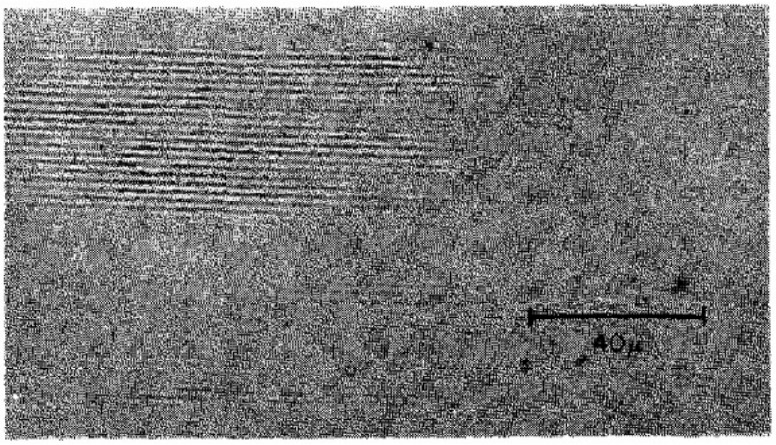

Figure 2.4.: SEM picture from Milton Birnbaum [4], showing the first documented appearance of LIPSS. The structures emerged after irradiating a germanium sample with a ruby laser.

and are often differentiated by the period of the structures. There are low spacial frequency LIPSS (LSFL), where the period Λ is

$$\Lambda_{\mathrm{LSFL}} \geq \frac{\lambda}{2} \tag{2.73}$$

and high spacial frequency LIPSS (HSFL), with

$$\Lambda_{\mathrm{HSFL}} < \frac{\lambda}{2}. \tag{2.74}$$

Despite the more than 50 years since the discovery of LIPSS, the discussion about the origin of the structures still has not settled. There are different theories concerning LSFL and HSFL.

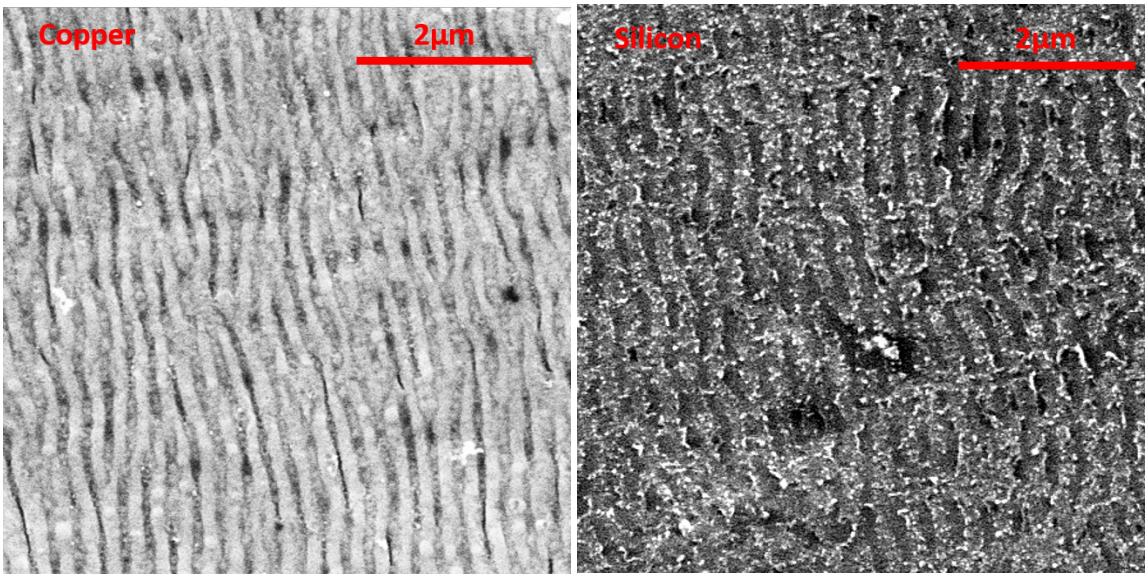

a) Copper a) Silicon

Figure 2.5.: The figure shows LIPSS forming on a) copper and b) silicon, after irradiation using 343 nm laser pulses with a pulse duration of 200 fs at a fluence of 50 mJ/cm^2 after 1000 and 50 pulses for copper and silicon, respectively.

2.3.1. LSFL

LIPSS with a period in the order of the wavelength of the light are the more frequently observed of the two types of LIPSS. LSFL have been found on various metals including gold [48–53], titanium [54], copper [55, 56], silver [56], aluminium [57], steel [54], tungsten [58] and platinum [50, 51] as well as on some semiconductors like silicon [53, 59–61], Germanium [4], gallium phosphide [62] and zinc oxide [63]. One of the main interests of analysis in LIPSS is the period of the structures. It has been found that the period is depending on the fluence of the laser beam, as well as the number of pulses. Vorobyev et al. [50] found a decrease in period with an increasing number of pulses on platinum using a 800 nm radiation and also on Tungsten [58]. Liu et al. [62] could measure a relationship between the period of LSFL on Gallium phosphide and the fluence of the laser beam, where the period increases with increasing fluence. They traced the effect back to the electronic temperature dependence of the dielectric function of the material.

2.3.2. Surface Plasmon Polariton Theory

For LSFL one of the most popular explanation of the emergence of LIPSS is the interference of laser light and SPP waves. In this theory the laser light generates SPP, if coupling is possible as discussed in 2.2.1. The SPP wave than may interfere with the still present laser light. If the amplitude of the interference is high enough, meaning the energy input onto the sample is large enough, the interference gets visible as structures on the surface. The processes involved in this structure formation are discussed in Chapter 6.
For the material to be capable of creating SPP, it need to be plasmonicly active, which means that the real part of the dielectric function must be negative, as was discussed in 2.2. For wavelengths in the range of 300-2000 nm, this requirement is fulfilled trivially for most metals and semiconductors. For dielectric materials it may be necessary to pre-heat the electronic system with a pre-pulse and thus changing the dielectric function [64, 65]. At normal incidence, the period of the resulting structures Λ_{LIPSS} is determined by the wavelength of the SPP [66–69] and can be calculated from the dispersion relation of the SPP 2.58:

$$\Lambda_{\mathrm{LIPSS}} = \lambda_{\mathrm{SPP}} = \frac{2\pi}{k_{\mathrm{SPP}}} = \frac{2\pi}{k_{\mathrm{las}}} \Re \left(\sqrt{\frac{\epsilon_m + \epsilon_d}{\epsilon_m \epsilon_d}} \right). \tag{2.75}$$

This equation may be generalised to different angles of incidence Θ and with $2\pi/k_{\mathrm{las}} = \lambda_{\mathrm{las}}$ the equation becomes

$$\Lambda_{\mathrm{LIPSS}} = \lambda_{\mathrm{las}} \Re \left(\sqrt{\frac{\epsilon_m + \epsilon_d}{\epsilon_m \epsilon_d}} \right). \tag{2.76}$$

The decay length of LIPSS L_{LIPSS} is given by the propagation length of the SPP waves L_{SPP}

$$L_{\mathrm{SPP}} = \frac{1}{2k_{\mathrm{las}}} \Im \left(\sqrt{\frac{\epsilon_m + \epsilon_d}{\epsilon_m \epsilon_d}} \right) \tag{2.77}$$

as well as the spatial profile of the laser pulse, which may differ depending on the specific profile [70]. The propagation length describes the distance over which the wave travels until its amplitude is reduced by a factor of 1/e.

The SPP theory has been tested in a number of experiments. Those were testing whether the angle dependence in the theory is consistent with experimental results [51]. Other experiments were testing the influence of the dielectric material covering the sample [62, 73].

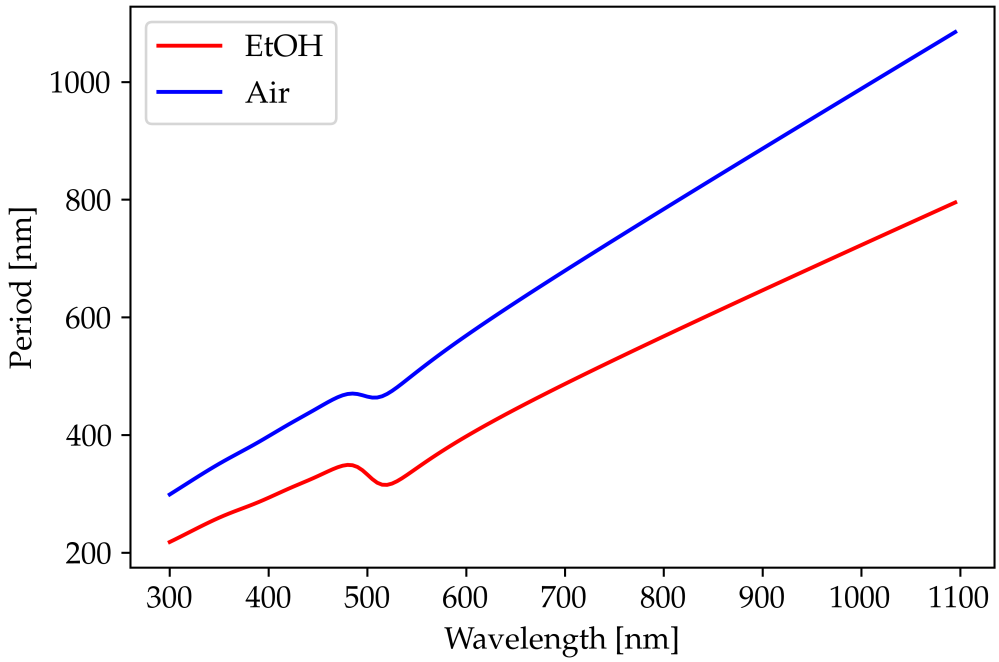

Figure 2.6.: Predicted period of the LSFL on a gold surface, depending on the wavelength of the light, if the structures are due to interference of the light and SPP. The blue curve shows the period in case of air as dielectric. The dielectric function of air is assumed to be constant, with $\epsilon(\lambda)_{Air} = 1$. The red curve shows the behaviour in case of ethanol (EtOH) as dielectric. The dielectric function for ethanol is taken from [71], that of gold is taken from [72].

Other Theories

Besides the SPP theory there are alternative theories that may explain the phenomenon of LIPSS. These theories may be classified in two categories: electromagnetic theories and matter reorganisation theories, where the SPP theory can be included as one of the electromagnetic theories.

Electromagnetic Theories Another electromagnetic theory is based on electromagnetic waves called radiation remnants, that have first been discussed by Sipe et al. [74]. This theory is used to describe the phenomenon of LSFL that are found on transparent dielectrics [65, 69, 75]. This type of LSFL are, in contrast to the LSFL given by the SPP theory, parallel to the polarisation of the laser beam and are therefore sometimes called $\text{LSFL}_{||}$ or LSFL-II. The period of these structures are

$\Lambda_{\mathrm{LSFL}||} \approx \lambda/n$, with n being the refractive index of the material.

Matter Reorganisation Theories A different approach explaining the emergence of LIPSS is based on matter reorganisation theories. In these theories the matter reshapes after laser irradiation due to mechanisms such as hydrodynamics or thermodynamic phase transitions to quasi periodic structures. The surface, which is melted by the laser pulse, is reorganised to quasi periodic structures due to local gradients [61, 69, 76].

2.3.3. HSFL

For very small structures with a period of $\Lambda_{\mathrm{LIPSS}} < \lambda_{\mathrm{las}}/2$ the origin of the appearance of HSFL is also not clear. These structures are found on metals [77–79], as well as on semiconductors [80] and dielectric materials [81, 82]. HSFL on dielectrics and semiconductors are often deeper than their period, while the structures on metals are shallower [3].

2.4. Thin Film Analysis

A confinement layer on top of a surface may be used to modify the structures created on a surface. This was observed for focused beams, [83, 84], deterministic periodic structures [85–87] and also LIPSS [62, 73]. As seen in Section 2.1.3, the thickness of the layer may greatly influence the fluence on the surface. To minimise the effect of attenuation, a thin layer is needed and with knowledge of the thickness the absorption can be estimated.
This section describes the method used for measuring the thickness of thin films as used in the experiments. The setup is presented in Section 4.3.
The measurement of the films relies on spectral measurements of white light reflected from the sample covered with a film [88]. Some part of the light is reflected at the interface between the air and the confinement layer. The transmitted light is then reflected at the interface of the layer and the material. The reflectance R is given by the refractive index and the absorption constant via

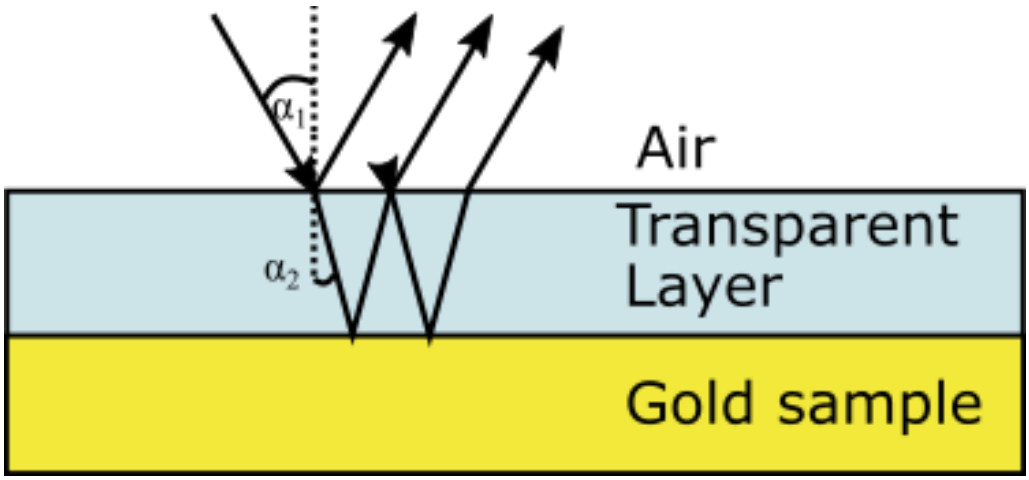

Figure 2.7.: Schematic drawing explaining the working principle of the reflectrometric thin layer analysis technique. The beam is partially reflected at the interface between air and the thin layer, as well as at the interface between the layer and gold. The two reflected beams interfere and cause an interference spectrum that is determined by the different path length of the two beams and thus the film thickness.

$$R = \frac{(n_i - n_j)^2 + \kappa^2}{(n_i + n_j)^2 + \kappa^2}. \tag{2.78}$$

In this formula the extinction coefficient of the layer is neglected. Within the thin layer, the light ray gets refracted. The angle of refraction is given by Snell's law

$$\frac{n_1}{n_2} = \frac{\sin \alpha_1}{\sin \alpha_2}. \tag{2.79}$$

The light reflected at the air-layer interface interferes with the light reflected at the layer-material interface. Depending on the length of the path travelled, the light is phase shifted, depending on the wavelength. Therefore, measuring the spectrum of white light reflected from a material with a thin layer allows for measuring the thickness of the layer.
The reflectance of the white light dependent on wavelength and layer thickness is given by

$$R = \frac{r_{01}^2 + r_{12}^2 + r_{01} r_{12} \cos\left(\frac{4\pi n_1 d \cos(\beta)}{\lambda}\right)}{1 + ((r_{01} r_{12})^2 + 2 r_{01} r_{12} \cos\left(\frac{4\pi n_1 d \cos(\beta)}{\lambda}\right))} \tag{2.80}$$

This way of measurement is called interferometric thin layer measurements. At a

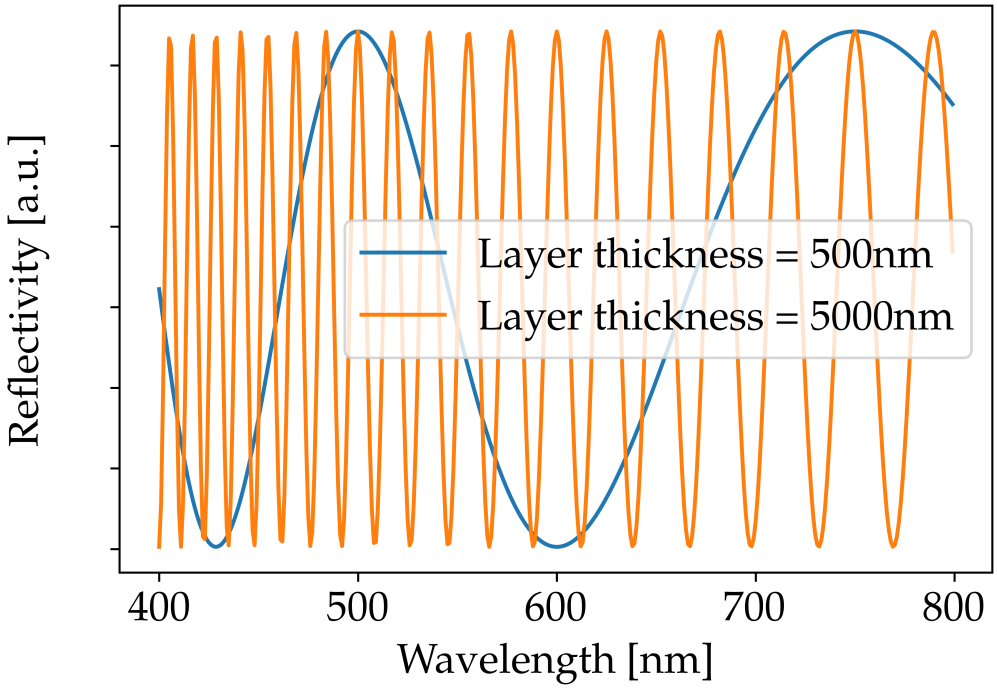

Figure 2.8.: The graph shows the calculated reflected spectra of a material with a refractive index of $n_2 = 2$ at normal incidence (0°). The blue line shows the spectrum in case of a layer thickness of 500 nm and the orange line a layer thickness of 5000 nm, the refractive index of the layer is set to $n_1 = 1.5$.

fixed angle the spectrum shows for a specific layer thickness a characteristic set of maxima and minima.
The wavelength at which the maxima emerge are given by

$$2d\sqrt{n_1^2 - \sin(\alpha)^2} = \frac{2m-1}{2}\lambda, \tag{2.81}$$

and for minima

$$2d\sqrt{n_1^2 - \sin(\alpha)^2} = m\lambda. \tag{2.82}$$

For a given spectrum it is possible to calculate the layer thickness via

$$d = \frac{1}{2\sqrt{n_1^2 - \sin(\alpha)^2}} \frac{\lambda_{\mathrm{Max},i}\lambda_{\mathrm{Min},j}}{\lambda_{\mathrm{Max},i} - \lambda_{\mathrm{Min},j}} (\frac{1}{2} + |i-j|) \tag{2.83}$$

for minima and maxima or via

$$d = \frac{1}{2\sqrt{n_1^2 - \sin(\alpha)^2}} \frac{\lambda_{\mathrm{Max},i}\lambda_{\mathrm{Max},j}}{\lambda_{\mathrm{Max},i} - \lambda_{\mathrm{Max},j}} (|i-j|) \tag{2.84}$$

for only maxima, with an analogous formula for only minima. Two examples for calculated interference patterns can be seen in Figure 2.8.

2.5. Laser-Matter Interactions

When irradiating a metal with a laser beam, the results are highly dependent on the pulse duration of the laser [89, 90]. This is mainly due to the high heat conduction of metals in which heat diffusion transfers the deposited energy to areas outside of the irradiated region. This is mainly the case if the pulse duration is larger than the electron-phonon coupling time, which is the time needed for the electrons in the system to transfer their energy to the lattice. The theory describing the heat transfer between electrons and atoms in a metal is the two-temperature model, which will be presented in more detail in Section 3.2.1. For metals, the electron-phonon coupling time lies in the order of a few picoseconds up to a few tens of picoseconds [91, 92]. Chichkov et al. [93] investigated the shape of holes produced by laser ablation in a steel foil applying different pulse durations. The results can be seen in Figure 2.9. Their results show cleaner ablation results when using a beam with a short pulse duration, also the heat affected zone gets smaller as the pulse duration decrease. The group of Hashida et al. [90] investigated the change of ablation threshold in

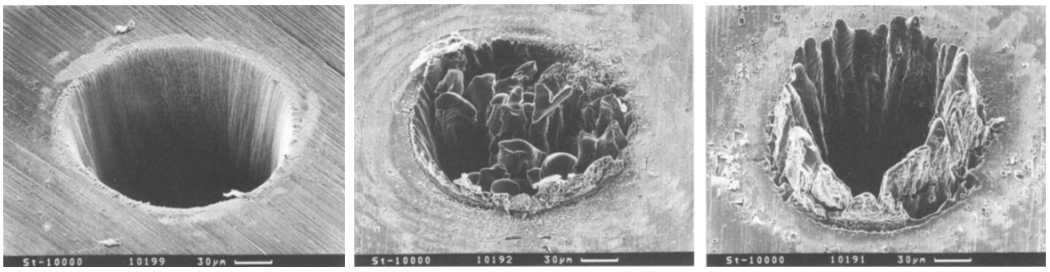

a) 0.2 ps, 0.5J/cm^2 b) 80 ps, 3.7J/cm^2 c) 3300 ps, 4.2J/cm^2

Figure 2.9.: Scanning electron microscope pictures showing the results of ablation experiments using pulses with a) 0.2 ps b) 80 ps and c) 3300 ps pulse duration with a laser wavelength of 780 nm. In all three experiments 10000 pulses are used, with increasing fluences for increasing with the pulse duration. The pictures are taken from [93].

copper at different pulse durations and found a reduction in the ablation threshold for shorter pulses. For short pulses, if the energy deposited to the sample is sufficient to create an overheated melt, the ablation occurs in an explosive removal of material, leaving a clean structure as can be seen in 2.9 a). For longer pulses the still persistent beam hits the already melted surface, it may push the melt to the side, causing the appearance of the structures as indicated in Fig. 2.9 b) and clearly visible in Fig. 2.9 c).

2.5.1. Periodic Laser Structuring

One way to study the fundamental processes of ablation is by simulating such process and compare the results with experimental observations. A limiting factor of the simulations is the size of the simulation volume; a more detailed description of this topic can be found in Section 3.2. A possible way to overcome this limitation is to simulate a periodic structuring event, where a small spatial section is representative for the complete process. This technique is applied in the publications [85, 94].
Here the theoretical description of the process of two beam interference shall be described.
There are two common methods to produce the two beams for the interference: either via a conventional beam splitter or by a grating. A beam travelling in z-direction, with a component in x-direction can be written as

$$E(t, x, z) = E_0 \exp(i(k_x x + k_z z - \omega t)). \tag{2.85}$$

Assuming the two beams are having the same amplitude and are enclosing the same angle to the normal axis, which is described by $k_{-x} = -k_x$, the interference is given by

$$E_{\text{inter}} = E_0 \left(\exp(ik_x x) + \exp(-ik_x x)\right) \exp(i(k_z z - \omega t)). \tag{2.86}$$

The intensity in x-direction is than given by

$$I = 2\epsilon_0 c E_0^2 \cos(k_x x)^2 = \epsilon_0 c E_0^2 (1 + \cos(2k_x x)), \tag{2.87}$$

which shows a periodic distribution.
Ivanov et al. [95] and Blumenstein et al. [96] have investigated the formation of periodic structures in detail by comparing experimental findings with simulation results. They found, that for low fluences the structures form because the surface gets uplifted by voids forming under the surface, with these sometimes opening to the surface. This is termed surface swelling and is sometimes accompanied by local openings of the voids to the surface. For higher fluences, the voids open along the complete structure and with large velocities, causing the walls of adjoining structures to combine forming nanoridges [96]. This type of structures formation is called surface wall formation.Increasing the fluence further, causes the surface to melt on a large scale, destroying the periodic structures [96]. This is called broad melting. The appearance of the different types of structures can be seen in Figure 2.10.

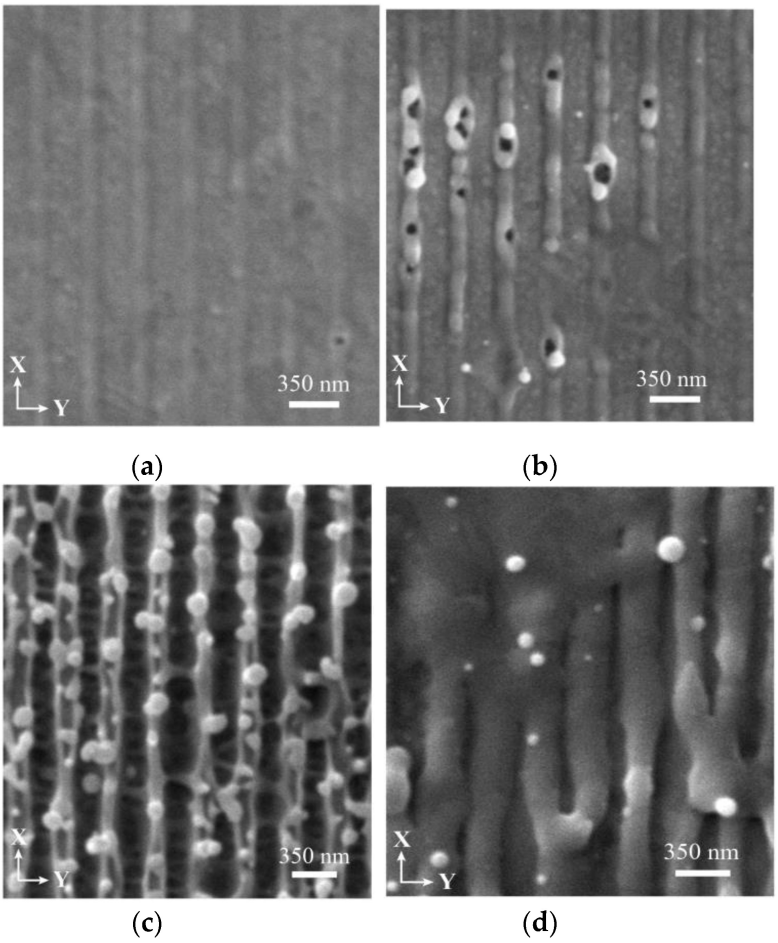

Figure 2.10.: The figure shows the different types of structures forming on gold after single pulse irradiation at a wavelength of 248 nm and a pulse duration of 1.6 ps for different fluences. At 100 mJ/cm^2 (a) surface swelling, at 150 mJ/cm^2 (b) void openings at 200 mJ/cm^2 (c) wall formation and for at 350 mJ/cm^2 broad melting is obtained. The figure is taken form [96].

2.6. Structures under Confinement

Ablation of a material with ultrashort laser pulses has intensely been studied with an increasing focus on changes in the resulting structures due to a transparent layer on the surface.

Trtica et al. investigated the difference in ablation of Ti irradiated with femtoscond pulses in air and under a water layer [86] (Figure 2.11). They found, that the structures were deeper in case of water confinement. Additionally, they observed a change in the chemical composition of the surface, depending on whether the confinement

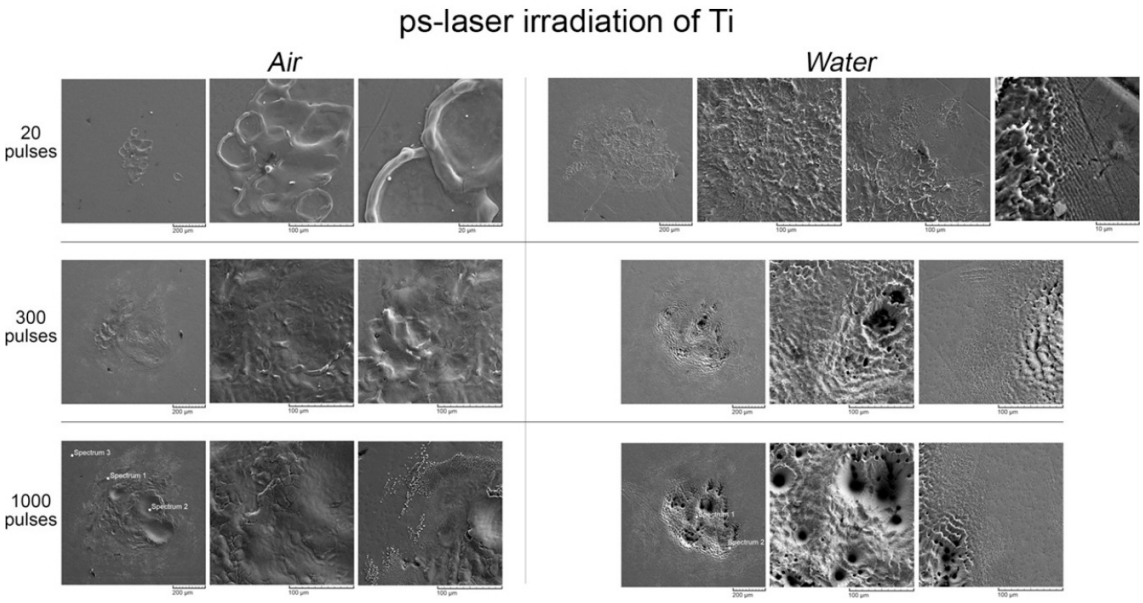

Figure 2.11.: The SEM pictures show the different appearance of ablation events on titanium in (left) air and (right) water after a varying amount of laser pulses using a 1064 nm picosecond laser source. The fluence in air was 10 J/cm^2 and in water 7.6 J/cm^2. The appearing craters are deeper in a water environment and LIPSS appear after fewer pulses. The pictures are taken from [86].

layer was present or not. Also they found LIPSS appearing in both cases, although in the case of a water layer, the structures appeared after fewer pulses and also nanoparticles may appear when a confinement layer is present.
Kaakkunen et al. [97] found that holes in silicon produced with 1000 pulses are deeper, when the surface is sprayed with water to produce a water film using a 130 fs laser at 780 nm. Smirnov et al. [98] found for 515 nm at different pulse durations, that the depth of a crater produced by a single pulse in water was smaller for the shortest pulse duration of 300 fs compared to the longest pulse duration of 10 ps. A trend that was reversed in the case of irradiations in air.

Spellauge et al. [99] found in pump-probe experiments using a pump beam with 3 ps pulse duration and a wavelength of 1056 nm, a shock wave and cavitation bubble forming, looking similar to results from laser-induced breakdowns in water [100], where similar behaviour is observed by irradiating a liquid.
Laser ablation in liquids is also considered a possible way of producing nanoparticles of noble metals [101–103]. Shih et al. [87] took a closer look at the generation of nanoparticles and also LIPSS on chromium by comparing experimental and computational results. They found a similar behaviour of the sample surface upon laser irradiation, as in both cases the top layer starts to heat up rapidly and is evaporated in a mixture of vapor and liquid droplets of chromium. In the case of air or vacuum environment, the ablation plume may expand freely, but with a confinement layer the evaporated material is rapidly decelerated. The water is heated by the ablation plume and thus expanding, pushing back the ablated surface material.
Shih et al. also found that the thin wall like structures appearing in an irradiation event in air evolves to a smooth, less prominent bump when the irradiation is done in water environment. In 2017 Ivanov et al. [85] investigated the creation

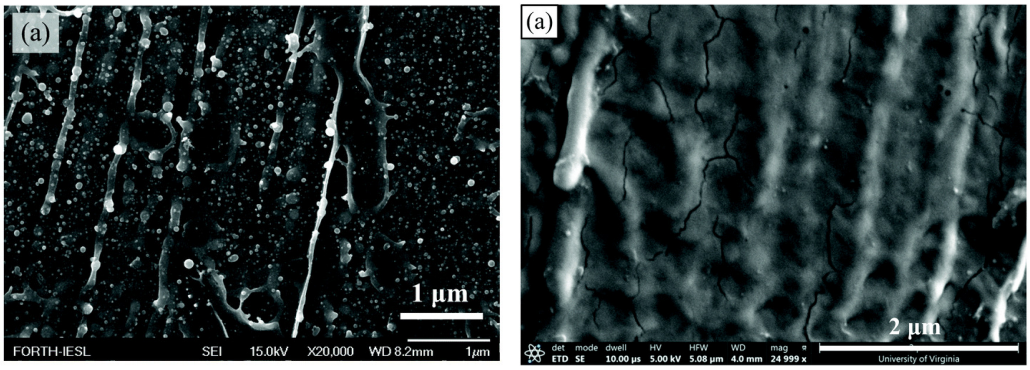

a) Air b) Water

Figure 2.12.: The SEM pictures show the structures forming on chromium (a) in air and (b) in water. The used laser has a wavelength of 1026 nm and a pulse duration of 200 fs. The incident fluence was 6 J/cm^2. Also the small, round debris particles present under irradiation in air vanished in the case of a water confinement. The pictures are taken from [87]

of periodic structures on gold, produced via two beam interference in air and water environment. They compared the structures produced in experiments with the results of simulations using a molecular dynamics - two temperature model (MD-TTM) framework described in [95]. In the simulations, they observe an uprise of the surface material due to the creation and expansion of voids underneath the surface.

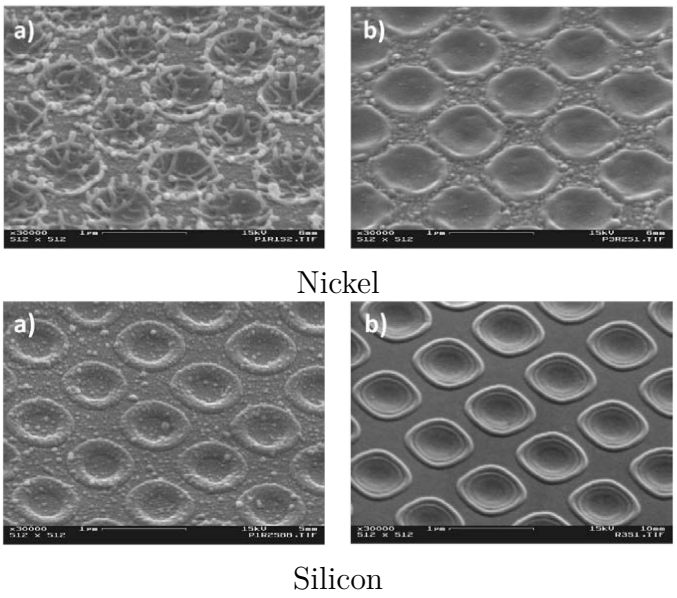

Figure 2.13.: The upper part of the figure shows structures appearing on Nickel after irradiation with 1.1 J/cm^2, the left pictures without a PMMA confinement layer and the right with a PMMA layer of 400 nm thickness. The comparison of the pictures show that the borders of the structures become much smoother when the layer is included.
The lower pictures show structures on Silicon after irradiation with 300 mJ/cm^2, left without the PMMA layer and on the right side with layer. The wavelength in all cases was 248 nm and the pulse duration 500 fs.The Figures are taken from [1].

This starts at about 300 ps after irradiation. As the shock wave caused by extension of the gold surface hits the gold-water interface, the water layer starts separating from the gold surface. A comparison of the results in air and water after 1000 ps shows an opening of the structures in case of air, while for water the structures stay closed and form a bump. Both Shih and Ivanov agree, that a confinement layer suppresses the formation of sharp features and result in more smooth and shallow forms.
There are also studies of the effects of a solid confinement on the appearance of structures. Klein-Wiele and Simon [1] used a Poly(methyl methacrylate) (PMMA) layer on Silicon and Nickel sample. The PMMA layer was 400 nm and applied via spin coater. They found that with the layer, very thin structures in the order of 10 nm formed and the deposition of debris is reduced. The results found in the study can be seen in Figure 2.13.

3. Methods and Concepts

3.1. Laser Light Sources

For the experiments two different laser systems were used. In this section the two laser sources will briefly be described and their important parameters listed. The two laser systems are a "Pharos" from Light Conversion and a "Hyper Rapid" from Coherent (formerly Lumera). The two systems differ mainly in the pulse duration, while their wavelengths are very similar.

3.1.1. Pharos

The Pharos laser system is a fiber laser using an active material of ytterbium doped potassium gadolinium tungstate (Yt-KGW). The fundamental wavelength of this material is 1030 nm and additional modules are used to convert the laser wavelength to the second and third harmonic to 515 and 343 nm, respectively. The pulse duration has been measured using a self-diffraction frequency resolved gating [104] (SD-FROG) setup. The results of the SD-FROG measurements are summarised in Table 3.1. The output beam is Gaussian shaped with a beam size of about 4 mm. The Laser has a power of 20 W at a maximum repetition rate of 300 kHz. The beam energy can be controlled by a pulse picker.

Wavelength [nm]	1030	515	343
Pulse duration [fs]	≈280	≈180	≈200

Table 3.1.: Measured pulse duration of the Pharos laser system at the different wavelengths, measured using a self diffraction frequency resolved optical gating system. The measurement was done with the beam line including all the transmissive optics as implemented in the experiments.

3.1.2. Hyper Rapid

The Hyper Rapid is a laser system using neodymium doped yttrium vanadate (Nd-YVO_4) as active material. The fundamental wavelength of this material is 1064 nm. Just like for the Pharos, there are modules for generating the second and third harmonic with wavelengths of 532 and 355 nm. The pulse duration at the fundamental is specified as 8 ps. The pulse duration is longer than the possible range of the SD-FROG, therefore a measurement of the pulse duration of the different wavelengths was not possible, but it can be assumed that the pulse duration at all wavelengths is close to 8 ps. The maximum power of the laser source is 50 W with a maximum repetition rate of 400 kHz. The beam energy is variable by an internal attenuator. The beam size is about 2.5 mm.

3.2. Molecular-Dynamics - Two-Temperature-Model

The simulations later presented in this work are based on the molecular dynamics-two temperature model (MD-TTM), therefore a short introduction in the concepts of this type of simulation will be presented here.
The MD-TTM model combines two approaches, one is the molecular dynamics (MD) approach and the other is the two temperature model (TTM).

3.2.1. Two-Temperature-Model

In the TTM, the material is described by two distinct systems, the electronic system and the lattice. After irradiating a target material with a short laser, pulse the beam energy is mainly deposited into the electronic system, and from there energy transfer to the lattice takes place. Its characteristic duration, the electron-phonon coupling time is material dependent and is in the range of $0.1 - 10$ ps [69].
The main part of the TTM is a pair of coupled differential equations connecting the temperatures of the electronic system and the lattice [105]:

$$c_e \frac{\partial T_e}{\partial t} = \nabla(\kappa_e \nabla T_e) - \alpha(T_e - T_i) + Q \tag{3.1}$$

$$c_i \frac{\partial T_i}{\partial t} = \nabla(\kappa_i \nabla T_i) - \alpha(T_e - T_i), \tag{3.2}$$

here the indices e and i are related to the electronic system and lattice (ionic) respectively, with c being the specific heat, T the temperature and κ the thermal conductivity. The source term Q describes the energy input per volume and time into the system. As for short laser pulses the complete input energy is absorbed by the electronic system, the source term is only present in 3.1 describing the temporal evolution of the electronic system. The source function contains the interactions between the laser and the sample, like absorption, two-photon absorption but also excitation of SPP and the interference with light.
Some limitations of the TTM are, that the model does not attribute temperatures to single electrons but rather has a temperature field component containing multiple electrons which may not be in thermal equilibrium. As the TTM assumes that the time and length scales of the temperature variations are much larger than the relaxation time and mean free path of the electrons, it describes the energy transport by a classical Fourier law [105].

3.2.2. Molecular-Dynamics

Simulations using MD are used to model the response of the material to laser irradiation on a molecular level. In MD simulations the Newtonian equations of motion are solved for all particles like atoms or molecules [106]. There the choice of the potential which represents the forces acting on the particles is of great importance as it largely determines the motions of the particles. For rapid processes like melting, the potential additionally needs to be time dependent [69].
MD simulations allow to precisely track the motions of the individual particles and also are capable of showing phase transitions. One way to make phase transitions visible is via the central symmetry parameter (CSP) [107]. The CSP calculates the distribution of the neighbouring particles and evaluates the symmetry around that particle. In a fully symmetric crystal lattice the CPS is zero and increases with reducing symmetry which allows for defining a liquid and gaseous phase. One has to consider that due to the broken symmetry, the surface has an artificially increased CSP.
In the combined MD-TTM approach, the equation for the temperature development of the lattice 3.2 is replaced by the individual motion of the particles [108].
Calculating the equations of motion for individual particles comes at the expense of a need in large computational power for a meaningful volume. Thus it is only possible to simulate regions of a few hundreds of nanometres for time scales interesting for ablation precesses at a reasonable computational time.

3.3. Sample Evaluation

In order to evaluate the results of the experiments, the samples have to be evaluated post-mortem. Due to the small size of the features of interest, a light microscope is not sufficient, therefore devices with a higher resolution are used. These are the scanning electron microscope (SEM), which allows for recording pictures with a few nanometres resolution and an atomic force microscope (AFM), which additionally allows for height measurements on the samples.

3.3.1. Scanning Electron Microscope

As stated by Abbe's law, the possible spatial resolution d with electromagnetic waves is limited by

$$d = \frac{\lambda_{light}}{2NA}, \tag{3.3}$$

with NA being the numerical aperture of the used objective. The SEM technology takes advantage of the material wave of electrons, which, depending on the velocity of electrons, are much smaller than the wavelength of visible light.
In the SEM, the electrons are produced in a tungsten filament using a current of a few amperes to create an electron cloud. The electrons are accelerated towards a ring anode, with an acceleration voltage of 1-50 kV. The electron beam is focused by magnetic lenses, which are also used to deflect the beam. The beam is focused on the sample, where the electrons are either scattered from the atoms of the sample (backscattered electrons (BSE)) or they may react with the atoms of the sample to emit electrons itself (secondary electrons (SE)).
The sample is scanned line by line and either the SE or BSE are recorded in a detector. The SE are mainly produced at the surface of the sample up to a depth of a few nanometres. Therefore, the SE detection is sensitive to the topography of the surface, as more electrons can be detected e.g. from higher standing convex features with small radii than from concave craters or holes.
The BSE are registered by detectors sitting close to the exit of the initial electron beam. These detectors change the contrast depending on the difference of atomic values of the material, which allows to differentiate between different materials.
Due to the electron beam there has to be vacuum in SEM, so it is not possible to investigate living samples. Also, due to the bombardment of electrons, the charge needs to be removed from the sample, to avoid repulsion of the electron beam from

the sample. The advantages of the SEM are a high resolution in the range of nanometres as well as fast rendering of pictures in seconds to minutes.
The used device for this work was a Zeiss EVO MA10.

3.3.2. Atomic Force Microscope

Another method used for measuring small structural details is atomic force microscopy. The measuring technique relies on scanning the sample using a small bendable tip, called cantilever. The AFM can be used in either contact and non-contact mode and as for evaluating the experimental results only the non-contact mode was used, it will be explained in more detail.
In the non-contact mode the cantilever does not touch the surface but is hovered above the surface, while oscillating in z-direction in its resonance frequency. The cantilever is then moved in x and y-direction over the sample, which is accomplished at rather slow velocities, thus AFM measurements take much longer than a SEM measurement. The oscillating cantilever oscillating and brought close to the surface, where different attractive and repulsive forces act on the tip depending on the distance to the surface. The forces change the phase or the amplitude of the oscillation of the cantilever. From this the forces acting on the tip can be determined and thus the distance to the surface can be evaluated. As the cantilever is scanned in x- and y-direction, the result is a map of the surface heights at different positions.
The measurement can be disturbed by vibrations, air movement, air circulation and acoustic distortions. To reduce these effects the apparatus is put on a vibration isolated table and in a closed housing to prevent air flow effects. Other sources of noise come from internal electronics and thermal fluctuations, thus for the best possible resolution of up to atomic resolution, the device needs to be cooled. As atomic resolution was not needed, the device is not cooled. The AFM used in this work, was a Park Systems XE-150.

4. Experimental Setups

For producing the data discussed in the Chapters 5 and 6, different experimental setups are used, which will be presented in this chapter. The first setup produces periodic structures using the two-beam interference technique, with UV light of both the Pharos and the Hyper Rapid, introduced in Section 3.1.1 and 3.1.2. The second setup was used for the generation of LIPSS, by irradiating a sample with a homogeneous laser beam, here the Pharos was used at all available wavelengths in IR (1030 nm), green (515 nm) and UV (343 nm). The third setup presented in this chapter is the configuration used to measure the thickness of the liquid layers which was implemented in the two-beam interference setup.

4.1. Two-Beam Interference Setup

This setup is used to produce deterministic periodic structures via two beam interference using the UV beams of both laser sources. The beams were spilt by a transmission grating and the diffracted beams were then brought together by a microscope objective. A sketch of the setup is shown in Figure 4.1.

To evaluate the fluence dependence of the forming structures, a rather homogeneous beam profile is helpful, but as the original beam shape is Gaussian, a method of modifying the beam profile was necessary. To change the Gaussian to a homogeneous Top-hat distribution, a commercial beam shaper was used (TOPAG Lasertechnik GmbH, FSB2-40-343). A more detailed description of its operating principle can be found in [109]. The component does not change the polarisation of the beam and is optimised for a Gaussian shaped input beam with a diameter of 4 mm.

After the beam shaper, the beam is focused by a lens. The diameter of the Top-hat profile b is dependent on the wavelength of the laser λ_{las}, the beam diameter d at $1/e^2$ level and the focal length f of lens, and is given by

$$b = \frac{2\lambda_{\text{las}} f}{d}. \tag{4.1}$$

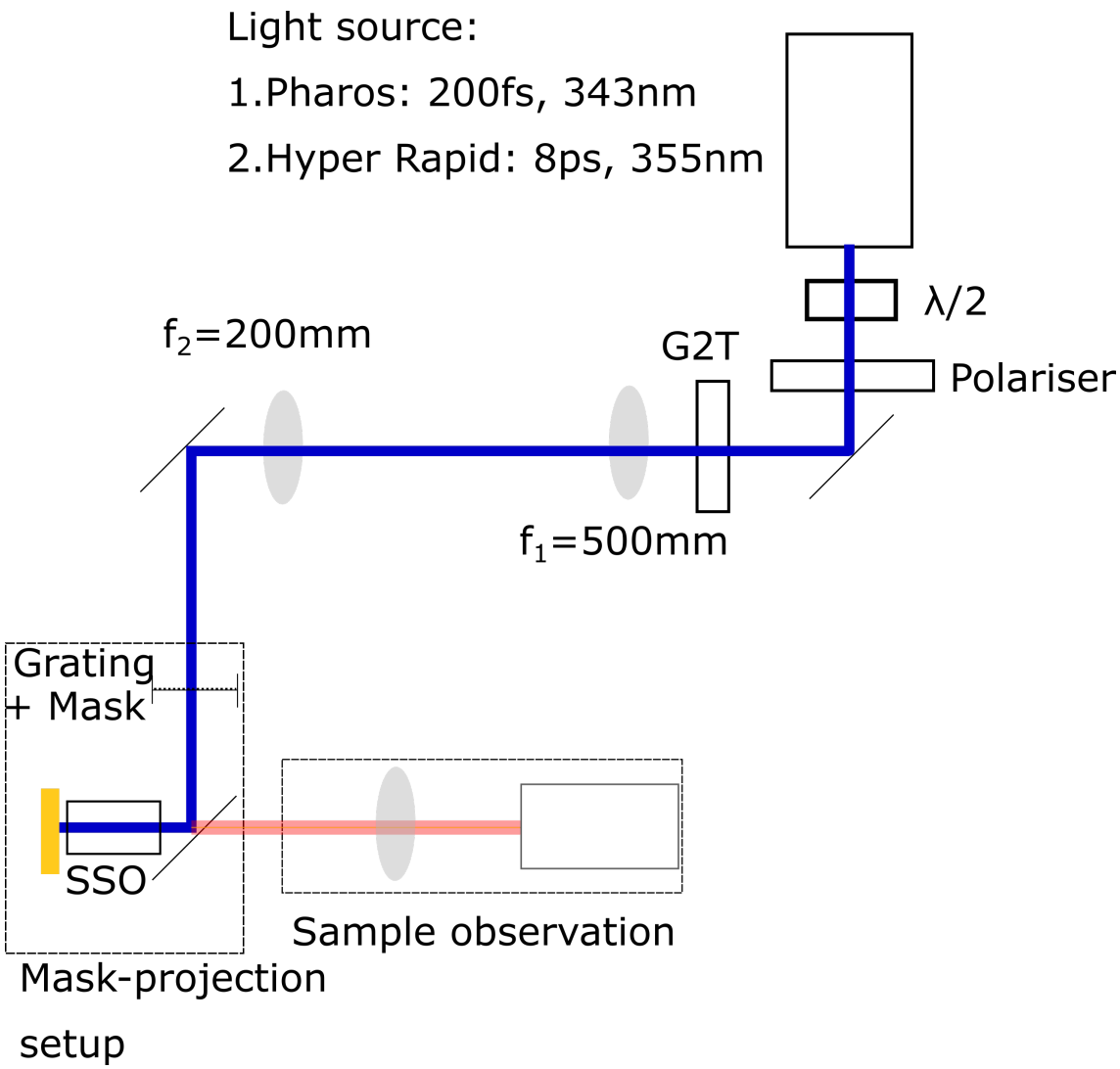

Figure 4.1.: The figure shows a sketch of the setup used for the experiments to produce periodic structures on gold samples by using the two-beam interference method. In the setup the beams travel trough a $\lambda/2$ waveplate and a polariser to control the polarisation of the beam. Afterwards, the beam passes the Gauss-to-Top-hat (G2T) beam shaper, that manipulates the phase of the beam in such a way, that a homogeneous beam profile is produced in the focus of the f_1 =500 mm lens. This profile is than imaged using the f_2 = 200 mm lens to the position of the grating. The setup for the mask projection as well as the sample observation are described in more detail in the Figures 4.3 and 4.4.

A lens with a focal length of 500 mm was used, the wavelength of the laser was 343 nm and the beam diameter was 4 mm, so the resulting Top-hat profile has a diameter of about 85 µm.
This profile was then imaged to the position of the grating using another lens with focal length f_2 200 mm. The size of the Top-hat profile at the position of the grating was than about 800 µm.
For the two-beam interference, the beam was split by using a transmission grating. At the grating the beam is diffracted in multiple diffraction orders; the angle Θ_n of the n^{th} order under normal incidence depends on the wavelength of the laser light and the period of the grating g:

$$\Theta = \arcsin\left(\frac{n\lambda_{\text{las}}}{g}\right) \tag{4.2}$$

The intensity of the n^{th} orders after the grating for an amplitude grating, which spatially modulates the amplitude of the beam is given by

$$I_n \propto \left|\frac{g}{2}\text{sinc}\left(\frac{n\pi}{2}\right)\right|^2, \qquad \text{with } \text{sinc}(x) = \frac{\sin(x)}{x} \tag{4.3}$$

for a grating with a slit width of $g/2$. The efficiency η_n of the different orders is given by

$$\eta_n = \frac{I_n}{\sum_{n_{\text{min}}}^{n_{\text{max}}} I_n}. \tag{4.4}$$

For the two first orders (± 1), the efficiency is ≈ 20 %, but as only half of the beam passes the amplitude grating, only ≈ 10 % of the total energy is contained in the first orders after the grating. Due to the low energy output of the amplitude mask, a phase mask was used, produced by Dr. Jörg Meinertz from Insitut für Nanophotonik via backside ablation of a SiO_x film on a quartz substrate with subsequent annealing. A phase grating has two advantages compared to an amplitude grating. First, the complete beam is transmitted through the grating, hence resulting in a higher transmission. Second, if using the correct depth of the grooves, the zero order can be suppressed, thus directing more energy in the first orders. The phase grating used in the experiments is a transmission quartz optic with periodically alternating plateaus and grooves. A sketch of a phase grating can be seen in Figure 4.2. For an optimal energy transfer the height of the steps should be $\lambda_{\text{las}}/2$, therefore the phase gratings only work optimally for a small wavelength region. The used phase

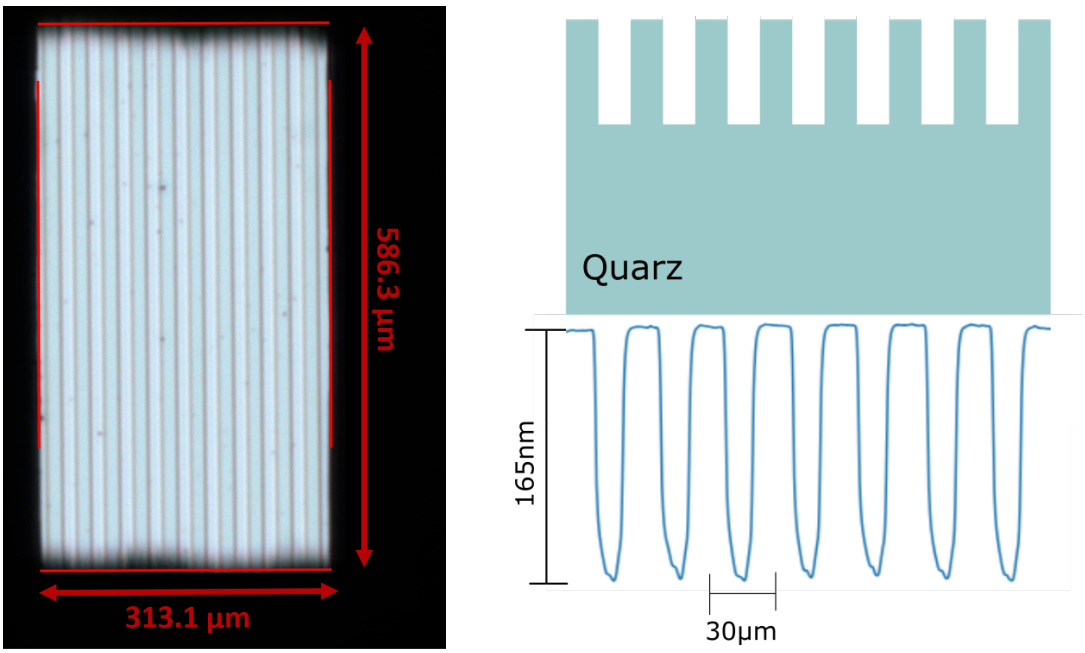

a) Grating with mask

b) Grating

Figure 4.2.: The picture shows (a) the phase grating together with the mask used to create sharp borders in the irradiations. The grating has a period of about 30 µm and the size of the mask is about 300 µm x 600 µm. (b) shows a sketch of the phase grating, together with a height measurement of the grooves. The height profile was taken using the stylus profilometer DekTakXT by Bruker. The height of the grating was measured to be about 165 nm.

mask has a step height of about 170 nm, a period of 30 µm and a step width of about 15 µm. A picture of the grating can be seen in Figure 4.2. Due to the special design of the phase grating it is not necessary to block the 0^{th} order, which in case of an amplitude grating would carry most of the energy and may damage optical components behind the grating.

Directly in front of the grating a mask is placed. The size of the mask is about 300 µm x 600 µm, a pictures of the grating with the mask can also be seen in Figure 4.2. Behind the grating with mask, the beams are reflected by a mirror to allow for a sample observation as described in 4.1.1. The two first orders are then used to form a demagnified image of the mask onto the sample by using a Schwarzschild-objective (SSO). The used SSO was a LMM-40X-UVV-160 from Thorlabs Inc., with a nominal magnification M_{mag} of 40 and a numerical aperture NA of 0.5. As only the two first orders are used in the imaging process, the period of the final structures

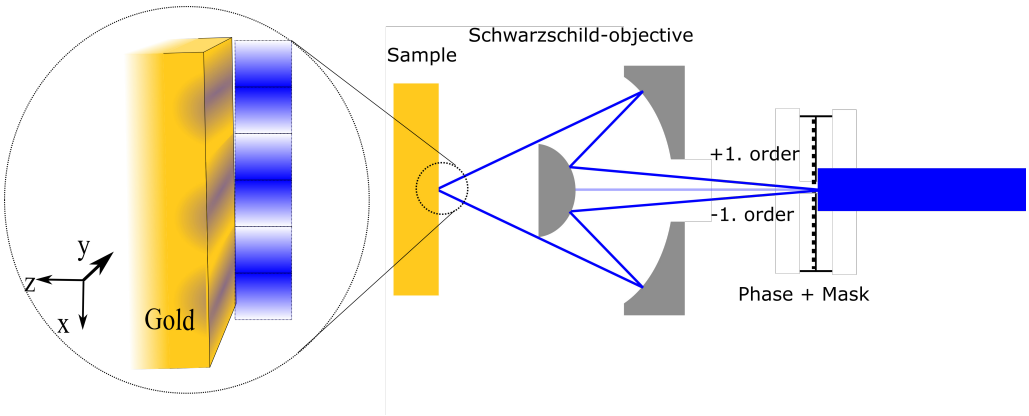

Figure 4.3.: This figure shows a detailed sketch of the setup used for the two-beam interference. The incoming beam is split by the phase grating shown in Figure 4.2. Due to phase mask the main energy is in the $\pm 1^{\text{st}}$ orders, which are than directed to the Schwarzschild-objective (SSO). The objective directs both beams onto the sample, where they form an interference pattern. In the actual setup, there is an additional mirror between the grating and the SSO that is necessary due to the additional sample observation described in Figure 4.4, but left out for the sake of clarity.

are half of what would be expected by the magnification alone. The period of the structures are calculated via

$$d_p = \frac{1}{2}\frac{g}{M_{\text{mag}}}. \tag{4.5}$$

For a grating with $g = 30$ µm and the given magnification, the expected period is 375 nm. Theoretically, the objective supports structures with a period of 375 nm, but due to the finite size of the beam, not the complete numerical aperture could be used, therefore the magnification of the objective was reduced by moving the grating closer to the objective. The structures finally have a period of about 500 nm, which translates to a magnification of about 33.3.

4.1.1. Sample Observation

A sharp image of the mask is produced only in the plane where the two orders completely overlap. The depth range in which this is fulfilled is only a few micrometres, therefore a precise sample observation is needed to reproducibly find the correct position. It is also useful to see the sample surface during the experiments, especially for irradiation of the step edge in the LIPSS setup described in Section 4.2.
A sketch of the sample observation can be seen in Figure 4.4. The sample obser-

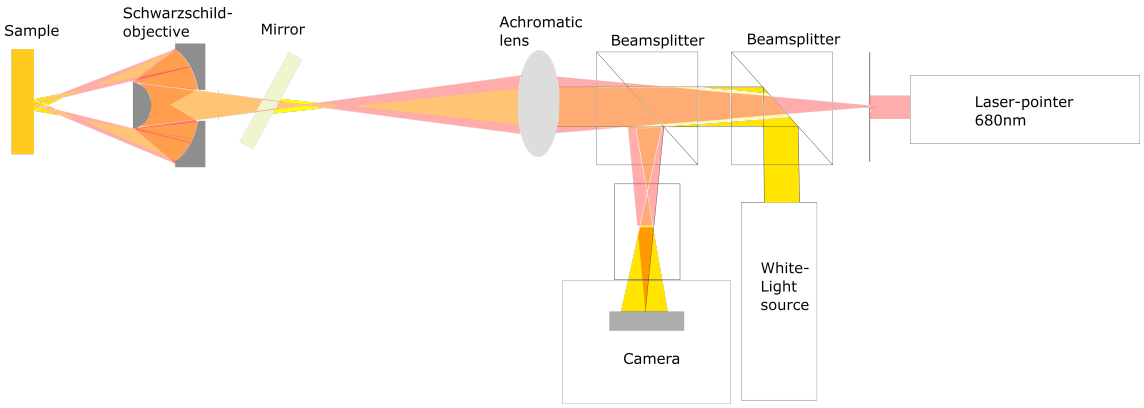

Figure 4.4.: The figure shows a sketch of the sample observation in the two-beam interference experiments.

vation does serve two purposes, one is to ensure that the sample is in the correct working plane, where the two beams form the interference pattern. The other is to make the sample surface visible to prevent multiple irradiation of the same position. For the positioning purpose, a laser-pointer is used to illuminate a pinhole of 20 µm diameter. The pinhole is then imaged by an achromatic lens to the plane that corresponds to the position of the phase grating shown in Figure 4.3. From there the image of the pinhole is again imaged by the SSO. The beam of the laser-pointer is then reflected back by the sample and travels through a beam splitter to a camera, whose chip is positioned in a plane corresponding to that of the pinhole. If the correct position of the sample is adjusted, the camera shows the image of the pinhole as a dot with the smallest diameter upon varying the sample position.
The visibility of the sample surface is ensured by a white light source, which is coupled into the beam path by another beam splitter. The light source illuminates the sample surface, which is imaged to the camera chip.

4.2. LIPSS Setup

The LIPSS experiments were done using the fundamental as well as the second and third harmonic beams of the Pharos. There were two beam lines, one for the UV beam and another for both green and IR, as the mirrors have a high reflectivity for both wavelengths.

4.2.1. UV Beam Line

The beam path includes a $\lambda/2$ waveplate and a polariser for polarisation control. Analogous the two-beam interference setup, the beam is reshaped by the Gauss to Top-hat beam shaper from TOPAG. Instead of being further imaged as in the other setup, the original Top-hat was used. Placing a lens with a focal length of 250 mm behind the beam shaper, resulted in a Top-hat size of $\approx$ 40 µm. A sketch of the setup is shown in Figure 4.5 (blue beam line) and a picture of the beam profile in Figure 4.6.

4.2.2. Green/IR Beam Line

The beam lines for the green and the IR beams also use $\lambda/2$ waveplates and polarisers. As noted earlier, the used dielectric mirrors are usable for both green and IR wavelengths, so only one beam line is used and those components which are wavelength dependent like the $\lambda/2$ waveplate can be switch via interchangeable mounts. A sketch of the beam line is given in Figure 4.5 (green-red line).

As in the previous case, the beam profile should be homogeneous at the sample position, but the beam shaper was not optimised for 515 and 1030 nm and performed poorly in producing a homogeneous beam profile there. Instead, another mask projection setup was used, in which the central region of the Gaussian beam was cut out and imaged onto the sample surface. This technique has the disadvantage that one has to find a balance between beam homogeneity and transmitted energy. The size of the mask was 1.2 mm and was demagnified to about 40 µm using a achromatic lens with a focal length of 50 mm. In front of the mask a field lens with a large focal length of 3.3 m was placed and moved to vary the energy of the beams going through the mask.

The beam profiles of the green and IR beam are shown in Figure 4.6.

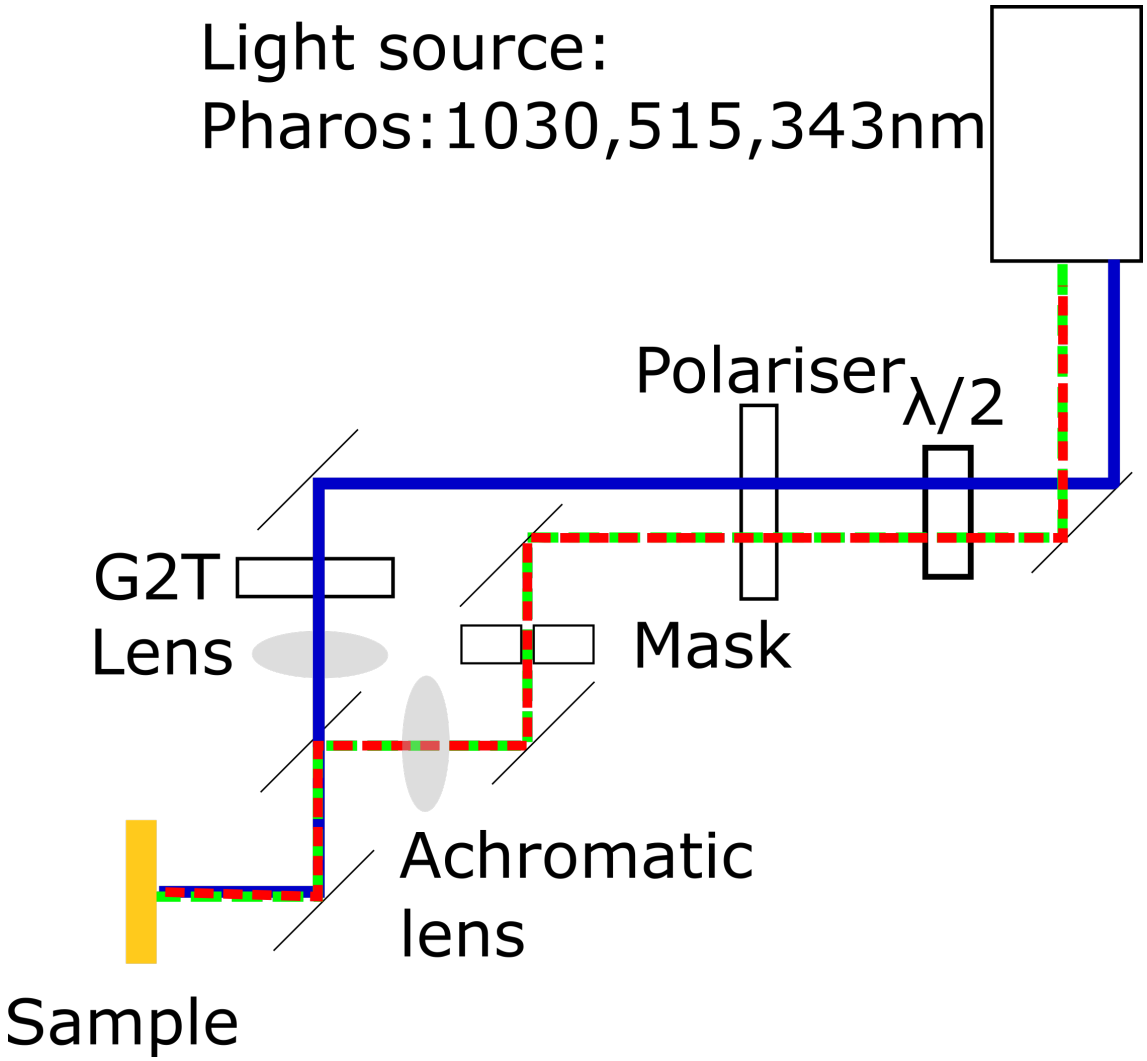

Figure 4.5.: The figure shows the beam paths used for the investigation of LIPSS: one for UV and the other for green and IR light. The two paths are necessary for two reasons. First, the used mirrors are of two types, one is highly reflective only in the UV region, whereas the other is highly reflective in green as well as in IR. Second, the used Gauss-to-Top-hat (G2T) beam shaper is optimised only for UV and produces poor results for the other wavelengths. Therefore, for green and IR, a homogeneous beam profile is achieved by cutting out the central region of the Gaussian profile via imaging of a mask.

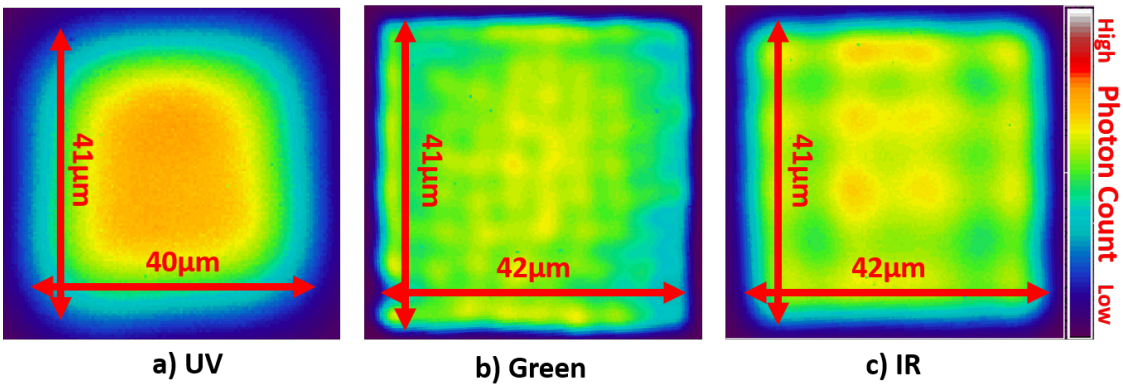

Figure 4.6.: The figure shows the beam profiles of the different wavelengths. The profiles were measured at the sample plane with a camera. Each beam profile is square shaped with a diameter of about 40 µm. The UV beam profile was obtained using a beam shaper. The green and IR beam profiles are obtained by projecting a mask.

4.2.3. Sample Observation

The LIPSS setup does not have an extra sample observation, but the translation between the sample position in the two-beam interference setup and the LIPSS setup has been measured by using a camera. This allows for a reproducible placement of the samples in the right position with an accuracy of 2 µm.

4.3. Film Thickness Measurement

To measure the thickness of the liquid layer on the sample during the confinement experiments, a setup based on the principle presented in Section 2.4 was implemented.
The setup consists of a white light lamp and a spectrometer.
The setup was needed to see the influence of the layer thickness on the structures forming in the two-beam interference experiments and also being able to estimate the absorbed fluence in the experiments by the layer. As the layer evaporates after a short time, a measurement setup within the experimental setup was needed. The available commercial setup could not be included in the experiment.
In order to obtain a highly localised measurement over a narrow spatial region, the white light is focused using an achromatic lens with a short focal length. As the working distance of the SSO is small, the angle of incidence of the white light is almost 70°, since for smaller angles the path would be blocked by the SSO. Due to the large angle, the focus on the sample has an elongated line-like character in x-direction, but as the liquid drop forming layer is applied from the top it is expected that the film thickness does not vary significantly in x-direction.
The liquid itself is applied at the top of the sample by hand, using a laboratory bottle with a small outlet. The liquid than runs down the sample and wets the complete surface.
The light reflected from the sample is collected by a lens and focused into a fibre, connected to the spectrometer (Ocean Optics, HR4000).
The setup was tested using a sample with a SiO_x layer on an SiO_2 substrate. The thickness of the layer was measured using the presented film thickness setup and additionally tested using a commercial film measuring device. The results of both measurements can be seen in Figure 4.7, showing a deviation of about 7%. In the calculation the refractive index of the layer is assumed to be constant over the complete displayed wavelength range. For the calculation of the thickness the same value was taken as in the commercial analyser ($n_{SiOx} = 1.95$). The used setup measured a thickness of 1.5 µm, while the commercial device measured 1.42 µm. The predicted range the setup may be used at is between 1 and 10 µm, as for shorter layer, not enough extrema are present. For larger layers, the extrema can not be differentiated from the noise.

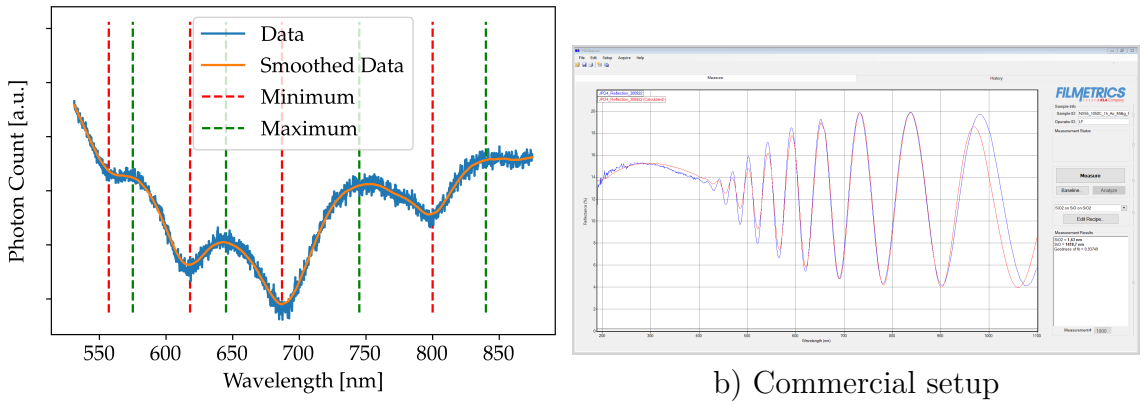

a) Setup in this work

b) Commercial setup

Figure 4.7.: The figure shows (a) the interference spectrum used to determine the thickness of the SiO_x layer in order to evaluate the measurement setup. The calculated thickness was 1.5 µm. (b) is the measurement of the same sample using the commercial layer thickness measurement device FS20-UV by Filmetrics. This device measured a thickness of 1.42 µm. This leads to the conclusion, that the implemented thickness measurement setup produces reasonably good results.

4.4. Sample Characterisation and Preparation

The experiments were done on samples consisting of a gold surface, on a thin chromium layer on a glass substrate. The thickness of the gold layer is about 300 nm, while the chromium layer is only a few nanometres thick. The purpose of the chromium layer is to increase the adhesion of the gold layer to the glass substrate.
The samples were provided by the Max Planck Institutes (MPI) for Biophysical Chemistry and are made via evaporation. A sketch of the sample can be found in Figure 4.8. The comparatively large thickness of the layer is necessary to be sure

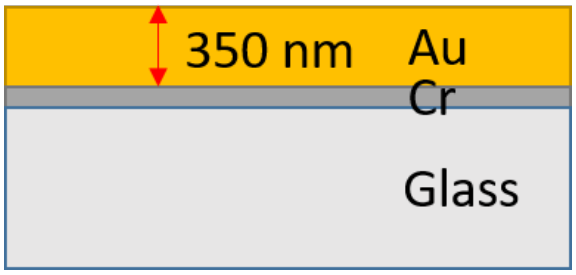

Figure 4.8.: Sketch of the samples used in the experiments, with a gold top layer of about 350 nm thickness, followed by a thin chromium layer to increase adhesion. The layer is a few nanometres. The substrate is a glass substrate, which is about 4 mm thick.

that there is no backscattering of the light wave from the gold chromium interface. The penetration depth is given by

$$\delta_p = \frac{1}{\alpha}, \tag{4.6}$$

with α the absorption coefficient introduced in 2.1.2 and calculated via equations 2.33 and 2.37 with the dielectric function for evaporated gold taken from [72].
Table 4.1 shows, that the penetration depths for all regarded wavelength are about one order of magnitude smaller than the layer thickness, therefore backscattering of the pulse can be neglected. It is noteworthy, that especially for the femtosecond laser, the actual penetration depth is even smaller, due to additional two-photon absorption which is not included in the calculation.
The root mean square roughness of the sample was measured by the AFM described in 3.3.2, to be $R_{rms} = 1$ nm. The roughness was measured at random positions on the samples. As described in Section 2.2.1, SPP may be excited from rough spots

λ [nm]	κ	δ_p [nm]
343	1.83	14.91
515	1.98	20.67
1030	6.85	11.97
355	1.82	15.50

Table 4.1.: The table shows the penetration depth of radiation of each of the used wavelength on gold. The data for the extinction coefficient are taken from [72].

on the surface, thus it is necessary to have a smooth surface to avoid multiple SPP waves that may interfere and cancel out each other.

5. Deterministic Periodic Surface Structures under Transparent Confinement

In this chapter the generation of structures under a thin transparent confinement layer is investigated. The structures were produced at two different pulse durations (ps and fs) via two-beam interference, for which the theoretical background is described in Section 2.5.1 and the used setup is described in Section 4.1. All the presented structures are the result of single pulse experiments. The size of the beam on the sample was about 8 µm x 18 µm, and as the period of the structures was about 500 nm.
Both liquid (ethanol) and solid (SiO_2) confinement layers with different thicknesses were studied.

5.1. Liquid Confinement Layer

As discussed in Section 2.6, the presence of a transparent confinement layer does alter the topography of the generated structures. In this section the structures that form under a liquid confinement layer after irradiation via two-beam interference are analysed. In addition, the thickness of the layer is measured, to estimate the fluence reaching the sample surface. Knowledge of the layer thickness is necassry as the for a short pulse duration, the absoption due to TPA (described in Section 2.1.3) may be high for thick layers. Then the changes in the results depending on the thickness of the film is analysed.

One possible way to include a liquid layer in the experiments is by wetting the sample using a liquid and cover it by a thin quartz cover glass. This makes sure that the liquid is covering the complete sample and using spacers between the glass

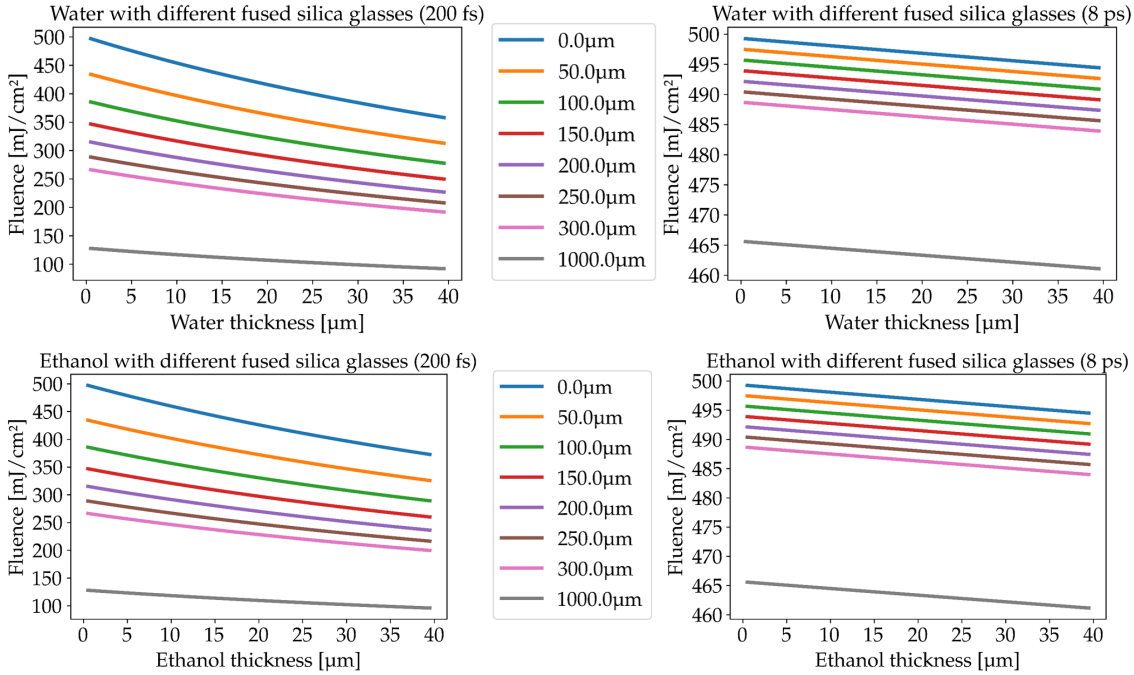

Figure 5.1.: The figure shows the reduction of the fluence for a system consisting of a quartz and a liquid (water or ethanol) layer for various thicknesses, for laser with pulse durations of 200 fs (left) and 8 ps (right). The change in fluence is calculated using equations 2.41 and 2.42. The initial fluence was in all cases 500 mJ/cm^2. The linear- and two-photon absorption parameters for quartz, ethanol and water are taken from [41].

and the sample, it is possible to control the thickness of the liquid layer.

The problem with the additional quartz layer is that it also absorbs some of the light via two-photon absorption. A graph showing the change of fluence after a quartz and a layer of either water or ethanol can be found in Figure 5.1. The graph makes it clear that a quartz cover glass of a few hundred µm thickness already absorbs almost half of the laser energy for the 200 fs laser beam. Therefore, an additional quartz layer was not used, but only the liquid layer was applied and its thickness was measured using the setup descriebed in Section 4.3. A version of Figure 5.1 showing the fluence of the beams after a liquid layer without quartz can be seen in Figure 5.2. It is visible that the absorption for water is for 200 fs slightly larger than for ethanol, while for 8 ps there is hardly any absorption. The challenge is then to provide a homogeneous spread of the liquid on the sample. Especially water does tend to form droplets instead of a homogeneous layer, while ethanol and isopropanol do form a more homogeneous layers as their surface tension is much lower than that

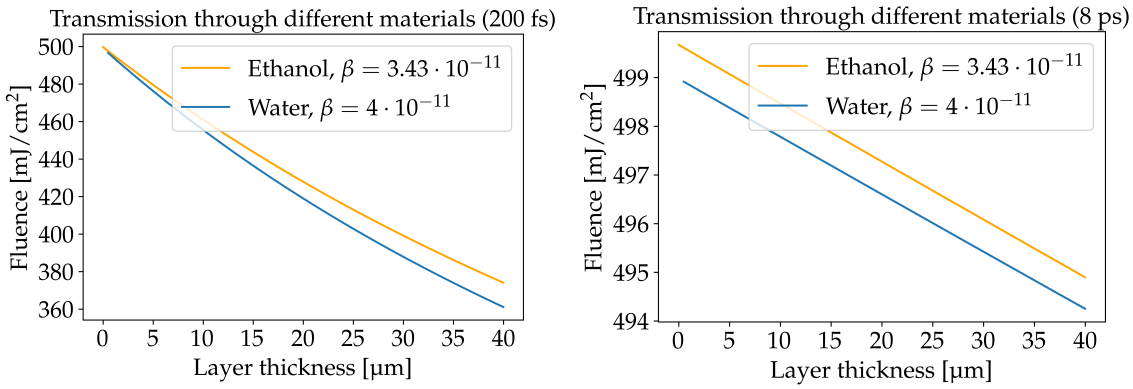

a) Pharos : $t_p = 200$ fs

b) Hyper Rapid : $t_p = 8$ ps

Figure 5.2.: The figure shows the transmission through a water and ethanol layer depending on the thickness of the layer for two pulse durations of (a) 200 fs and (b) 8 ps. The β is given in cm/W. The offset of the lines on the right is due to the different reflectivities of the layers. The linear absorption coefficients for water and ethanol are taken from [110] and [71] and the two-photon absorption coefficient from [111] and [41], respectively. The values given in the literature for the two-photon absorption coefficient are for a smaller wavelength (266 nm) and therefore the absorption is probably slightly over estimated.

of water [112].

Due to the large difference in the absorption for the different laser pulse lengths, both laser sources (presented in Section 3.1) were used for the production of periodic structures via two-beam interference.

5.1.1. Pharos

For the first experiments, the layer was chosen to be larger than the measurable thickness and only the incident fluence has been varied. The results are compared with structures created using the same incident fluence without a layer. The used incident fluences were 500, 600 and 730 mJ/cm^2. The SEM pictures of the results for these incident fluences can be seen in the Figure 5.3. In this fluence range no substantial difference can be observed in the appearance of the structures. However, it is obvious that the height modulation of the structures is greatly reduced when the layer is present. It is visible in all structures under the layer, that the height of the structures increases with increasing distance from the central area. The height of the structures in the central area is independent of the incident fluence, though the height at the outer regions does increase at higher fluences, from about 30 nm to 80 nm for 500 and 730 mJ/cm^2, respectively.
While the structures without the confinement layer all show wall formation, the structures under the layer are formed through surface swelling. In a few places, possible void openings may be seen, e.g. inside the green square shown in Figure 5.3. Additionally, there is no debris on the structures, when the layer was present. This may be the case, as there is no material ejection when the structures form due to surface swelling compared to surface wall formation.
The minima of the structures forming after irradtion without a confinement layer are around 100 nm and thus in same range as given by the penetration depth for 343 nm in gold. The height of the walls and thus the maxima of the structures a up to a few hundred nanometers and so much larger than the depth at the minima. Such a larger wall height of also observed in the simulations shown in [96]. That in case of a transparent confinement layer is consistent with the findings of [87] and [85], presented in Section 2.6.

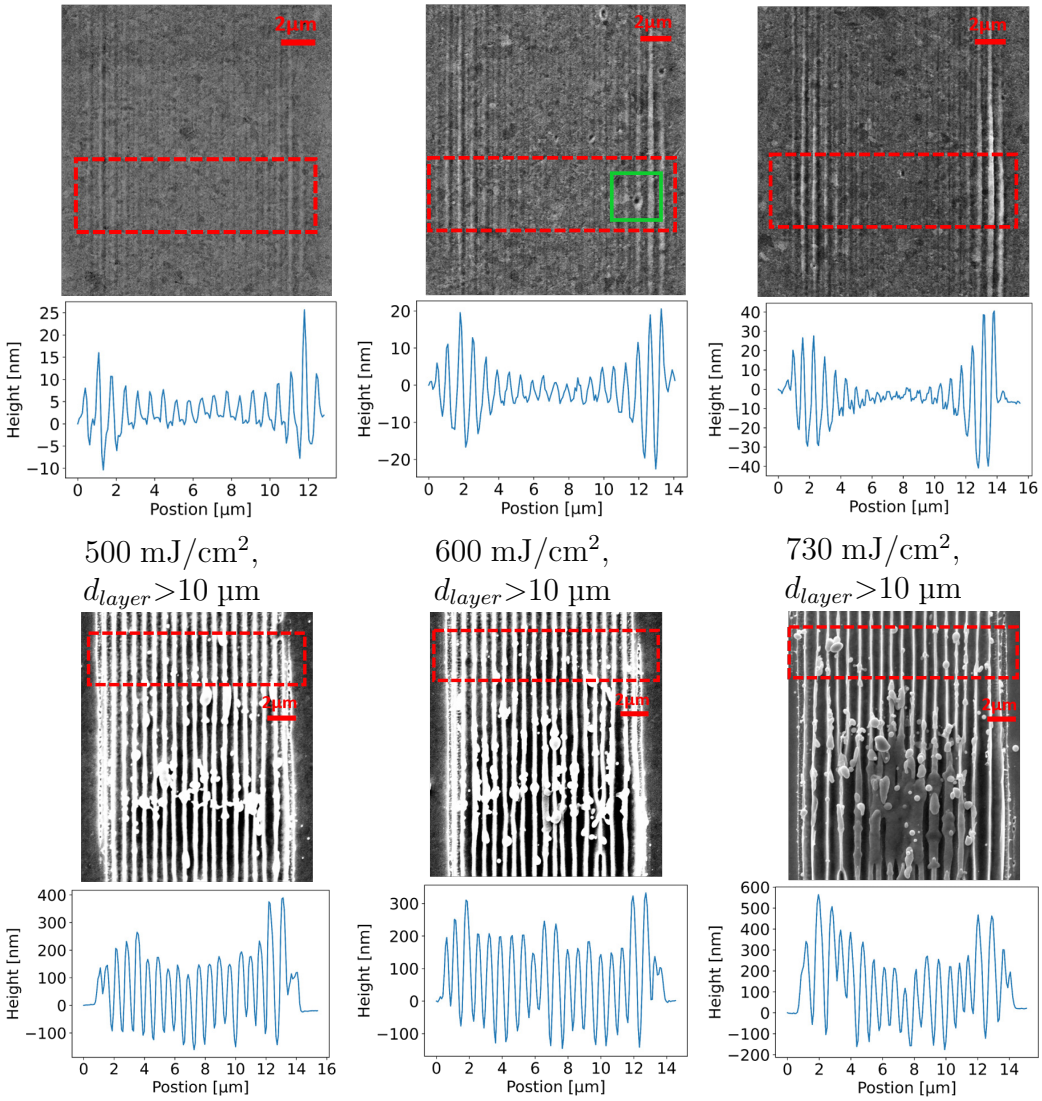

Figure 5.3.: The figure shows the structures that form under a thick ethanol confinement layer on gold produced via two-beam interference using the 343 nm, 200 fs beam (top). The incident fluences were 500, 600 and 730 mJ/cm^2. For comparison the structures are shown using the same fluences without the layer (bottom). Underneath each picture the AFM height measurement of the structures is presented. The data were recorded in the red squares. Inside the green square a possible void opening to the surface is visible.

Afterwards, for a fixed incident fluence of 600 mJ/cm^2 different layer thicknesses were investigated. Here the layer thickness is measured using the setup presented in 4.3. The used layers were about 3, 2, 1 µm and below 1 µm. The results of the experiments are shown in Figure 5.4. The fluences behind the layers are calculated to be 580, 588, 593 and 596 mJ/cm^2 and are almost equal. The measurement of the layer thicknesses are shown in the Appendix A in Figure A.1.

From the series shown in Figures 5.3 and 5.4 two trends become obvious. As the layer is getting thinner, the structures in the central region are getting more and more suppressed. For the thinnest layer of less than 1 µm, the structures in the middle are completely vanished. At the same time another trend can be observed. With reducing layer thickness the structures on the sides grow higher. Here the height increases form 60 nm for a 3 µm layer to about 250 nm for the thinnest layer of less than 1 µm. A possible explanation for the observed trends in Figures 5.3 and 5.4 may be a pressure wave forming in the layer and pushing the structures down- and outwards. Such a pressure bubble has detected when irradiating gold under a liquid layer with a short laser pulse [113, 114]. The production of the pressure bubble may either be explained by laser-induced breakdown [114] or by heat transfer from the gold surface to the layer [115]. In a laser-induced breakdown, a laser beam may cause the creation of a plasma cloud, which is followed by a pressure bubble in a liquid [100] if the intensity of the laser is above a certain threshold, the breakdown has also been seen in thin layers [116]. In water, the threshold was measured to be 1.4 J/cm^2 for a 300 fs and 1.1 J/cm^2 for a 100 fs laser (at 580 nm) [117]. Despite the lower mean fluence in the experiments, this threshold may be reached at the maxima of the interference pattern, though the exact threshold for ethanol and for 343 nm could not be found in the literature. The laser-induced breakdown was found to start about 200 fs after reaching the threshold [100] and should thus not disturb the interference process, but could influence the structure formation.

Another possibility is that the laser heated surface transfers the heat to the layer [118–120]. The layer then expands creating a pressure bubble, as has also been reported for ablation of zinc in an ethanol environment [121].

The formed pressure bubble may dissipate at the sides, but not in the center, so the center of the structured region is affected most by the bubble. The thinner the layer, the closer a pressure bubble may form to the surface. Similarly, the less fluid is available to dissipate the heat, the more the layer can heat up. Therefore, the observed effect is expected to be stronger for a thinner layer.

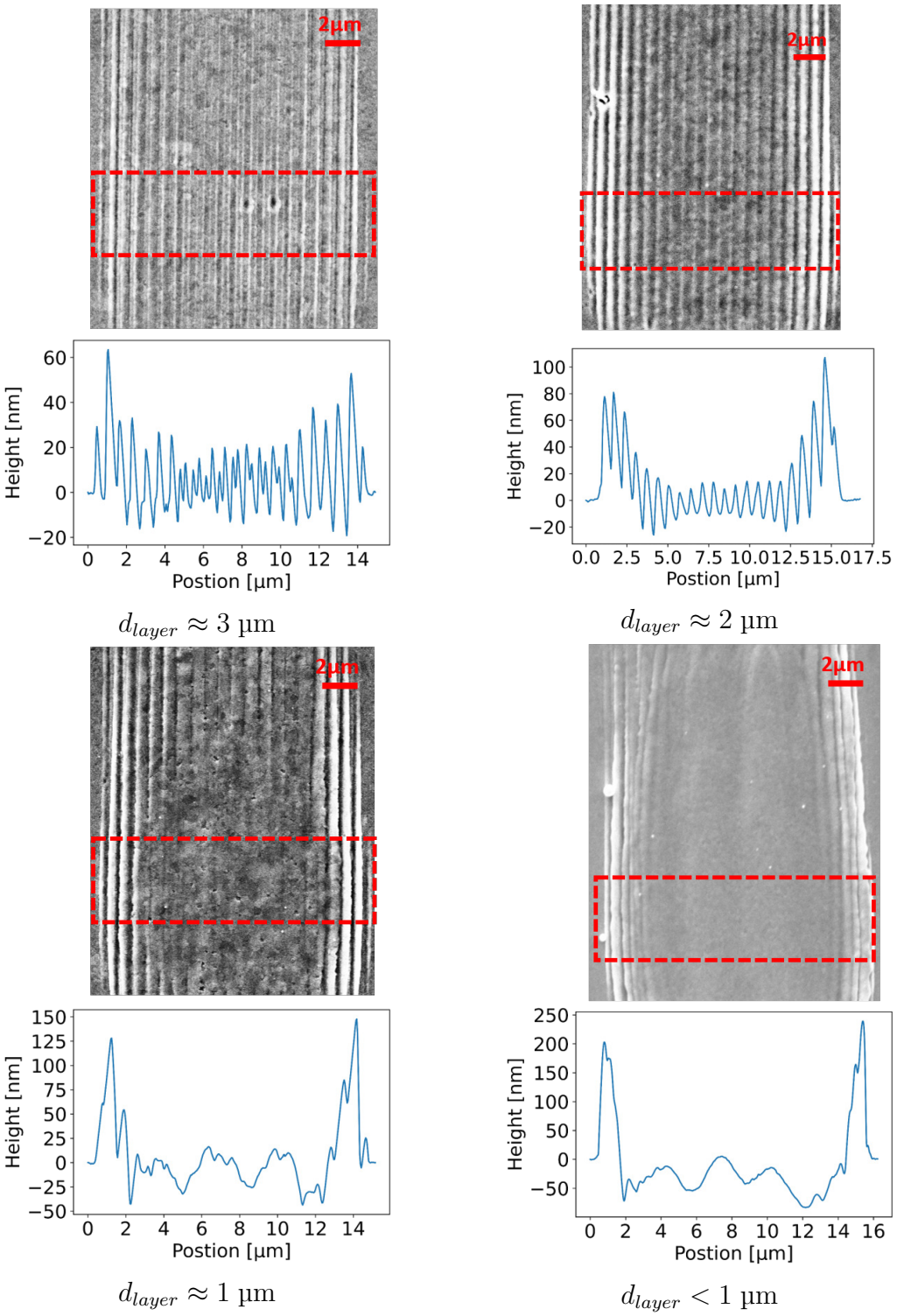

Figure 5.4.: The figure shows SEM pictures of the structures obtained at different ethanol layer thicknesses on a gold surface. The wavelength of the laser is 343 nm and the pulse duration 200 fs. The incident fluence was 600 mJ/cm^2 in all pictures. Underneath each picture AFM height measurement of the structures contained in the red squares are displayed.

5.1.2. Hyper Rapid

The pulses of the Hyper Rapid laser source, with a pulse duration of 8 ps are less affected by the layer as can be seen in Figure 5.2. On the other hand, the longer pulse duration could lead to a slightly broader heat distribution and thus to melted structures. Like for the other light source, the first experiments are done using a thick layer. As can be seen in Figure 5.2, the absorption due to the layer is negligible. The results of these experiments are shown in Figure 5.5. Using the longer pulse, the structures look more similar with and without the ethanol layer than for the shorter pulse, in both cases the central region is melted. There is no clear connection between the depth of the ablated region and the presence of the layer. Though [98] found deeper crater when a layer was present (for 515 nm, 6.2 ps at 7.8 J/cm^2). However a difference can be seen in the periodic structures on the sides of the irradiated areas. While the structures are forming by surface wall formation without a layer, the periodic structures under the layer form via surface swelling with a few void openings also being present. It is apparent, that with the layer, no structures form via surface wall formation but go from surface swelling with void openings directly to broad melting.

At lower fluecnes (125 and 166 mJ/cm^2), a thick ethanol layer was used. The layer thickness was larger than what could be measured using the measurement setup. The results of the experiments can be seen in Figure 5.6. Like for the higher fluences, the structures under the layer are forming via surface swelling or are melted (for 166 mJ/cm^2) and no structures form by surface wall formation. With heights of about 60 nm (for 125 mJ/cm^2) and 80 nm (for 166 mJ/cm^2) the periodic structures under the layers are smaller than the ones without the layer with 250 nm and 300 nm for 125 mJ/cm^2 and 166 mJ/cm^2, respectively. For the higher fluence it is visible that the structures are melted in the central region if the layer is present, while without the layer structures have formed by wall formation. It appears that the liquid lowers the threshold fluence for melting.

When comparing the structures formed using the different laser sources, the major difference is that the height reduction for the central structures and the elevation of the outer zones does not occur with the 8 ps pulse.

When taking a look at the threshold fluence for laser-induced breakdown for the longer pulse duration, [117] gives for water a threshold fluence of 2.6 J/cm^2 for 3 ps (at 580 nm) and 16.8 J/cm^2 for 60 ps (at 532 nm). Assuming the threshold for the experiments lies in the same order of magnitude, this value was not reached.

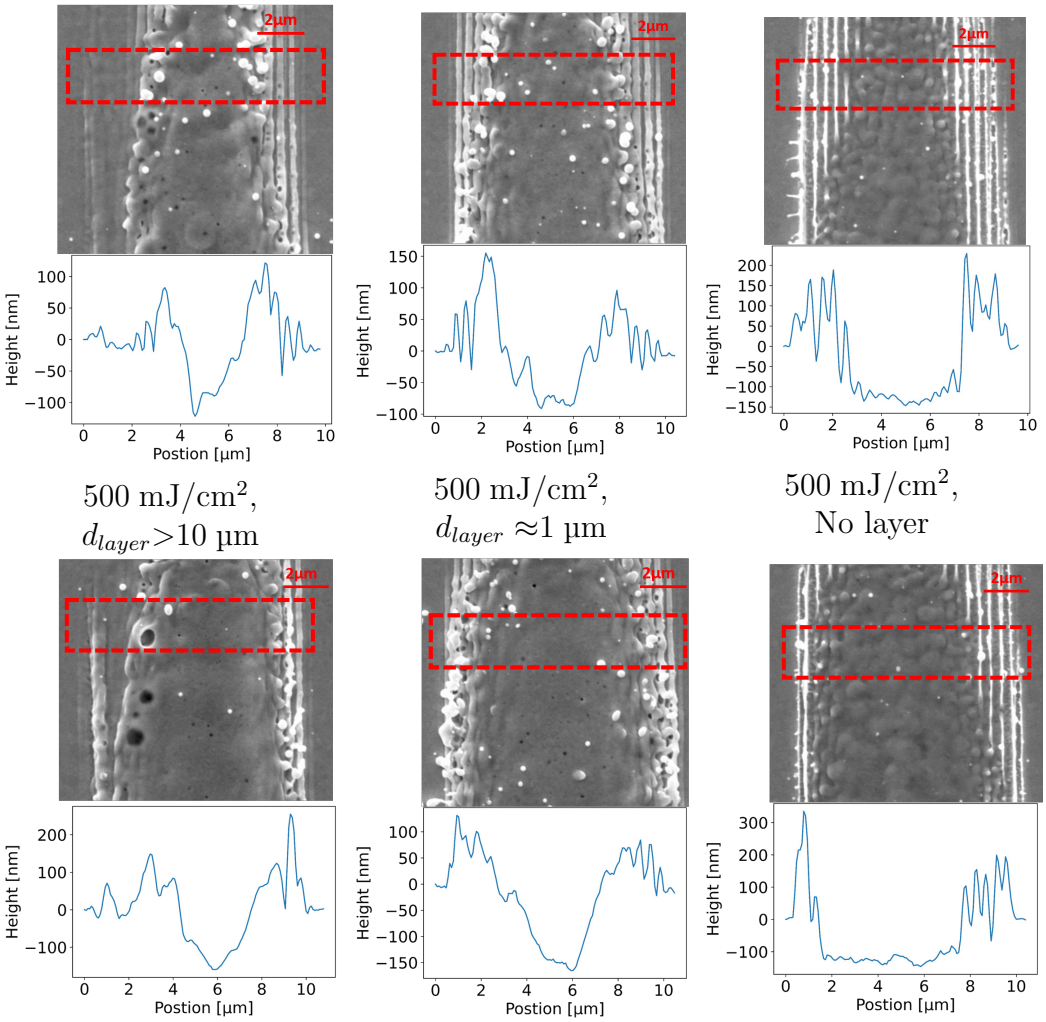

Figure 5.5.: The figure shows SEM pictures of the structuring results at 355 nm with a pulse duration of 8 ps at different fluences. In the top row, the fluence was 500 mJ/cm^2, in the bottom row 600 mJ/cm^2. The AFM measurement of this structures were taken in the area indicated by the red square and are shown under each picture.

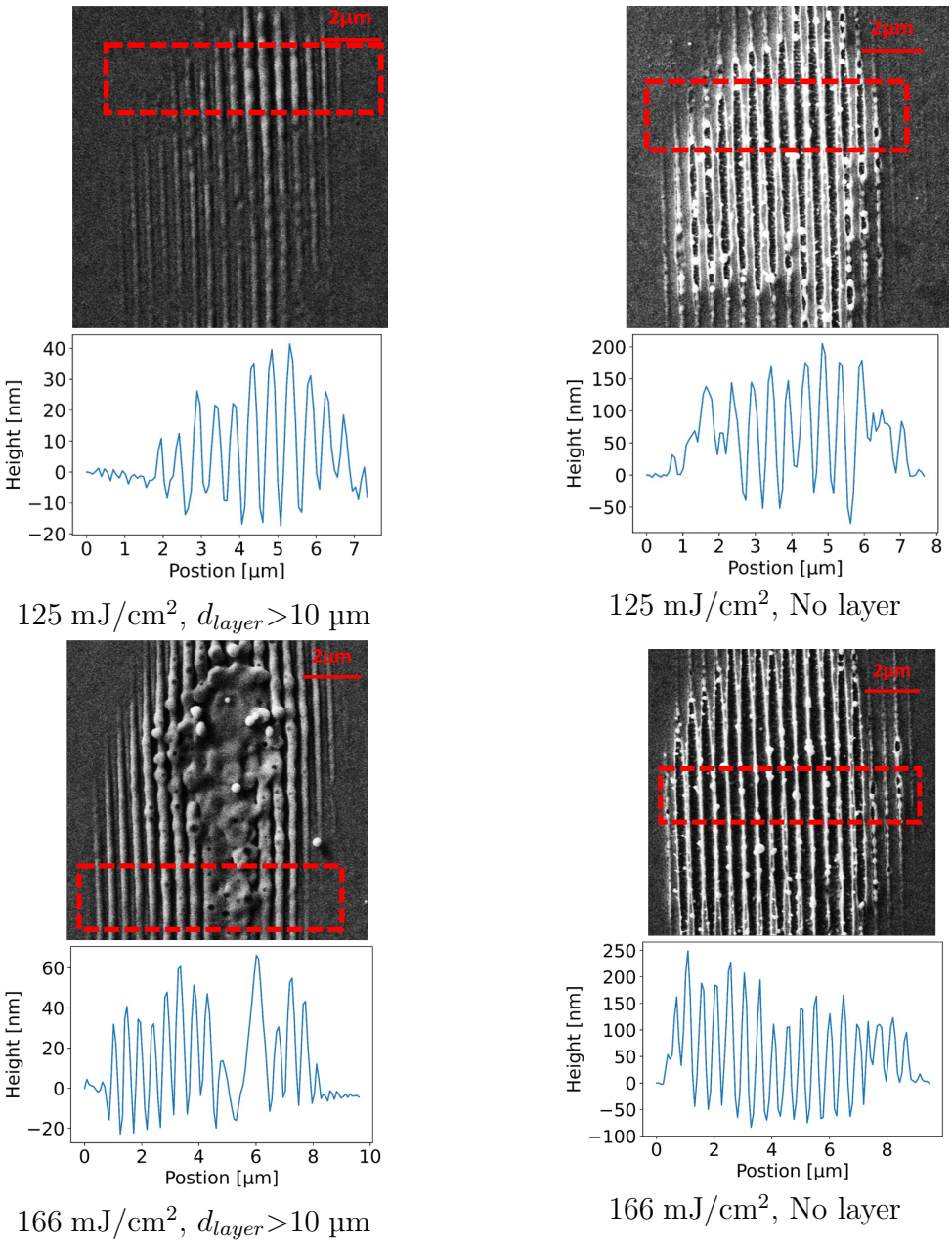

Figure 5.6.: The results of the irradiation events using 355 nm, 8 ps laser pulses under a thick ethanol confinement layer on gold with lower fluences are shown. In the top row, the fluence was 125 mJ/cm^2 and in the bottom row 166 mJ/cm^2. The AFM measurement of this structures can be found underneath each picture, with the red square showing the region in which the measurement has been taken.

5.2. Solid Confinement Layer

In addition to a liquid layer, also samples with a solid confinement were investigated. These samples are similar to the samples presented in 4.4, but have an additional layer of SiO_2, for one set of samples with a layer thickness of about 50 nm and one set with 325 nm thick layers. As these layers are too thin to be measured with the apparatus described in 4.3, a commercial setup was used which has a larger range of possible layer thicknesses. The used device was a Filmetrics FS20-UV, which uses the a similar principle as the one described in 2.4. The measurement of the thickness of two samples can be seen in Figure 5.7. The samples are irradiated by both laser

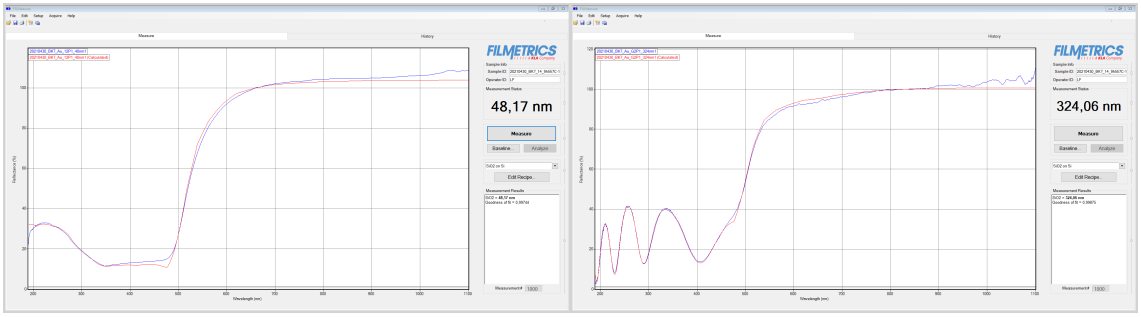

50 nm 325 nm

Figure 5.7.: Measurements of the film thickness of the samples with a SiO_2 layer. The film measurement shows the reflected spectrum of the sample (blue) with a best fit estimate (red). The measured film thickness was 48.17 nm and 324.06 nm for the thin film and thick film, respectively. The measurement device was a Filmetrics FS20-UV and the data is evaluated by the software FILMeasure.

systems using the third harmonic (UV) beams of the sources.

5.2.1. Pharos

The irradiations were done in the same manner as for the liquid confinement layer but on the sample with the solid layer.
The experiments were done in the fluence range of 100 to 1000 mJ/cm^2. For a fluence of 100 mJ/cm^2, no structures were visible, but above 200 mJ/cm^2 structures started to appear (Figure 5.8). Increasing the fluence, more structures develop and for a fluence of 1000 mJ/cm^2, the structures start to melt and vanish. Figure 5.9, shows the structures at 400 and 1000 mJ/cm^2. The results are than compared to structures under the solid confinement layers of either 50 nm and 325 nm thickness.

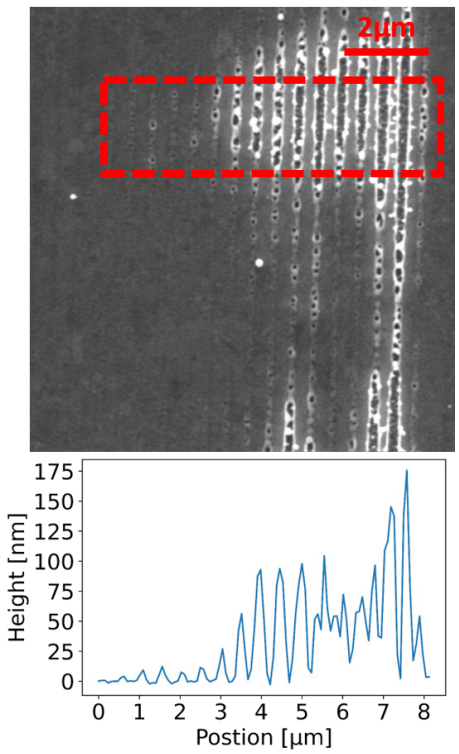

200 mJ/cm^2

Figure 5.8.: The figure shows the structures forming on the gold sample using a fluence of 200 mJ/cm^2 without a layer. The laser had a wavelength of 343 nm and a pulse duration of 200 fs. The AFM measurement can be found under the picture and was taken from the region indicated by the red square.

For the thin layer the structures start to appear at 200 mJ/cm^2 as well. More structures become visible at 400 mJ/cm^2 and the structures look comparable to those without layer. The pictures are shown in Figure 5.9. In both cases at 400 mJ/cm^2 there are droplets on the structures as well as a melted part in the lower right corner. In contrary to the liquid layer, here the homogeneity of the structures with and without layer do not differ that much. While the structures show wall formation without the layer, they are formed under the layer by surface swelling. The height of the structures are reduced by the layer, from 400 nm (400 mJ/cm^2, no layer) to 100 nm (400 mJ/cm^2, 50 nm SiO_2). Debris was present in both cases, even forming in the same place. For the thicker SiO_2 layer of 325 nm, shallow structures were formed under the layer at a fluence of 200 mJ/cm^2, without removing the layer. Figure 5.11 show the structures under the layer. At fluences of 300 and 400 mJ/cm^2 clearly visible structures were forming and the layer was removed from the surface

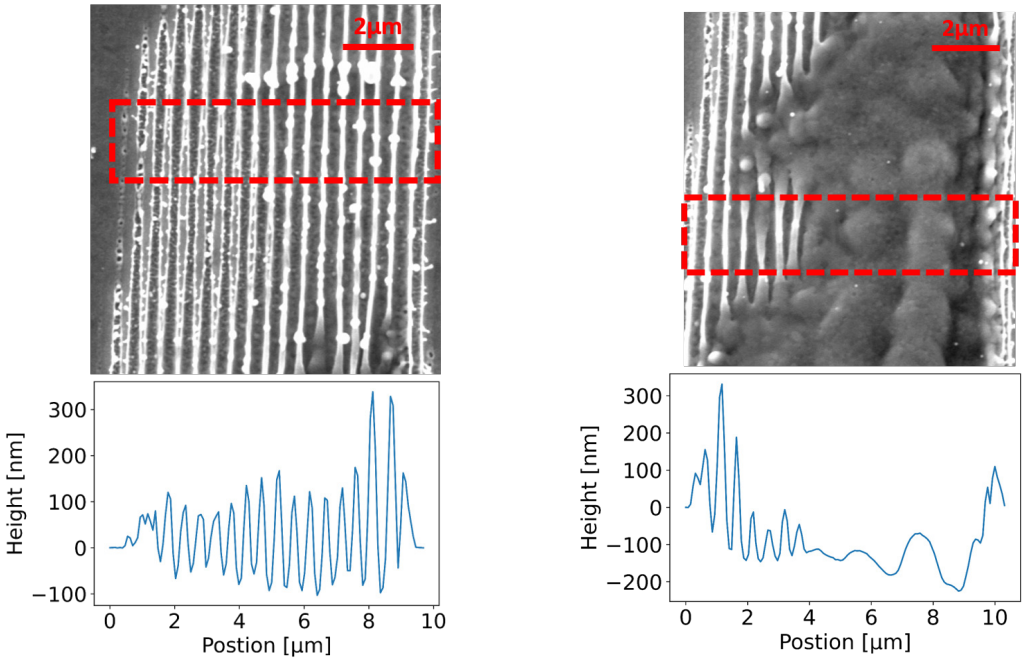

a) 400 mJ/cm^2 b) 1000 mJ/cm^2

Figure 5.9.: The figure shows the structures forming on the gold surface without a layer, irradiated with a 343 nm laser with a pulse duration of 200 fs. The fluence was a) 400 mJ/cm^2 and b) 1000 mJ/cm^2. Under each picture is the AFM height measurement of the region indicated by the red square shown.

(Figure 5.12). The structures were formed solely by surface swelling and no debris can be found. Their height (40 nm) was lower than in the case of the thin SiO_2 layer (100 nm).

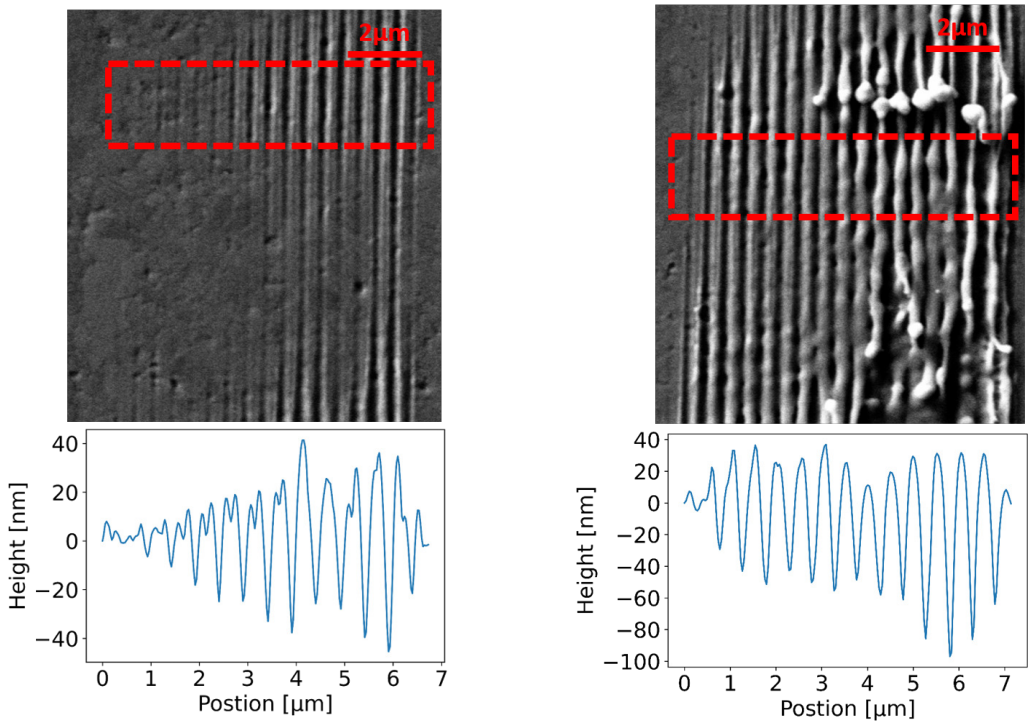

a) 200 mJ/cm^2 b) 400 mJ/cm^2

Figure 5.10.: The figure shows the structures forming on a gold sample covered with a SiO_2 with a thickness of about 50 nm. The laser had a wavelength of 343 nm and a pulse duration of 200 fs. The structures form after irradiation with a) 200 mJ/cm^2 and b) 400 mJ/cm^2. The AFM measurement of this structures taken in the regions indicated by the red square are shown under each picture.

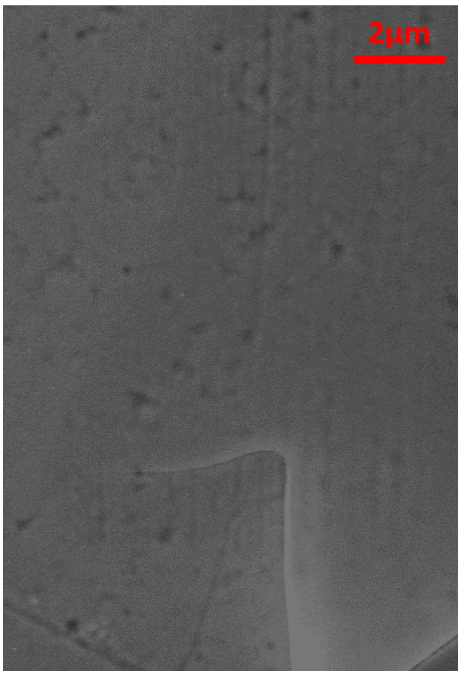

200 mJ/cm^2

Figure 5.11.: The figure shows a gold surface with 325 nm SiO_2 confinement layer after irradiation with 200 mJ/cm^2 pulse. There are slightly visible structures under the layer, but the layer is still for most part intact. For this picture there is no AFM measurement, as the layer is still on the sample.

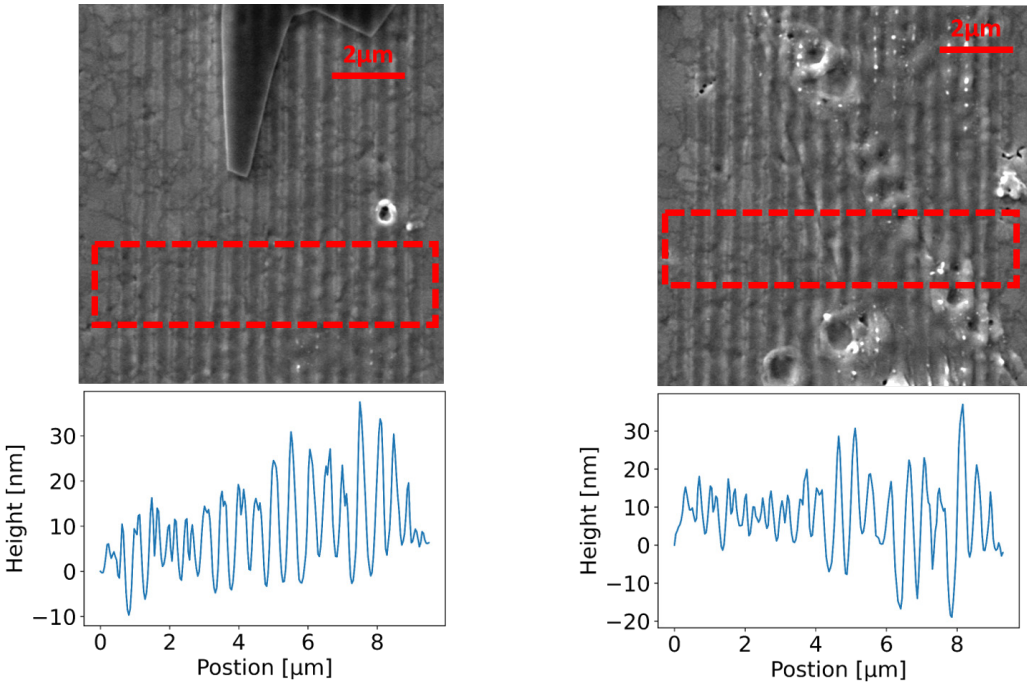

a) 300 mJ/cm^2 b) 400 mJ/cm^2

Figure 5.12.: The figure shows SEM pictures of the structures forming on a gold surface under a solid SiO_2 layer of 325 nm thickness at a fluence of a) 300 mJ/cm^2 and b) 400 mJ/cm^2 using a 343 nm laser with pulse duration of 200 fs.The AFM measurement of this structures can be found under each picture. The red square indicates the region the height measurement was taken.

5.2.2. Hyper Rapid

In these experiments the samples were irradiated using the two beam interference technique to create gratings on the sample with a period of about 500 nm. The fluence was ranging from 100 to 1000 mJ/cm^2.

When no confinement layer is present, there are no visible structures forming at a fluence of 100 mJ/cm^2, only for fluences above 200 mJ/cm^2. The structures at 200 mJ/cm^2 can be seen in Figure 5.13. For the fluences between 300 and

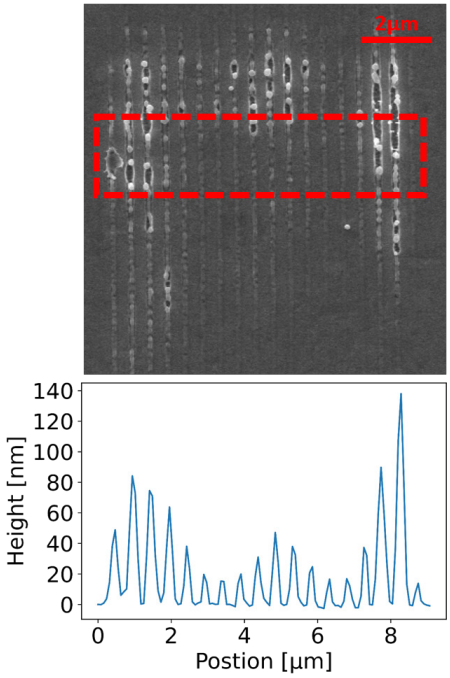

200 mJ/cm^2

Figure 5.13.: The figure shows a SEM picture of the periodic structures appearing on a gold sample. The fluence was 200 mJ/cm^2 at a laser wavelength of 355 nm and a pulse duration of 8 ps. The AFM measurement are taken in the area within the red square and is shown under the picture.

380 mJ/cm^2, the structures are shown in Figure 5.14. It is visible that the structures get covered by droplets, getting more at higher fluences. It may be noted, that there were no measures done to reduce the debris, like applying an air flow in front of the sample.

For the 50 nm SiO_2 layer, there are some structures visible at 200 mJ/cm^2. With and without layer, structures are formed by surface swelling.

At 300 mJ/cm^2 the upper part is ablated. The depth of the ablated region reaches

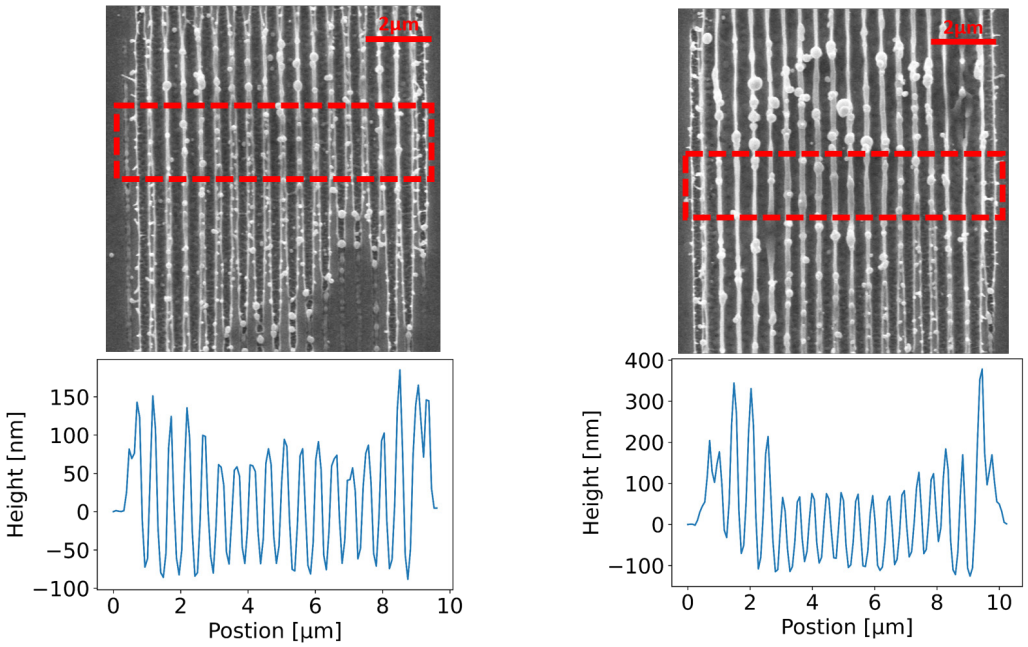

a) 300 mJ/cm^2 b) 380 mJ/cm^2

Figure 5.14.: The figure shows the structures, appearing after irradiation with a) 300 mJ/cm^2 and b) 380 mJ/cm^2 pulses. The wavelength of the laser was 355 nm and the pulse duration 8 ps. The AFM measurements were performed in the area indicated by the red square and the results can be found underneath each picture.

100 nm below the initial gold surface. In the ablated region, there are a few structures visible. The peaks of the structures are about 50 nm high.

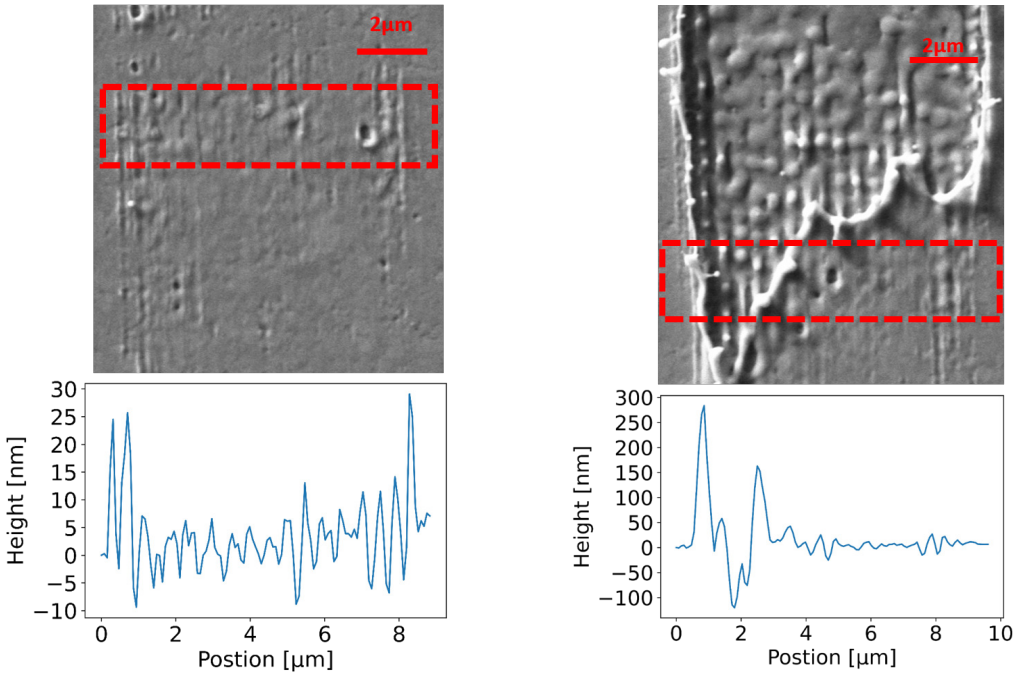

a) 200 mJ/cm^2 b) 300 mJ/cm^2

Figure 5.15.: The figure shows the results of irradiation of the gold sample with 50 nm SiO_2 layer with a fluence of a) 200 mJ/cm^2 and b) 300 mJ/cm^2. The wavelength of the laser was 355 nm and a pulse duration 8 ps. The AFM height measurement of this structures can be found under each picture and the profile was recorded in the region indicated by the red squares.

Irradiating the gold sample covered with a 325 nm SiO_2 layer at 200 mJ/cm^2 also show structures and the layer stays intact. As in the case without layer, the lowest fluence of 100 mJ/cm^2 was not enough to create visible structures on the sample. At higher fluences of 300 and 380 mJ/cm^2 the SiO_2 layer gets ablated to a large extend and underneath there are structures present. For 300 mJ/cm^2 there are structures present in the complete irradiated area. At 380 mJ/cm^2, the upper part of the structures are melted and the structures vanished (Figure 5.16). The structures are again formed by surface swelling and are partly molten, but like before, no structures by surface wall formation were found. It was found that irradiation

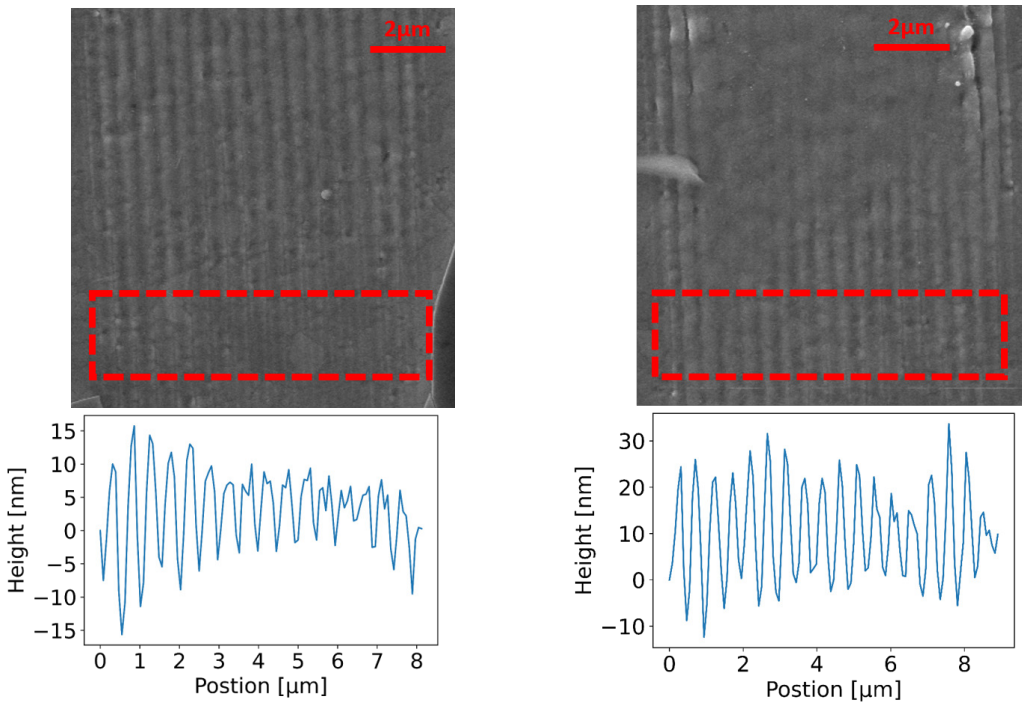

a) 300 mJ/cm^2 b) 380 mJ/cm^2

Figure 5.16.: The figure shows SEM pictures of gold sample with a 325 nm SiO_2 layer irradiated using a mean fluence of a) 300 mJ/cm^2 and b) 380 mJ/cm^2. The wavelength of the laser was 355 nm and the pulse duration was 8 ps. The red squares show the regions in which the AFM measurements were performed, with the height profiles shown under each picture.

under the 325 nm SiO_2 layer lead to no debris being present, together with an overall reduction of the height of the structures. Independent of the thickness of the solid layer, there was no instance of surface wall formation. Either periodic structures form by surface swelling or the surface is molten. For the 50 nm SiO_2 layer and

the 8 ps pulse, at 300 mJ/cm^2 a large region of the irradiated area is ablated, what was neither the case for the shorter pulse duration nor for thicker layer or without layer. This may be due to the time needed for the layer to be removed from the surface. If the thin layer is removed while the surface is still liquid (for times up to 1000 ps [49, 96]), the removal may strongly impact the gold surface, including a removal of part of the gold layer. The thick layer is likely to be stronger and hold longer on the surface, influencing the structure formation for a longer time and is probably removed at a time, when the surface is again mainly solid. The thin layer may be removed at a time when the surface is liquid and may thus remove parts of the surface.

The threshold for laser-induced breakdown in SiO_2 for a thin 150 µm SiO_2 sample was found to be about 10 J/cm^2 [116] (at 790 nm, 150 fs). Additionally, it is hard to imagine a bubble shaped pressure wave forming in the solid, causing a localised variation of the structures. Under none of the transparent confinement layers, structures formed by surface wall formation. This is in agreement with [85], who found in MD-TTM simulations, that the voids do not open under a liquid water confinement due to the pressure of the layer. The same seems to be the case for a solid layer.

The difference in the observed behavour with liquid and solid confinement may be explained as follows. A liquid confinement layer, especially of small thickness can easily be evaporated thus supporting the formation of a bubble above the irradiated area. The bubble then expands and creates a pressure distribution having its peak at the central region with decreasing pressure towards the outer zones. This may lead to material flow from the center to the outer regions in case of the liquid confinement. On the contrary, the solid confinement layer is not likely to evaporate and exerts a more uniform pressure to the irradiated area below. Therefore, it hinders the development of structures but does not facilitate a lateral flow of the material to the sides of the irradiated area.

6. Laser-Induced Periodic Surface Structures

In this chapter, the formation of LIPSS on gold after irradiation with a single laser pulse is investigated. Parts of the presented work here has also been published in [48] and [49]. Up to now, most investigations of LIPSS have been done using multipulse experiments [122–130], but there are also some studies of LIPSS produced with single pulse irradiation [52, 53, 55, 68, 131–133]. The benefits of single pulse generation of LIPSS is mainly in investigating the fundamental processes responsible for the emergence of these structures. This is the case especially when comparing experiments to simulations, as otherwise also the changes on the sample surface have to be taken into account after each pulse. This would result in an extreme increase in computational time for the simulation of LIPSS after hundreds or even thousands of pulses.

The results of experiments are compared to the predictions of the plasmonic theory to find out, whether the theory can be used to predict properties of the forming structures.

As has been explained in Section 2.2.1 it is not possible to couple light to SPP directly on a smooth sample. Therefore, the samples needed to be prepared in advance to enable the coupling. Line like defects on the surface were used that in the following will be called step edges. The step edges were produced applying two different techniques. The first was by inducing a scratch on the surface using a sharp razor blade. To obtain a straight line, the sample was moved underneath the razor blade using motorised linear stages. The form of the scratch includes a gap in the middle, down to the glass substrate. On both sides ot the gap there are upstanding walls of gold. The walls are of slightly different heights and shapes, likely due to the non-symmetrical form of the razor blade. An AFM measurement of a scratch, later used as step edge can be found in the left part of Figure 6.1.

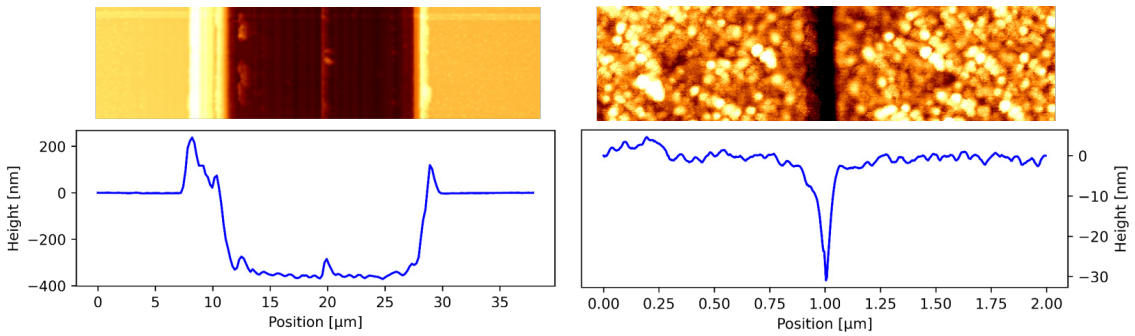

a) Razor blade step edge b) FIB groove

Figure 6.1.: The figure shows pictures of the AFM measurement and the height profile of (a) the razor-blade step edge and (b) the FIB groove. The razor blade edge is much broader and deeper than the FIB groove. The sides of the razor-blade edge are different, probably due to the asymmetrical shape of the razor-blade.

The AFM measurement shows that the walls besides the gap have heights of about 220 and 160 nm, respectively.

The other method of creating defects for the SPP coupling, are small gaps created via focused ion beam (FIB) irradiation. These were produced by Dr. Murat Sivis and Felix Kurtz from the IV. physikalische Institut of the Universität Göttingen.

The FIB works, by focussing ions onto a sample which damage the surface. The ions used are often gallium and sometimes helium ions. Similar to the REM, the ions are focused and directed via magnetic lenses. This can be used to precisely produce structures. An AFM measurement of the FIB structures can be seen in the right part of Figure 6.1. The FIB lines are much smaller than the scratches produced using the razor blade and they also do not have side walls. Due to the small width of the structures, the SPP may emerge on both sides of the FIB line with structures forming on both sides. All the presented experiments are done by single pulse irradiation under normal incidence.

6.1. Single Pulse LIPSS using Ultraviolet Light

First the step edge was irradiated with the Pharos laser system at 343 nm. The results of the experiments are then compared to the predictions of SPP theory of LIPSS described in 2.2 and 2.3.2.

For the measurement, beam energy E was detected by a photoelectric energy meter PE9-ES-C from Ophir Optronics Solutions at a position slightly behind the sample plane. The beam size A was measured using a Lu160 camera from Lumenera at the sample position. The fluence is then given by

$$F_{\text{inc}} = \frac{E}{A}. \tag{6.1}$$

The same method was used also for determining the fluences that follow.

The fluence was varied in the range of 130 to 350 mJ/cm^2. LIPSS were only observed in the range of 160 to 270 mJ/cm^2. The irradiation results for different flueneces can be seen in Figure 6.2. The experiments clearly show the emergence of periodic

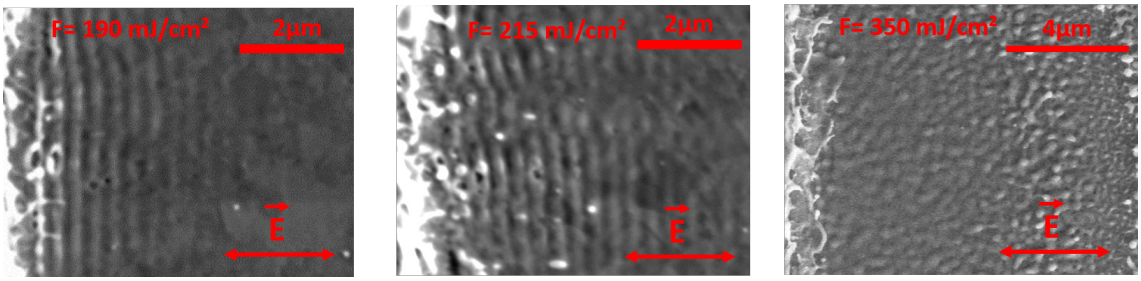

Figure 6.2.: The figure shows SEM pictures of the results of different irradiation events at varying fluences at 343 nm and a pulse duration of 200 fs on a gold sample with a step edge. The edge is located at the left side of each picture. The red arrows show the polarisation of the beam. The figure was published in [49].

structures using single pulse irradiation at a step edge, if the fluence is sufficient. The structures were only visible when using p-polarised light and no structures were obtained using s-polarised light, which is in agreement with the SPP theory as discussed in 2.2.

The post mortem shape of the structures was compared to the spatial shape of the energy input, given by the source function that will be described in detail in Section 6.2.2. The results are shown in Figure 6.3 for the fluences of 172 mJ/cm^2 and 192 mJ/cm^2. The comparison of the measured profiles with the calculated

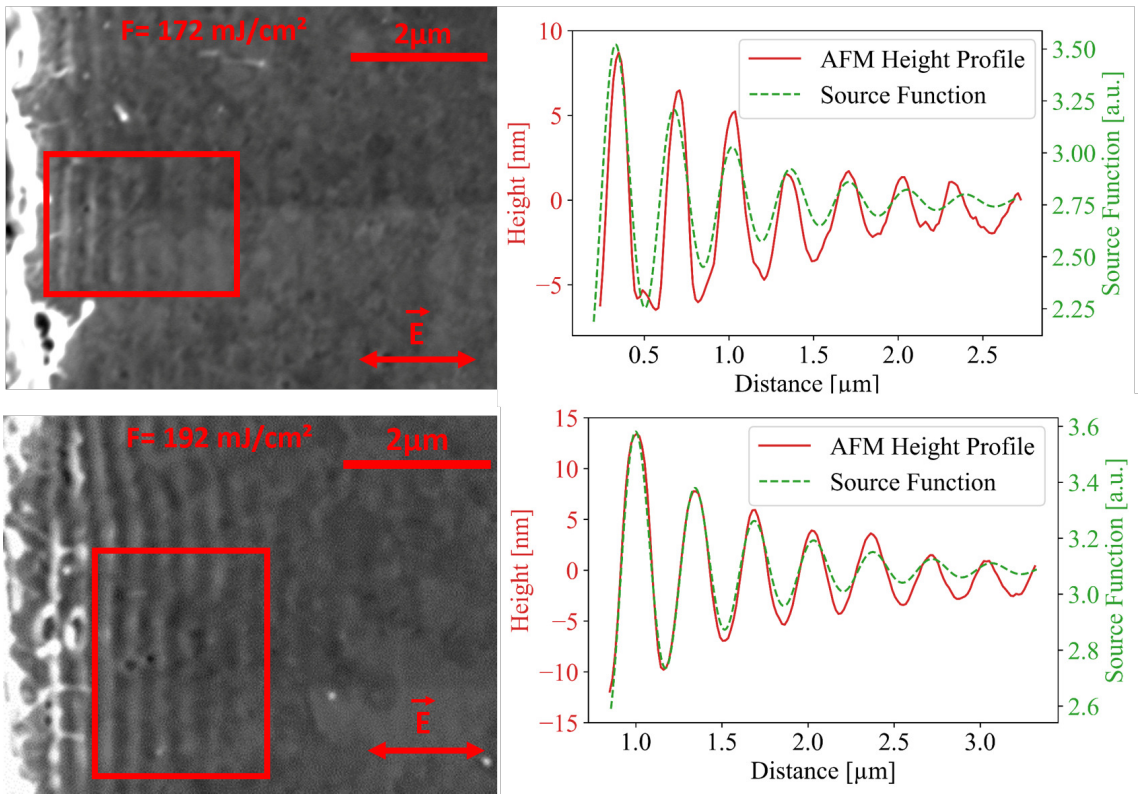

Figure 6.3.: The figure shows the structures forming at the step edge after irradiation with a laser beam at a wavelength of 343 nm and a pulse duration of 200 fs. The fluence in was 172 mJ/cm^2 in the top picture and 192 mJ/cm^2 in the bottom one. On the left are the SEM pictures of the structures, the red squares indicate the region over which the AFM hight measurements were taken. The structure heights are plotted at the right in red together with the calculated source function (green dashed line). For the AFM measurement, the 0 position was placed as the mean value of the height profile. The data from this figure were published in [49].

ones show good agreement for the periodicity. The decay of the profiles also agrees qualitatively, as both show an exponential decay, though the decay length in both cases differ.

For determining the periods of the structures two different methods are used. One uses the AFM or SEM data to determine the peak to peak distance over a number of structures. The other method uses the power spectrum of the measured height profile [134]. Figure 6.4 shows a height profile measurement of the AFM together with the power spectrum of that profile. Both methods deliver slightly different periods: measuring the distance of the maxima leads to 344 nm, while the power spectrum results in a period of 342 nm. Both methods were used to measure the

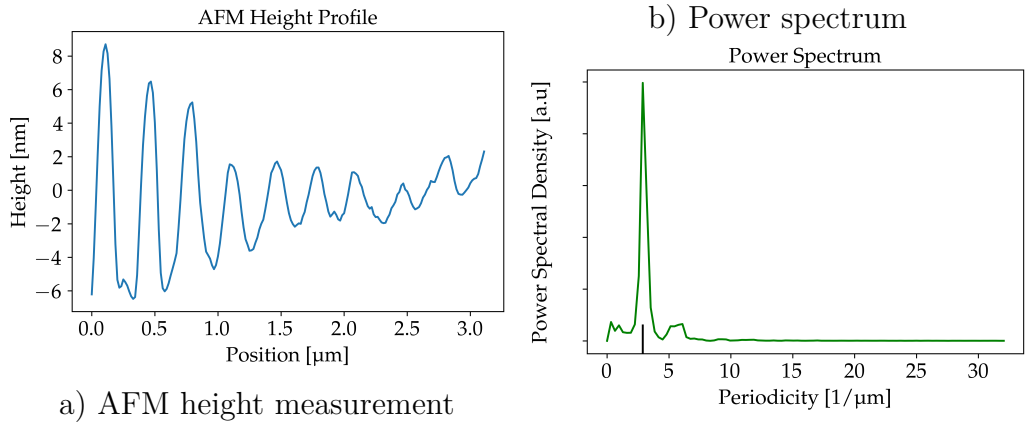

a) AFM height measurement

Figure 6.4.: The figures shows a) the AFM height measurement of the LIPSS structures at a fluence of 172 mJ/cm^2 and b) the power spectrum of the height profile. The inverse of the periodicity peak then gives the period. In this example, the period given by the power spectrum is about 342 nm and if taking the mean distance between the peaks in the height profile 344 nm.

periods of the structures for fluences from 170 to 270 mJ/cm^2. The periods hardly vary for the different fluences and no clear trend can be seen. The results are shown in Figure 6.5. The mean period combining both evaluation methods is 338 ± 10 nm. This number is in good agreement with the calculated period by using the dielectric functions of Johnson and Christy [135] and Olmon et al. for evaporated gold [72] and equation 2.75, yielding 340 and 344 nm, respectively.

Blumenstein et al. [136] measured the reflectivity of gold at different electronic temperatures. From the reflectivity, the dielectric function may be determined. Figure 6.6 shows the real and imaginary part of the dielectric function of gold for different electronic temperatures as measured by Blumenstein et al. Using these

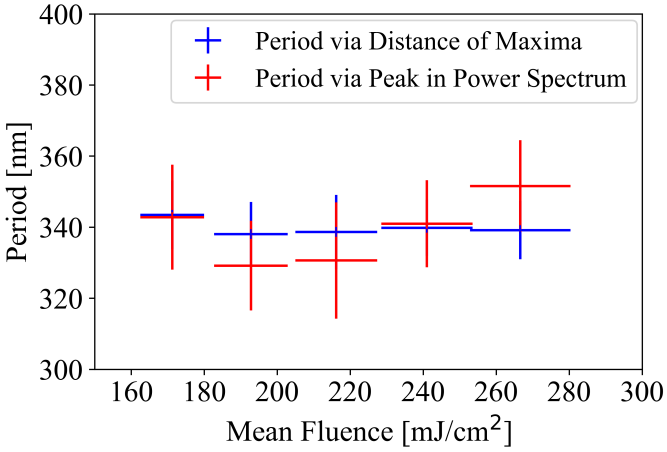

Figure 6.5.: The figure shows the periods of the structures measured at fluences ranging from 170 to 270 mJ/cm^2. The wavelength of the beam was 343 nm and the pulse duration 200 fs. The blue points show the periods measured taking the distance of the maxima, the red points using the maximum of the power spectrum. The data in this plot were published in [48].

data and equation 2.75, the expected periods for different electronic temperatures were calculated and compared to the measured data. The MD-TTM simulations that will be presented in the next section show a maximum electronic temperature of about 26500 K for a fluence of 270 mJ/cm^2. The result of the comparison is shown in Figure 6.7, showing, that the changes in period are within the measurement error.

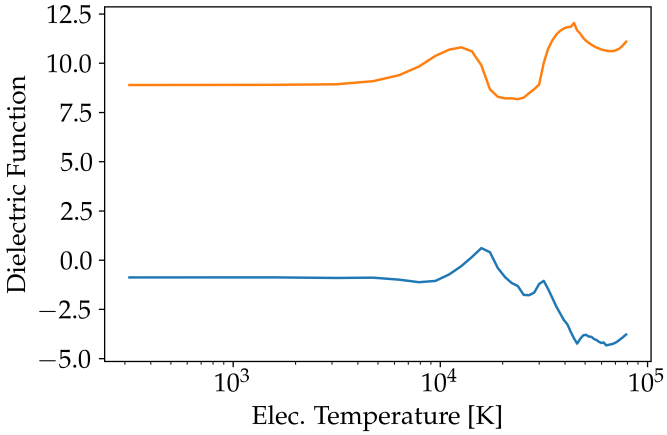

Figure 6.6.: The figure shows the change in the real part (ϵ_1) and the imaginary part (ϵ_2) of the dielectric function as a function the temperature of the electronic subsystem. The data were provided by Blumenstein et al. [136].

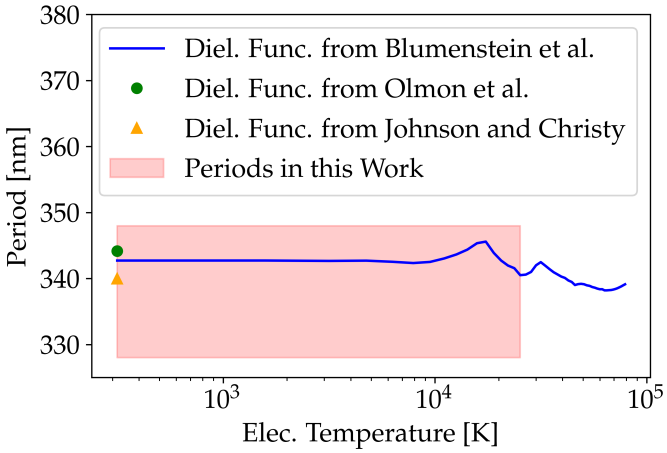

Figure 6.7.: The blue line in this figure shows the calculated periods for different electronic temperatures given the data from Blumenstein et al. [136]. The green dot and orange triangle show the calculated periods given the dielectric function published by Johnson and Christy [135] and Olmon et al. [72]. The red shaded are shows the results of this work showing the range of error. The shaded area goes up to 26500 K, corresponding to the maximum electronic temperature at 270 mJ/cm^2 in the MD-TTM simulations presented in Section 6.2. These data were published in [48].

6.2. Comparison between Experiment and Simulation

The small period of the structures allow a direct comparison of their appearance with simulation results. First, an overview is given of former studies aiming at an asimilar comparison by Ivanov et al. [95] and Blumenstein et al. [96].

6.2.1. Simulations

The simulations were done by Dr. Dmitry Ivanov from the Universität Kassel. The type of simulation was a MD-TTM simulation, as described in Section 3.2.
In the works of Ivanov et al. and Blumenstein et al. the results of MD-TTM simulations were compared to structures produced using the two-beam interference method with mask projection. The setup in their work is similar to the one shown in 4.1, using a krypton florid (KrF) excimer amplifier, that was seeded by titan sapphire (Ti:Sa) laser pulses. The wavelength was 248 nm and the pulse duration was 1.6 ps.
The study showed good agreement between the experiments and the simulations for a broad range of phenomena such as the structures forming due to voids underneath the sample in accordance with the period of the structures. This leads to the uprise of the surface and so to the creation of structures [95]. For higher fluences they show that the ablated walls are connecting to create upright standing structures [96]. The results were also presented in Section 2.5.1.

6.2.2. Source Function

The source function Q, introduced in Section 3.2.1 in equation 3.1 gives the energy input per volume and time and is the point where the SPP theory enters the simulation. The source function was mainly developed by Dr. Pavel Terekhin and a detailed description of the source function can be found in [70] and the supplementary material of [49].
The used source function for the simulation consists of three distinct parts and is written as

$$Q_{\text{total}}(\mathbf{r}, t, \beta, \delta) = Q_{\text{las-las}}(\mathbf{r}, t) + Q_{\text{las-SPP}}(\mathbf{r}, t, \beta, \delta) + Q_{\text{SPP-SPP}}(\mathbf{r}, t, \beta, \delta). \tag{6.2}$$

Each of the terms describes the energy input of a distinct source. The $Q_{\text{Las-Las}}$ describes the input of the laser beam. The $Q_{\text{SPP-SPP}}$ gives the part solely attributed to the SPP and $Q_{\text{Las-SPP}}$ describes the interference between the laser pulse and the SPP. Q_{SPP} and $Q_{\text{Las-SPP}}$ both depend on β and δ. Here δ is the phase difference between the optical wave of the laser pulse and the SPP, which the experiments are not sensitive to. The factor β is the coupling efficiency describing how much of the energy of the laser is transferred to the SPP wave. The phase and the coupling efficiency are free parameters in this calculation and the phase is not relevant for a comparison to the experimental results. Figure 6.8 shows the different parts and the total source function with a coupling parameter of $\beta = 0.3$ and $\beta = 0.8$. The individual components of the source function are given in the Appendix A.

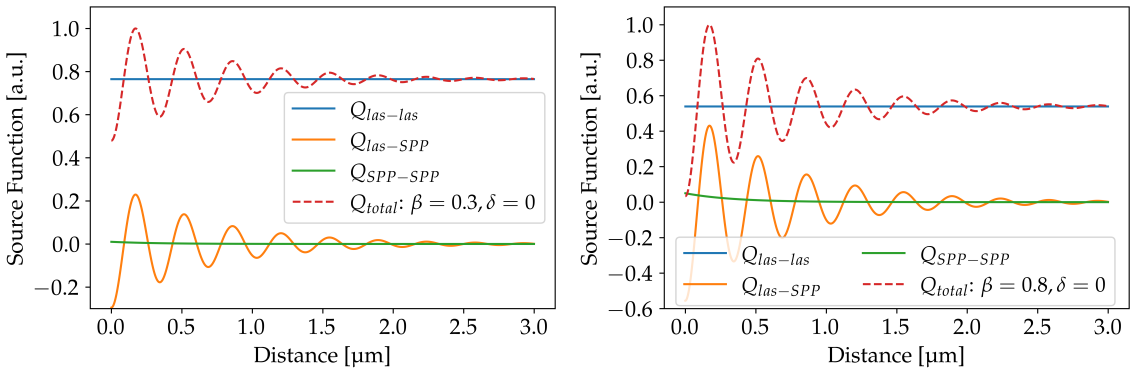

a) $\beta = 0.3$ b) $\beta = 0.8$

Figure 6.8.: The graphs show the source function as described in [70] for two coupling parameters a) $\beta = 0.3$ and b) $\beta = 0.8$. The functions are calculated for a laser wavelength of 343 nm and a pulse duration of 250 fs for a homogeneous beam profile on a gold surface. The material parameters for gold are taken from [72].
The green dashed line shows the total source function Q_{total}. The blue line shows $Q_{\text{las-las}}$, which contains the contribution of the laser beam. The orange line shows the contribution of the inference term between the SPP and laser $Q_{\text{las-SPP}}$. The last line in purple shows the contribution of solely the SPP in the term $Q_{SPP-SPP}$.

6.2.3. Results of the Simulations

The simulation of the process of LIPSS production was done at the Lichtenberg Super Computer Facility at the TU-Darmstadt. The size of the sample in the simulation was 4000 nm x 10 nm x 200 nm in x, y and z direction, respectively. The simulated sample consisted if $375{\cdot}10^6$ atoms.
As the source function presented in the previous chapter has two free parameters, these were set to $\beta = 0.3$ and $\delta = 238.68°$. The incident fluence used in calculating the source function was 130 mJ/cm^2. The parameters for gold were taken from [72] and the laser parameters were a wavelength of 343 nm and a pulse duration of 250 fs. Snapshots were taken at different times and the different physical quantities were evaluated.
First the pulse is absorbed by the electronic system, which reaches it's maximum temperature at about 1 ps after the start of the irradiation. The maximum electronic temperature reached $\approx$ 14500 K. The distribution of electronic temperature can be seen in the in Figure 6.9 (a). It is readily seen that the first peak is heated to a higher temperature than the second one, due to a higher energy input in this first region.
From the electronic system the energy is transferred to the lattice. The lattice temperature is maximized about 8 ps after the start of irradiation. Here also the first zone is more affected than the second one, with the maximum temperature of the lattice reaching about 3500 K. Due to the high temperatures of the lattice, high pressures develop under the surface at hotspots with a maximum pressure of 15 GPa. A snapshot of the pressure distribution after 8 ps can be seen in Figure 6.10.

The change in the surface morphology starts at about 20 ps. At that time the first few nanometres of the simulated surface are liquid. The depth of the liquid phase is dependent on the deposited input energy. At 120 ps, small voids form under the surface at a depth of about 50 nm. These voids push the surface upwards and in regions, with a larger energy input more voids are forming. These voids grow in size and may unify to form even bigger voids. These bigger void push the surface even higher. After 1000 ps the, the liquid surface starts to solidify again and gets frozen with the voids still under the surface. In Figure 6.11 the shape of the surface can be seen at the times, 20, 120, 300, 500 and 1000 ps. The black dashed line in the last snapshot in Figure 6.11 shows the position of the surface before irradiation. In the simulations a general uplift of the complete surface by 2-3 nm became visible. This

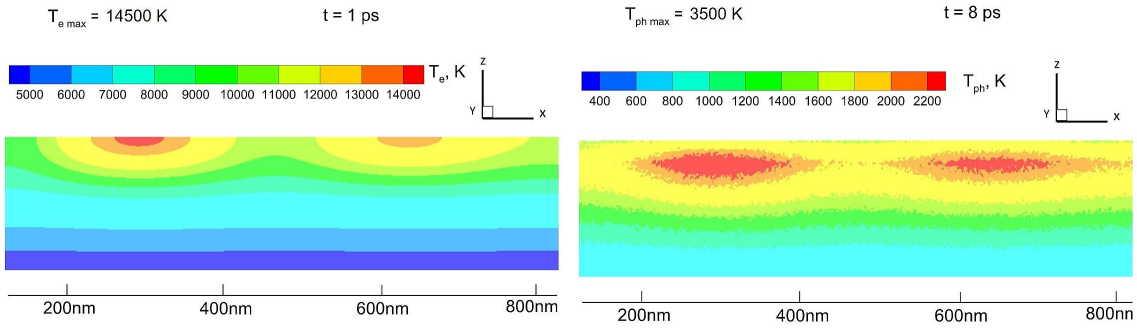

a) Electronic System Temperature b) Lattice Temperature

Figure 6.9.: The figure shows the temperature distribution for a) the electronic system in a snapshot at 1 ps and of b) the lattice in a snapshot at 8 ps after irradiation. This Figure was produced by D. Ivanov and has been published in the supplementary material of [49].

may be due to thermal expansion of the lattice. As visible in the graph of the source function in Figure 6.8, the total source term does not sink to zero. This effect is too small to be measured by the AFM.

Inside the sample, dislocations appear at times later than 300 ps, visible in the last two snapshots in Figure 6.11. This is most probable not an artifact in the simulation and has also been seen in experiments concerning laser peening [137].

The height of the structures formed in the simulations can be compared to the structures measured after the experiments. The simulations match in the height of the structures for 192 mJ/cm^2. For the experimental structures, the measurements were evaluated beginning with the third maximum of the ripple structure due the heavy debris on the first two periods. In the simulations the height of the third maximum is ≈25 nm just like in the AFM measurement of the experimental structures in Figure 6.3. Looking at the decay of the structures and assuming an exponential decay of the structures, the decay length for the simulation is 1.51 µm^{-1}. For the experimental data, the decay length is 1.25 µm^{-1}. Here a fit for the first five shown maxima was taken. So the measured and calculated decay lengths differ by about 20%.

As stated earlier, for experiments with a fluence of 130 mJ/cm^2 no structures could be observed and the height of the structures in the simulation matches the height using 192 mJ/cm^2 in the experiment. This indicates a mismatch between the used fluences in the experiments and the simulations.

One possible explanation for the mismatch concerns the coupling parameter β. The

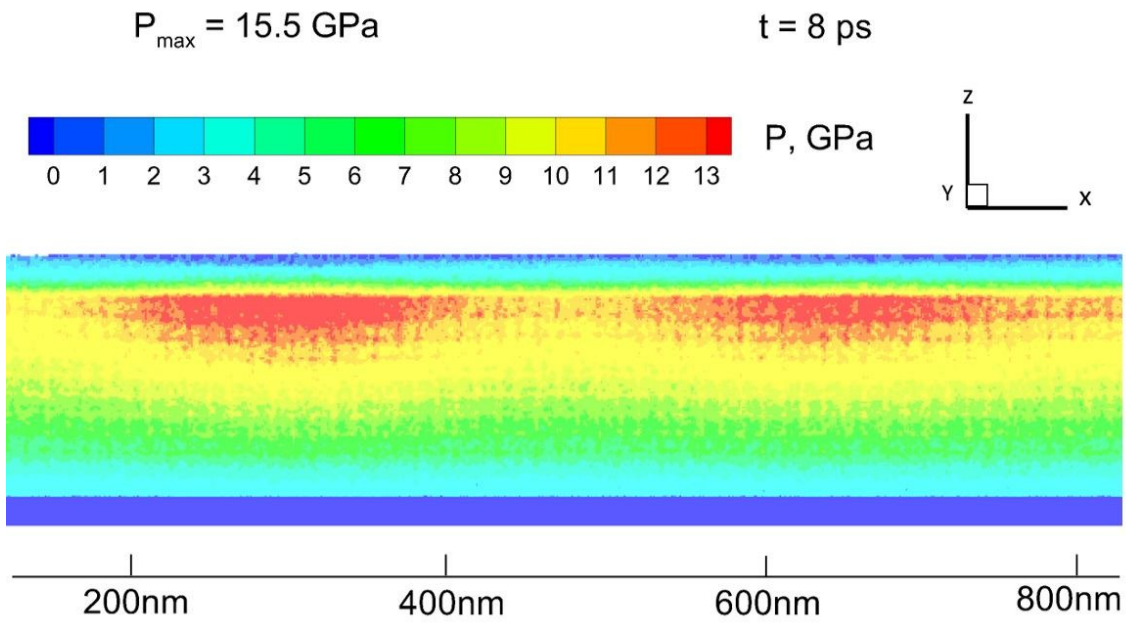

Figure 6.10.: The figure shows the pressure distribution in the simulation. The snapshot is taken at about 8 ps. This Figure was produced by D. Ivanov and has been published in the supplementary material of [49].

value of 0.3 was determined by preliminary trials but to determine the correct value comparison to the experiments is needed. The coupling parameter might as well be fluence dependent.

Another possible reason for the lower ablation threshold in the simulation may be due to a change in reflectivity as a function of the electronic temperature in the sample, which was not included in the simulation. Taking a look at the results from Blumenstein et al. measuring the reflectivity as a function of the electronic temperature [136], for a wavelength of 343 nm and an electronic temperature of 14500 K a reflectivity of 0.48 was obtained, instead of 0.36 as given by [72] at room temperature. Of course, not the entire pulse experiences the electronic system at this temperature; in fact there is a complex coupled system between reflectivity and electronic temperature. The progression of the reflectivity dependent on the electronic temperature from the data from [136] can be seen in Figure 6.12. Measuring the reflectivity in the experiment at 200 mJ/cm^2 leads to a reflectivity of 0.41, with the sample tilted by an angle of about 3°, to separate the in- and outgoing beam. Figure 6.12 does not show a clear trend of higher reflectivity for all electronic temperatures above room temperature, but since the maximum is at an electronic temperature of about 10000 K, it is expected that for high pulse energies the mean reflectivity is

higher than assumed in the simulations.
The last possible reason for the discrepancy in fluences between simulation and experiment is the small simulation size in y-direction. The size in this direction is only 10 nm compared to the sizes of 4000 and 200 nm in x and z direction, respectively. The small size was chosen to accelerate the computational time of the simulation, but the small size may lead to an artificial growth of small void bubbles under the surface. As explained earlier, the voids are mainly responsible for the uplift of the surface due to expansion and unification of small voids. A small volume may prevent small voids to collapse and so artificially increase the number of voids present which drive a more extreme response of the sample to the laser pulse.

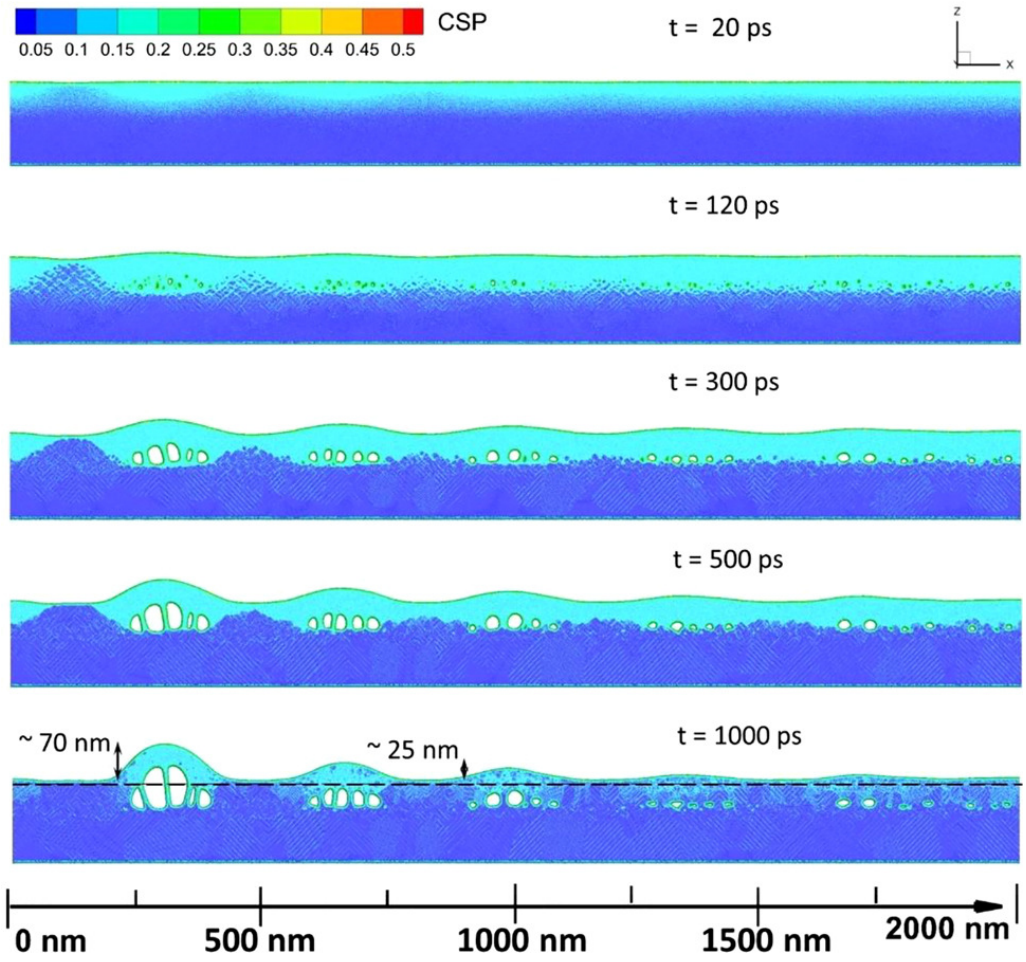

Figure 6.11.: The figure shows the distribution of atoms in the simulation in snapshots at different time steps. The atoms are color coded by the CSP described in 3.2.2. The color of a region indicates the state of aggregation of the region, with crystal $<0.08 <$ defects (dislocations) $< 0.11 <$ liquid $< 0.25 <$ surfaces $< 0.50 <$ vapor (free atoms). This Figure was produced by D. Ivanov and has been published in [49].

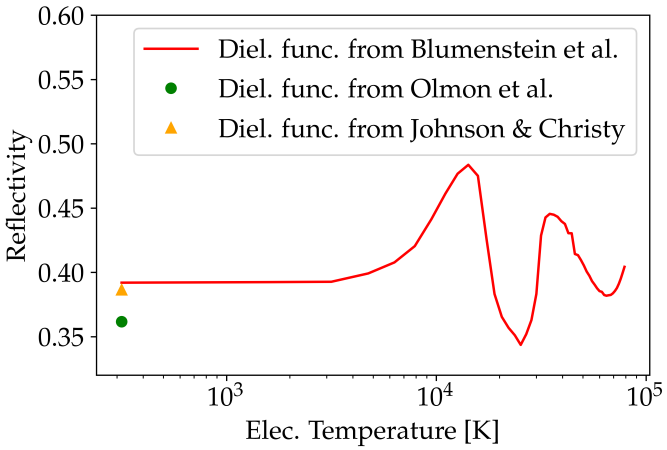

Figure 6.12.: The figure shows the reflectivity of a gold surface as a function of the electronic temperature at 343 nm. The graph shows as red line the reflectivity given by the data from Blumenstein et al. [136]. Also shown are the reflectivity values given by Johnson and Christy [135] as yellow triangle of Olmon et al. [72] as green circle.

6.3. Creating LIPSS using other Wavelengths

Additionally to UV, also the other available wavelengths of the Pharos were used for the creation of LIPSS in single pulse experiments. For these experiments no simulations have been performed for comparison.

6.3.1. Single Pulse LIPSS using Green Light

For the wavelength 515 nm (green), the irradiation took place on both the step edge and the FIB groove. The pulse duration was about 200 fs. The step edge was again created by a razor blade, as explained in the beginning of this chapter.
Due to the higher reflectivity of gold at 515 nm a higher fluence was needed for the creation of LIPSS, the threshold being at about 250 mJ/cm^2. The reflectivities from Johnson and Chrity [135] for 343 nm and 515 nm are 0.39 and 0.59, respectively. Taking this into account, the absorbed fluence in both cases is about 105 mJ/cm^2. The reflectivity values do not take into account the change in reflectivity due to a heating of the electronic system.
Some results of the irradiation event can be seen in Figure 6.13. The measured

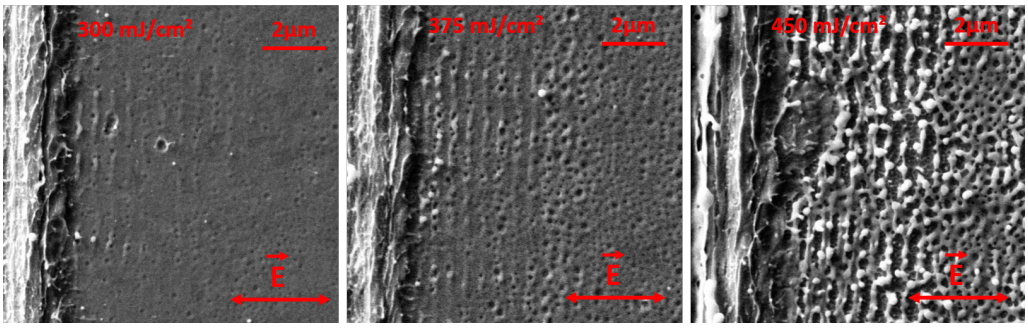

Figure 6.13.: The figure shows strucutres forming after irradiating the razor-blade step edge using the 515 nm beam with a pulse duration of about 200 fs. The fluences were varied between 300 and 450 mJ/cm^2.

periods depending on the fluence are visible in the left part of Figure 6.14, while the mean period for all experiments was 499±16 nm. The periods calculated from the dielectric function from Johnson and Christy [135] and Olmon et al. [72] are 473 nm and 466 nm, respectively, leading to a deviation form the obtained period by about 6% and 7%. In Figure 6.14 (b) the calculated period from the data of Blumenstein et al. [136] for different electronic temperatures is shown, which match the measured periods very good.

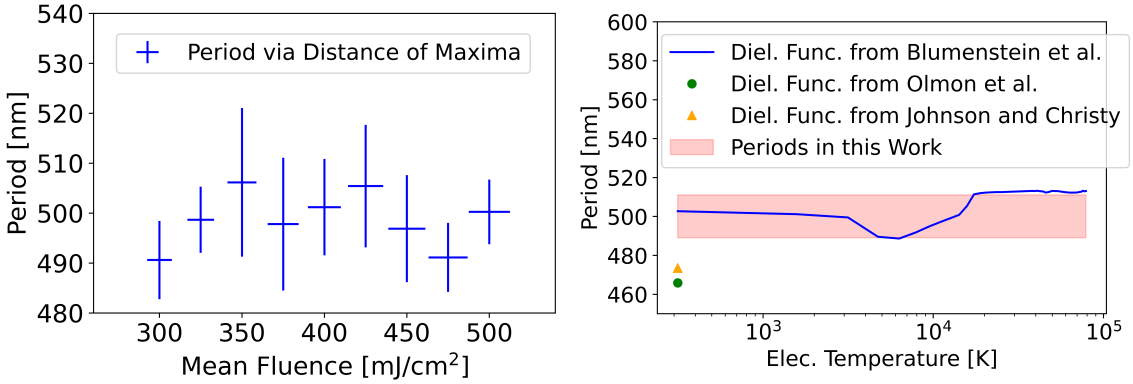

a) b)

Figure 6.14.: The figure shows (a) the measured period of LIPSS obtained at 515 nm depending on the mean incident fluence of the beam and (b) a comparison of the calculated period given the dielectric function form Blumenstein et al. [136] (blue line) against the electronic temperature. Also included are the values from Johnson and Christy [135] (yellow triangle) and Olmon et al. [72] (green circle). Also included is the mean period measured in this work (red shaded area). Since for this wavelength there are no simulations, it could not be concluded what electronic temperatures were reached during the experiments.

When irradiating a FIB groove using a fluence of 400 mJ/cm^2, due to the inhomogeneities in the beam profile, it is possible to see how the structures evolve depending on the fluence, which shows similarities between LIPSS and the results obtained by two-beam interference also presented in Section 6.2. The results are shown in Figure 6.15. The structures show large similarities with the ones shown in Figure 2.10. The structures in the red area look like surface swelling with void openings and the structures in the green area like surface wall formation. In the literature on LIPSS, the two types of structures are sometimes differentiated as non-ablative and ablative LIPSS [94].

6.3.2. Single Pulse LIPSS using Infrared Light

As well as for the other two other wavelengths, also the fundamental wavelength of 1030 nm was applied. Here again the structures are produced using both the razor blade step edge and the FIB groove.
The comparison of the absorbed fluence for IR is not as useful as before, because the literature value for the reflectivity at 1030 nm as given by Johnson and Christy

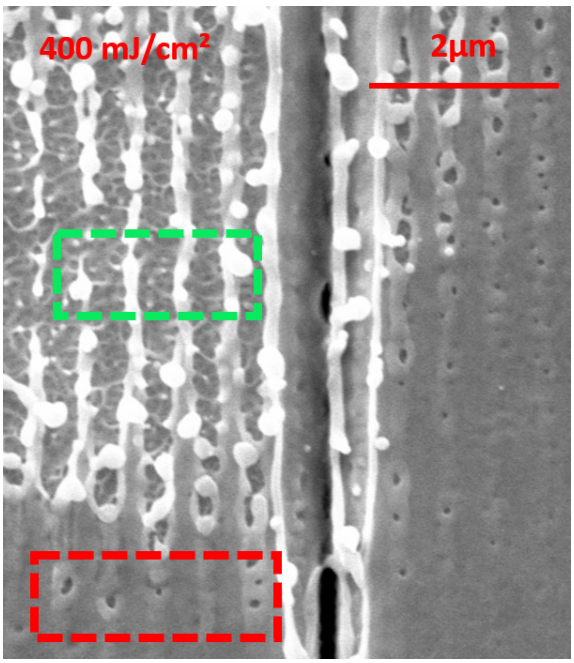

Figure 6.15.: The figure shows the structures developing after irradiating a FIB groove with a beam at 515 nm and a pulse duration of 200 fs at a fluence of 400 mJ/cm^2.

[135] is about 0.98 and therefore for an absorbed fluence of 100 mJ/cm^2 an incident fluence of 5000 mJ/cm^2 would be needed, but the experiments show results already at much smaller fluences. This may indicate that the absorption may strongly be influenced by non-linear effects.
In the IR the used fluences ranged from 500-1000 mJ/cm^2 and structures are visible already at 600 mJ/cm^2. Figure 6.16 shows the structures forming at different fluences.
The period of the structures are measured for the different fluences and like for UV there is no large variation in the period depending on the fluence. In this case the period was determined solely by measuring the distance between the maxima of the structures. The results can be found in Figure 6.17.

The mean value of the measured period is 1023±19 nm, with the prediction from theory being 1019 nm, for both Johnson and Christy [135] as well Olmon et al. [72]. As the spatial decay of the structures reduces with increasing wavelength, they develop over a longer range away from the step edges. Therefore another experiment was done to see how far the structures reach.

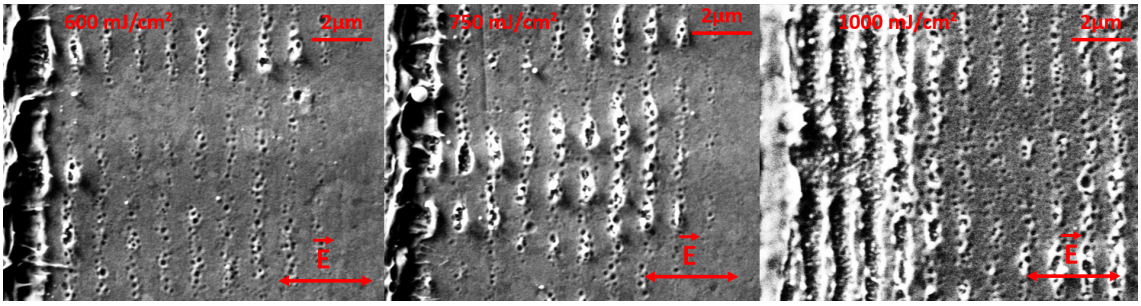

Figure 6.16.: The figure shows SEM pictures of the LIPSS forming at the step edge, after irradiation with 1030 nm beam with a pulse duration of 250 fs at fluences from 600 to 1000 mJ/cm^2.

For the experiment one of the FIB grooves was used. The results can be seen in Figure 6.18. The longest distance at which structures could be seen was about 25 µm away from the groove.

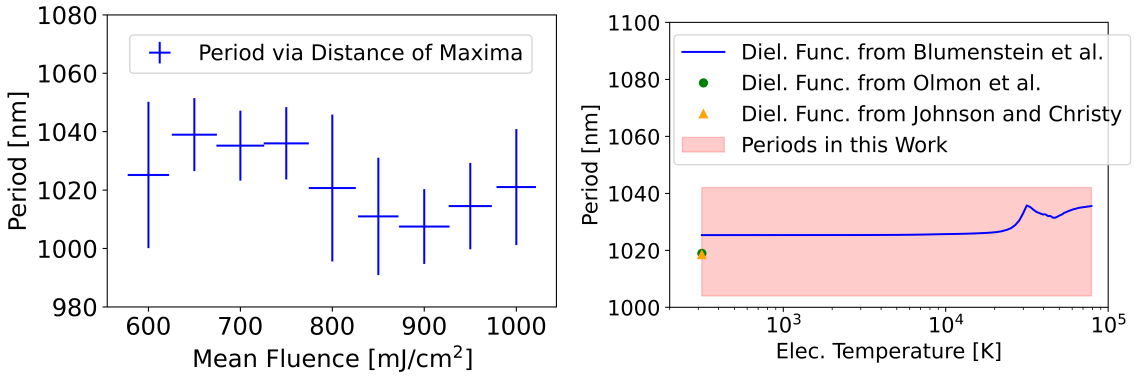

a) b)

Figure 6.17.: The figure shows (a) the periods of the structures created at different fluences for experiments at 1030 nm with a pulse duration of 280 fs and (b) the calculated periods for different electronic temperatures. The values for Johnson and Christy [135] (yellow triangle) and Olmon et al. [72] (green circle) for room temperature are also included. The electronic temperature dependent values are from Blumenstein et al. [136] (blue line). Since for this wavelength there are no simulations, it could not be concluded what electronic temperatures were reached during the experiments. The periods of this work are displayed as red shaded region.

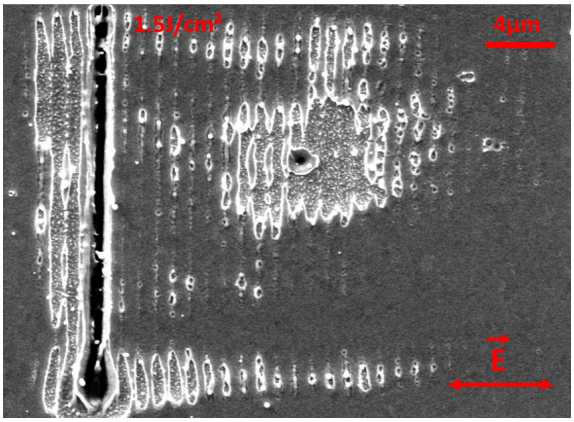

Figure 6.18.: The figure shows a SEM picture of the structures forming at the FIB groove after irradiation at 1030 nm with a fluence of about 1.4 J/cm^2. The structures reach to about 25 µm from the FIB groove.

6.4. Beam Profile Shaping

As visible in the previous results, the structures show an exponential decay with increasing distance from the step edge, which is also predicted by the SPP theory. As the energy input is given by the interference between the SPP and the still prevailing laser beam, one may compensate for the exponential decay by changing the beam profile.

To change the beam profile, the Top-hat converter was used, which allows for changing the beam profile by controlled misalignment. If the converter is slightly moved laterally, the profile shown in Figure 6.19 is obtained. Using that beam profile, the

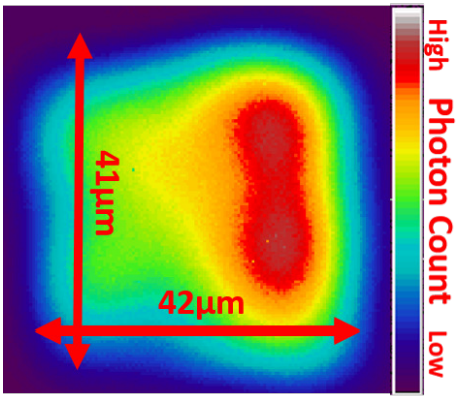

Figure 6.19.: The figure shows the fluence profile of the 343 nm beam after laterally moving the beam shaper.

step edge created by the razor blade has been irradiated using different beam energies. For easy comparison to the previous results, also the mean fluence will be given, although it is not a good measure for the inhomogeneous beam profile. The results are shown in Figure 6.20.

In the figure, the fluence increases with increasing distance from the step edge. The influence of the shape of the beam profile on the height profile of the structure was investigated by AFM measurements. The results are shown in Figure 6.21. As visible in the figure the variation in the height distribution is most pronounced at the first few periods, where the exponential decay is most noticeable.

This is most likely due to the increase of fluences causing additional uplift, while the SPP wave does decay in amplitude. At a larger distance away form the step edge, the fluece causes to much damage to the surface and potential LIPSS vanish in the roughness of the surface.

The results show that it is possible to adjust the beam profile in a way to cancel out

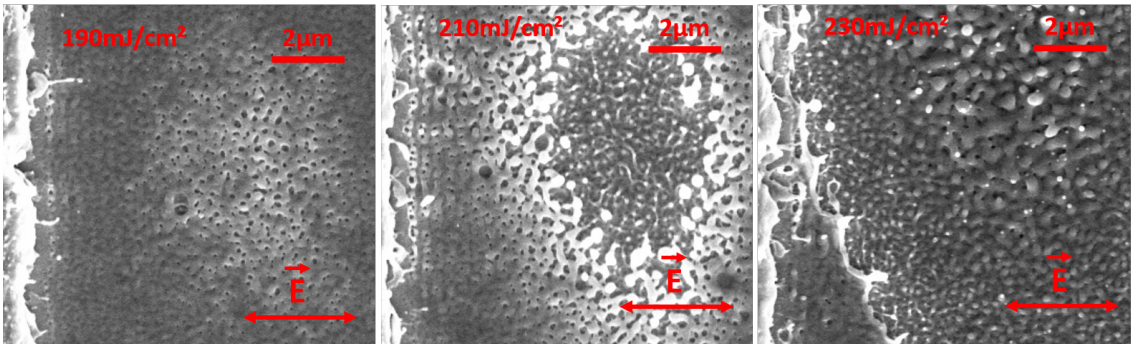

Figure 6.20.: The figure shows the structures forming at different fluences, when irradiated with the 343 nm beam using the beam profile shown in Figure 6.19. Within each SEM picture the fluence is increasing with increasing distance from the edge.

the effect of the exponential decay in a single pulse irradiation event.

There are works concerning the homogeneity of structures obtained using longer wavelengths (800 and 1030 nm) by controlling the overlap of multiple spots [138]. For short wavelength a hybrid approach of controlled overlap and the here presented way of manipulating the structures by the beam profile may be needed to achieve comparable results.

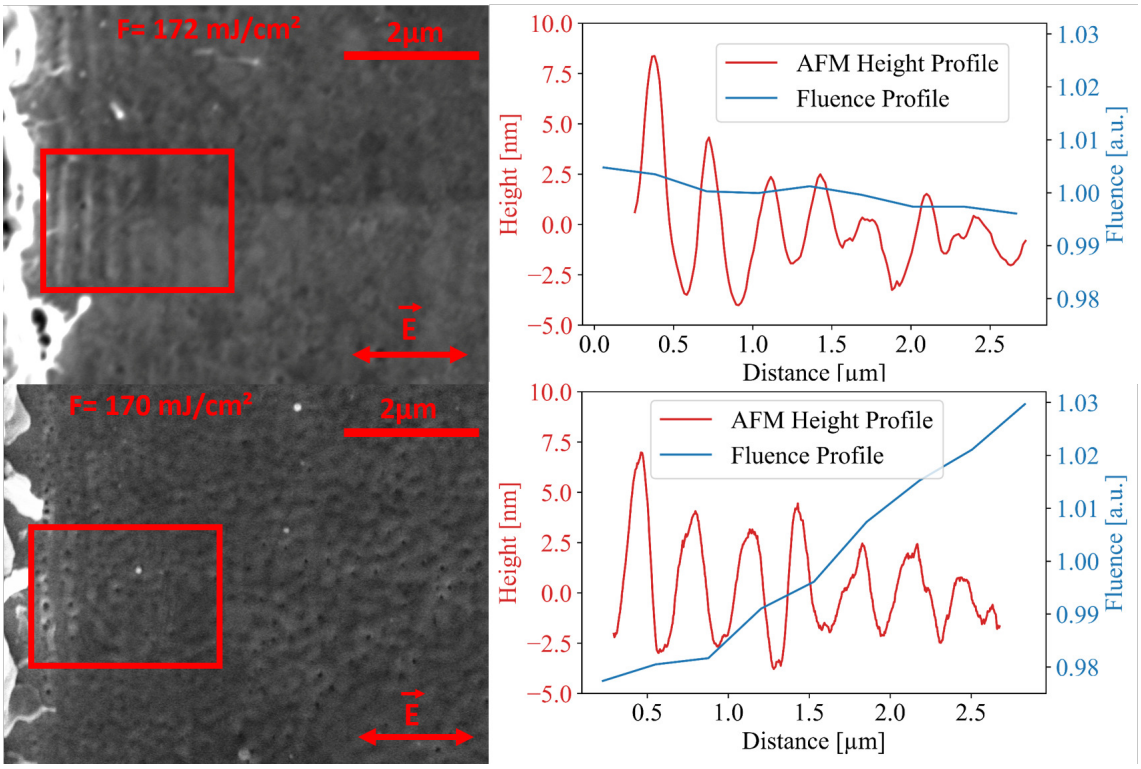

Figure 6.21.: The figure shows a comparison of the results of irradiation events at a mean fluence of about 170 mJ/cm^2 with a homogeneous profile (top) and a profile with a rising slope (bottom) of the 343 nm beam. The plots on the right show the AFM height profiles (red) and the fluence profile (blue). On the left SEM pictures of the structures are shown, where the red square indicates the region in which the height profile was taken. For the AFM measurement, the 0 position was placed at the mean of the height profile. The red arrow in the SEM picture show the polarisation of the beam. The data in this figure were published in [48].

6.5. Confinement

The period as well as the decay length of the LIPSS structures are in the SPP theory dependent on the dielectric material covering the sample. Up to now, the LIPSS were obtained with the dielectric layer being air.
In addition to the experiments for LIPSS in air, also experiments using liquid confinement layers on gold were done. Figure 6.22 shows the theoretically expected periods for varying wavelength under different confinement layers and the calculated decay constant. The values are calculated using the equations 2.75 and 2.77. Corresponding experiments were done using the FIB grooves.

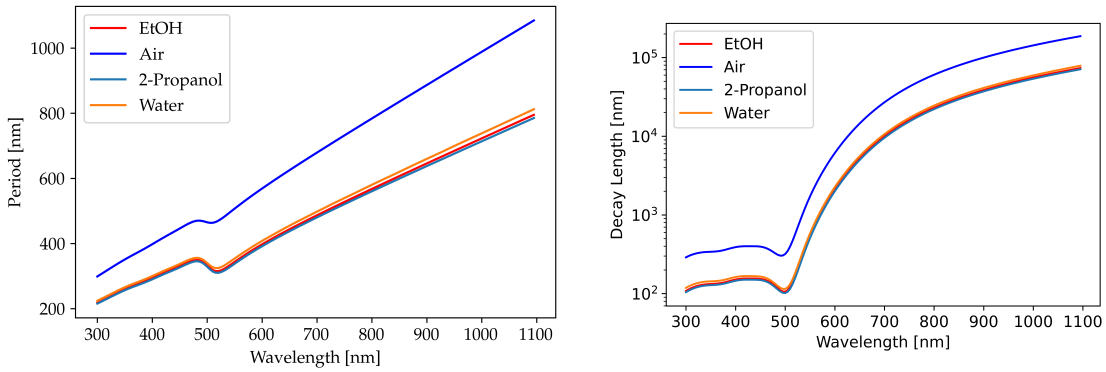

a) Periods

b) Decay length

Figure 6.22.: The graph shows the a) calculated period of the LIPSS according to equation 2.75 and b) the decay length of SPP calculated by equation 2.77 on a gold surface with different liquid layers. The dielectric function for Gold, Water, Ethanol and 2-Propanol are taken from [72], [110], [71] and [71], respectively.

The experiments were done using the three available wavelength of the Pharos. From Figure 6.22 it can be seen, that the decay length reduces by a larger factor than the period. This may lead to fewer periods forming on the surface. Calculating the corresponding factors shows that the reduction of the decay length is about a factor of two higher than that of the period. Specifically, the factors are 1.90, 2.30 and 1.87 for 343, 515 and 1030 nm, respectively for an ethanol layer.
Additionally, it has been shown in Section 5.1 that a liquid layer during the structuring leads a lower structure height.
The results of the experiments using the Pharos at 343 nm are presented in Figure 6.23. For the shortest wavelength of 343 nm, it is hard to tell whether LIPSS have emerged, but the SEM pictures as well the height measurement from the AFM mea-

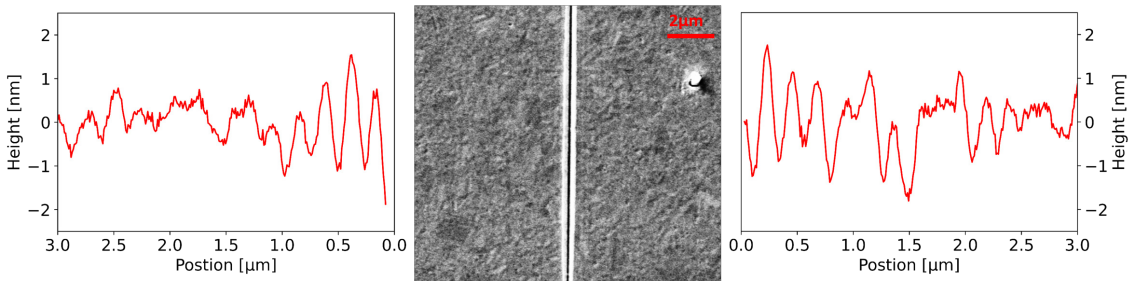

343 nm 275 mJ/cm^2

Figure 6.23.: The picture in the middle shows the SEM picture of the FIB groove after irradiating it at 343 nm with 250 mJ/cm^2 under an ethanol confinement layer. Left and right of the SEM picture AFM height measurements of the respective side of the FIB groove are presented. In the AFM measurement, the 0 position was placed at the mean height of the profile. The maximum oscillation amplitude was about 3 nm.

surement show slightly visible structures. The period of the measured structures is about 230 nm, which differs by approximately 10% from the calculated value of 256 nm. The dielectric function for gold was taken from [136] at a electronic temperature of 315 K and for ethanol from [71]. Though, in this case an uncertainty comes not only from the varying dielectric function of the gold, but also from that of the ethanol layer. The height of the structures is, as was predicted, very small with less than 3 nm height modulation between maximum and minimum. Also, there are only 3-4 visible peaks, as compared to about 10 without the layer, as shown before. At 515 nm, the structures are clearly visible. The fluences for which structures are visible were in the range of 250-350 mJ/cm^2. The evaluation of the height profile indicates more periods than what was visible in the SEM picture. Measuring the period by taking the distance between the maxima of the structures gives about 340 nm, independent of whether measuring all the peaks in the height profile or only the structures only visible in the SEM picture. The calculated period is 368 nm, with the dielectric function for gold taken from [136] (at 315 K) and for ethanol from [71]. In this case, the measured period is about 7% smaller than calculated one, similar to the case at 343 nm. The reason for this may be that a constant dielectric function for both gold and ethanol was assumed. For this wavelength, the structures have a slightly higher amplitude with about 9 nm.

Also the longest wavelength of 1030 nm was applied to produce LIPSS under the ethanol layer. Though as it is visible in Figure 6.25 a), for a fluence of 900 mJ/cm^2 no structures are visible under the layer, in the SEM picture, there is some peri-

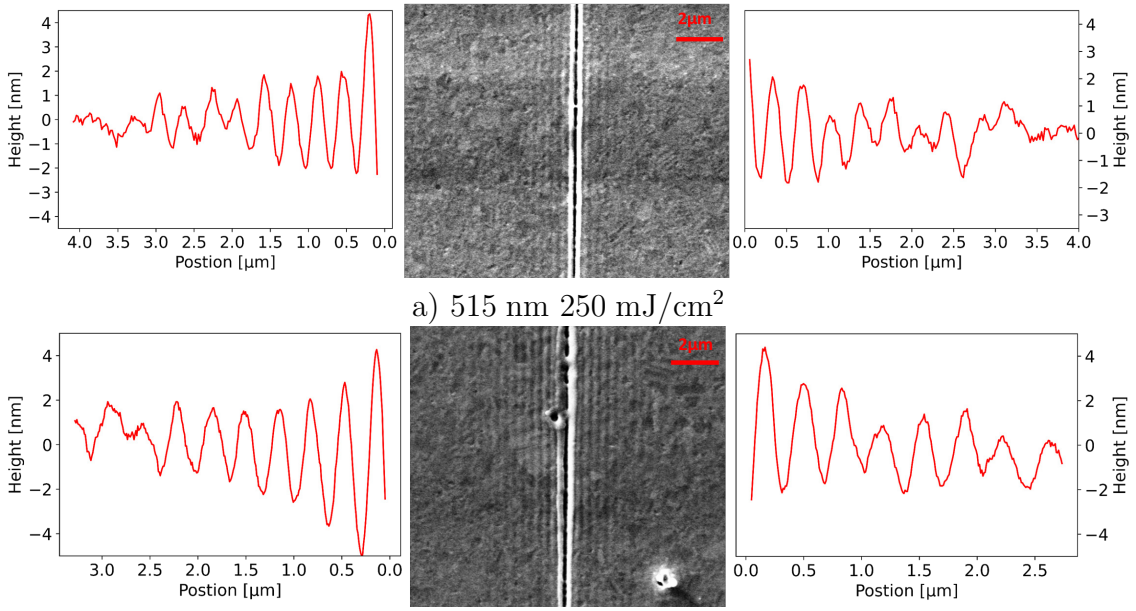

Figure 6.24.: The figure shows the results of irradiating the FIB grooves at 515 nm with a fluence of a) 250 mJ/cm^2 and b) 300 mJ/cm^2 under an ethanol confinement layer. In the middle there is a SEM picture of the groove with the structures and on both sides the respective AFM height measurements.

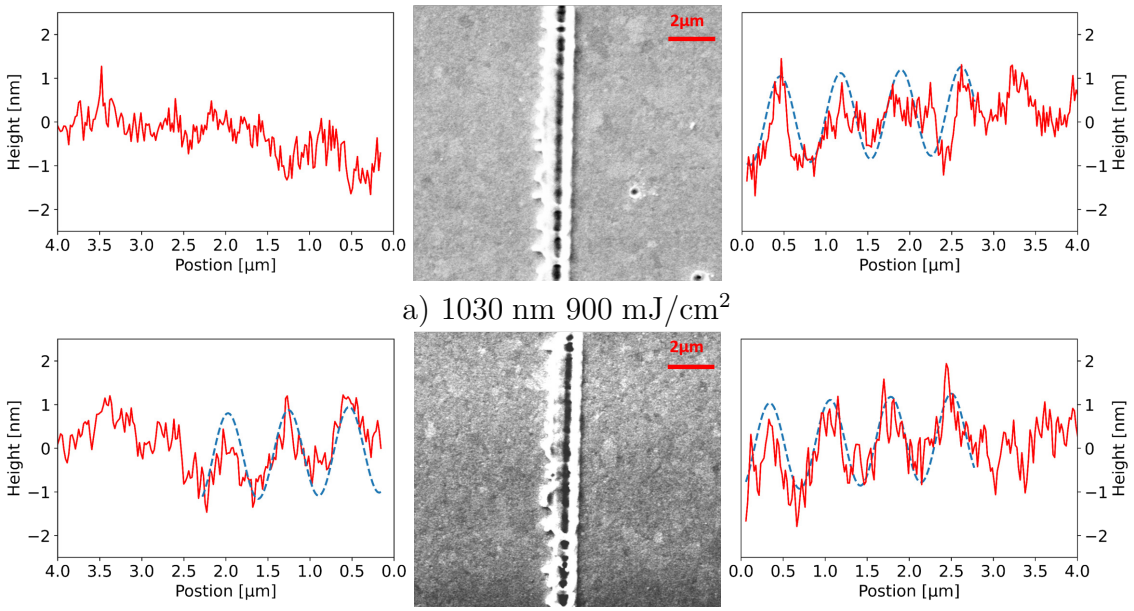

a) 1030 nm 900 mJ/cm^2

b) 1030 nm 1300 mJ/cm^2

Figure 6.25.: The figure shows the results of irradiating the FIB grooves using 1030 nm with a fluence of a) 900 mJ/cm^2 and b) about 1400 mJ/cm^2 under an ethanol confinement layer. In the middle there is the SEM picture of the groove with the AFM measurements on both sides. The blue dashed line represents a periodic function with a period of 720 nm, just to guide the eye.

odicity visible in the AFM measurement on the right side. The period determined by the power spectrum of the measurement was about 720 nm. To test, whether a higher fluence would lead to structures which are better visible, another test with 1.4 J/cm^2 was performed. It is shown in Figure 6.25 b). The structures are again hardly visible in the SEM picture, but now in the AFM measurements on both sides structures with a period of about 720 nm are visible. The amplitude of the structures is only a few nanometres, that may be increased with a higher fluence, but no higher fluence was available in the experiments. The expected period of the structures would be 754 nm for the dielectric function of gold from [136] (at 315 K) and for ethanol form [71]. The measured period differs from this value by about 5%. So it is possible to create structures with periods smaller than the wavelength by LIPSS production under a liquid confinement layer, though the amplitude of the structures is low. The periods of the structures can be predicted using the plasmonic theory and the dielectric function from Blumenstein et at. [136] for all wavelengths.

7. Conclusion

The thesis reports on investigations of laser generation of periodic structures on gold surfaces and discusses different ways to explain and may predict their properties. The structures were generated using two different methods: two-beam interference and spontaneous formation via LIPSS.

Single pulse two-beam interference structures on gold are compared for femtosecond and picosecond pulses and with and without transparent confinement material on the surface. A confinement layer leads to droplet free and smoother, but shallower structures compared to the case without confinement. The structures were formed only by surface swelling with confinement, and features like wall formation of colliding side walls were not observed.
Using a 200 fs pulse and a liquid confinement layer, the structures were shallower in the center of the irradiated region and increased in height towards the borders. This effect was more pronounced for thinner layers, up to the point where no structures were left in the center. This effect may be explained by a pressure bubble in the layer pushing the molten material in the center down- and sidewards. This behaviour was not observed for the longer pulse (8 ps) and also not using a solid confinement layer, where shallow but homogeneous structures were obtained.

In this work, the creation of LIPSS using three different laser wavelengths, via single pulse experiments with and without confinement layer was also investigated. To induce SPP in a single pulse experiment, an initial defect on the surface is required. For this, line like step edges in the form of either scratches or FIB grooves were used.
The properties of the structures were compared to the predictions of the plasmonic theory. The periods of the LIPSS were in full accordance with those predicted by the plasmonic theory for all three wavelength (343, 515 and 1030 nm), using the material data from Blumenstein et al. [136]. Based on previously reported literature

data, there was good agreement in the UV and in the IR, but a 7% deviation was obtained at 515 nm. In addition, the region in which the structures are visible does increase with increasing wavelength, also in accordance with the SPP theory. The structures obtained at 343 nm were compared to simulations provided by Dr. Dmitry Ivanov. Although the periods of the simulated structures are matching the experimental ones, there was a mismatch in the fluence that was necessary for creating the structures. This mismatch may be attributed to a too small simulation volume, neglecting the change in reflectivity during the irradiation or a not optimal choice of the coupling parameter between light and SPP.

The possibility of influencing the appearance of the structures by either changing the beam profile or applying a liquid confinement layer was also tested. The experiments for LIPSS with a liquid confinement layer showed that it is possible to reduce the period of the structures, but at the expense of the range over which structures are visible as well as a lower structure height.

Moreover, applying a tailored beam distribution allowed to create LIPSS at a step edge with increased uniformity.

A. Appendix

Thickness Measurements

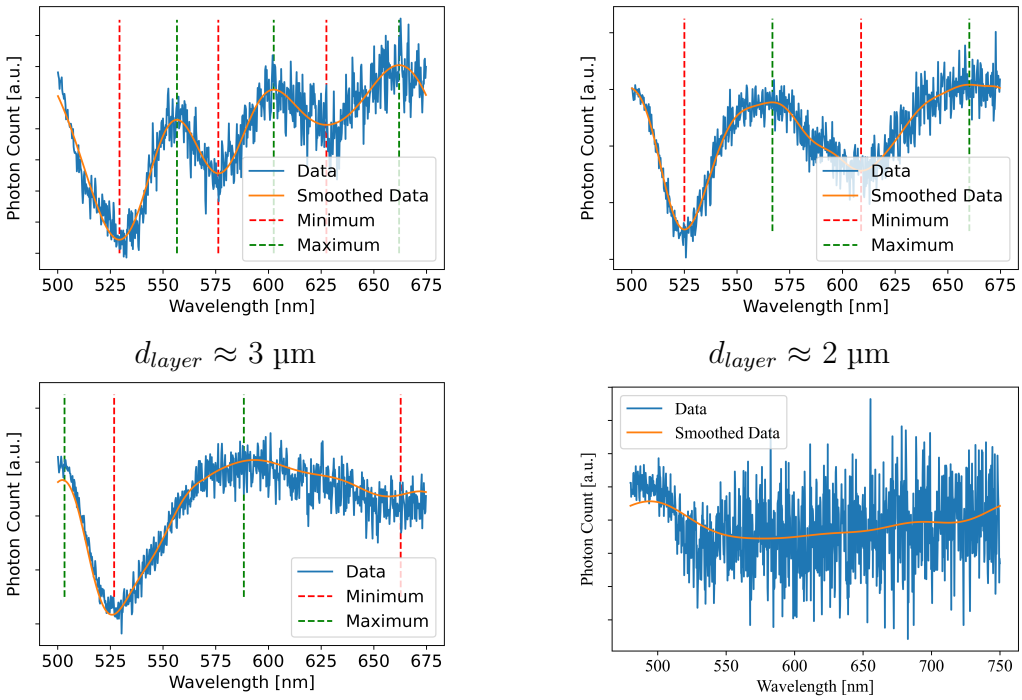

$d_{layer} \approx 3$ µm

$d_{layer} \approx 2$ µm

$d_{layer} \approx 1$ µm

Too thin to measure

Figure A.1.: Spectra of the thickness measurements during the irradiation event leading to the structures presented in 5.4. The blue line shows the measured spectral data, the original data is than smoothed using a Fourier and Savitzky-Golay filter. The smoothed data is shows as the orange line. In the smoothed data the maxima and minima are determined and from there the layer thickness is measured using the equations 2.83 and 2.84. The results of the calculations lead to thicknesses for about 3, 2 and 1 µm. The layer in the last pictures could not be measured.

Source Function

This chapter contains the equations used for calculation of the source function. The equations were mainly developed by Dr. Pavel Terekhin and are described in detail in [70].

$$Q_{\text{total}}(\mathbf{r},t,\beta,\delta) = Q_{\text{las-las}}(\mathbf{r},t) + Q_{\text{las-SPP}}(\mathbf{r},t,\beta,\delta) + Q_{\text{SPP-SPP}}(\mathbf{r},t,\beta,\delta) \tag{A.1}$$

$$Q_{\text{Las-Las}}(\mathbf{r},t) = F_{\text{inc}}\frac{8k_0 n_m k_m}{(n_m+1)^2+k_m^2}\exp(2k_0k_m z)\Phi_1\frac{1}{\tau}\sqrt{\frac{\sigma}{\pi}}\exp\left(-\sigma\frac{(t-t_0)^2}{\tau^2}\right) \tag{A.2}$$

$$\begin{aligned} Q_{\text{Las-SPP}}(\mathbf{r},t,\beta,\delta) =& \beta F_{\text{inc}}\frac{2(f_1\cos(f_3(x,z,\delta)) + f_2\sin(f_3(x,z,\delta)))}{(n_m+1)^2+k_m^2} \\ & \Phi_1 G_1(x,t)\exp\left((k_0k_m + k'_{z,m}) - k''_x x\right) \end{aligned} \tag{A.3}$$

$$Q_{SPP-SPP}(\mathbf{r},t) = \beta^2 F_{inc} f_9 \Phi_2(y) G_2(x,t)\exp\left(2(k'_{z,m}z - k''_x x)\right) \tag{A.4}$$

$$\Phi_1(x,y) = \Theta\left(-x+\frac{d_{beam}}{2}\right)\Theta\left(x+\frac{d_{beam}}{2}\right)\Theta\left(-y+\frac{d_{beam}}{2}\right)\Theta\left(y+\frac{d_{beam}}{2}\right) \tag{A.5}$$

$$G_1(x,t) = \frac{1}{\tau}\sqrt{\frac{\sigma}{\pi}}\exp\left(-\sigma\frac{(t-t_0)^2}{2\tau^2}\right)\exp\left(-\sigma\frac{(x-v_{g,SPP}(t-t_0)^2)}{2v_{g,SPP}^2\tau^2}\right) \tag{A.6}$$

$$f_1 = \frac{-k''_x f_4 + k'_x f_5}{k_0|\epsilon_m|^2} - (k'_{z,m}+k_0k_m)f_6 - (k''_{z,m}+k_0n_m)f_7 \tag{A.7}$$

$$f_2 = \frac{k''_x f_5 + k'_x f_4}{k_0|\epsilon_m|^2} - (k'_{z,m}+k_0k_m)f_7 + (k''_{z,m}+k_0n_m)f_6 \tag{A.8}$$

$$f_3(x,y,\delta) = k'_x x + (k''_{z,m}+k_0n_m)z + \delta \tag{A.9}$$

$$f_4 = \epsilon'_m(k'_x(n_m+n_m^2+k_m^2)+k''_x k_m) + \epsilon''_m(-k'_x k_m + k''_x(n_m+n_m^2+k_m^2)) \tag{A.10}$$

$$f_5 = \epsilon'_m(k'_x k_m + k''_x(n_m+n_m^2+k_m^2)) + \epsilon''_m(k'_x(n_m+n_m^2+k_m^2)+k''_x k_m) \tag{A.11}$$

$$\begin{aligned} f_6 = 1 + n_m &+ \frac{\epsilon'_m(k'_{z,m}k_m - k''_{z,m}(n_m+n_m^2+k_m^2))}{k_0|\epsilon_m|^2} \\ &+ \frac{\epsilon''_m(k'_{z,m}(n_m+n_m^2+k_m^2)+k''_{z,m}k_m)}{k_0|\epsilon_m|^2} \end{aligned} \tag{A.12}$$

$$f_7 = -k_m - \frac{\epsilon'_m(k'_{z,m}(n_m + n_m^2 + k_m^2) + k''_{z,m}k_m)}{k_0|\epsilon_m|^2} + \frac{\epsilon''_m(k'_{z,m}k_m - k''_{z,m}(n_m + n_m^2 + k_m^2))}{k_0|\epsilon_m|^2} \tag{A.13}$$

$$f_8 = \frac{2(\epsilon'_m(k'_x k''_x - k'_{z,m}k''_{z,m}) + \epsilon''_m(k''^2_x + k'^2_{z,m}))}{k_0|\epsilon_m|^2} \tag{A.14}$$

$$\Psi_2(y) = \Theta\left(-y + \frac{d_{beam}}{2}\right)\Theta\left(y + \frac{d_{beam}}{2}\right) \tag{A.15}$$

$$G_2(x,t) = \frac{1}{\tau}\sqrt{\frac{\sigma}{\pi}}\exp\left(-\sigma\frac{(x - v_{g,SPP}(t - t_0)^2)}{2v_{g,SPP}^2\tau^2}\right) \tag{A.16}$$

With Q being either the total source function or the source functions of its components. k_0 is the wave vector of the light, n_m the refractive index of the material, k_m the extinction coefficient of the material. τ is the full-with half-maximum pulse duration and t_0 is the maximum of the beam in time. $\sigma = 4\ln(2)$ is a constant factor. Θ is the Heaviside function, depending on the beam diameter d_{beam}. The beam is assumed to be symmetrical in x- and y-direction. $\epsilon_m = \epsilon'_m + \mathrm{i}\epsilon''_m$ is the complex dielectric function of the metal, with real and imaginary part. $k_x = k'_x + \mathrm{i}k''_x$ is the wave vector of the SPP in x-direction and $k_{z,m} = k'_{z,m} + \mathrm{i}k''_{z,m}$ the wave vector in the metal in z-direction. The factor $v_{g,\mathrm{SPP}}$ is the group velocity of the SPP. β is the SPP coupling efficiency and δ the phase difference of the SPP and the light wave.

Bibliography

[1] J.-H. Klein-Wiele and P. Simon, "Sub-100nm pattern generation by laser direct writing using a confinement layer," *Optics Express*, vol. 21, no. 7, p. 9017, 2013.

[2] L. Mulko, M. Soldera, and A. F. Lasagni, "Structuring and functionalization of non-metallic materials using direct laser interference patterning: A review," 2022.

[3] J. Bonse, S. Hohm, S. V. Kirner, A. Rosenfeld, and J. Kruger, "Laser-Induced Periodic Surface Structures-A Scientific Evergreen," *IEEE Journal of Selected Topics in Quantum Electronics*, vol. 23, no. 3, pp. 109–123, 2017.

[4] M. Birnbaum, "Semiconductor surface damage produced by Ruby lasers," *Journal of Applied Physics*, vol. 36, no. 11, pp. 3688–3689, 1965.

[5] S. S. Kou, G. Yuan, Q. Wang, L. Du, E. Balaur, D. Zhang, D. Tang, B. Abbey, X. C. Yuan, and J. Lin, "On-chip photonic Fourier transform with surface plasmon polaritons," *Light: Science and Applications*, vol. 5, no. September 2015, 2016.

[6] Y. Lin, T. X. Hoang, H. S. Chu, and C. A. Nijhuis, "Directional launching of surface plasmon polaritons by electrically driven aperiodic groove array reflectors," *Nanophotonics*, vol. 10, no. 3, pp. 1145–1154, 2021.

[7] S. Dong, Q. Zhang, G. Cao, J. Ni, T. Shi, S. Li, J. Duan, J. Wang, Y. Li, S. Sun, L. Zhou, G. Hu, and C. W. Qiu, "On-chip trans-dimensional plasmonic router," *Nanophotonics*, vol. 9, no. 10, pp. 3357–3365, 2020.

[8] T. Zang, H. Zang, Z. Xi, J. Du, H. Wang, Y. Lu, and P. Wang, "Asymmetric Excitation of Surface Plasmon Polaritons via Paired Slot Antennas for Angstrom Displacement Sensing," *Physical Review Letters*, vol. 124, no. 24, p. 243901, 2020.

[9] V. Bruno, C. Devault, S. Vezzoli, Z. Kudyshev, T. Huq, S. Mignuzzi, A. Jacassi, S. Saha, Y. D. Shah, S. A. Maier, D. R. Cumming, A. Boltasseva, M. Ferrera, M. Clerici, D. Faccio, R. Sapienza, and V. M. Shalaev, "Negative Refraction in Time-Varying Strongly Coupled Plasmonic-Antenna-Epsilon-Near-Zero Systems," *Physical Review Letters*, vol. 124, no. 4, p. 43902, 2020.

[10] I. Suárez, A. Ferrando, J. Marques-Hueso, A. DIéz, R. Abargues, P. J. Rodríguez-Cantó, and J. P. Martínez-Pastor, "Propagation length enhancement of surface plasmon polaritons in gold nano-/micro-waveguides by the interference with photonic modes in the surrounding active dielectrics," *Nanophotonics*, vol. 6, no. 5, pp. 1109–1120, 2017.

[11] H. C. Zhang, L. P. Zhang, P. H. He, J. Xu, C. Qian, F. J. Garcia-Vidal, and T. J. Cui, "A plasmonic route for the integrated wireless communication of subdiffraction-limited signals," *Light: Science and Applications*, vol. 9, no. 1, 2020.

[12] F. López-Tejeira, S. G. Rodrigo, L. Martín-Moreno, F. J. García-Vidal, E. Devaux, T. W. Ebbesen, J. R. Krenn, I. P. Radko, S. I. Bozhevolnyi, M. U. González, J. C. Weeber, and A. Dereux, "Efficient unidirectional nanoslit couplers for surface plasmons," *Nature Physics*, vol. 3, no. 5, pp. 324–328, 2007.

[13] J. Lin, J. P. Mueller, Q. Wang, G. Yuan, N. Antoniou, X. C. Yuan, and F. Capasso, "Polarization-controlled tunable directional coupling of surface plasmon polaritons," *Science*, vol. 340, no. 6130, pp. 331–334, 2013.

[14] Y. Fang and M. Sun, "Nanoplasmonic waveguides: Towards applications in integrated nanophotonic circuits," *Light: Science and Applications*, vol. 4, no. December 2014, pp. 1–11, 2015.

[15] T. Leißner, C. Lemke, J. Fiutowski, J. W. Radke, A. Klick, L. Tavares, J. Kjelstrup-Hansen, H. G. Rubahn, and M. Bauer, "Morphological tuning of the plasmon dispersion relation in dielectric-loaded nanofiber waveguides," *Physical Review Letters*, vol. 111, no. 4, pp. 1–5, 2013.

[16] S. A. Maier, *Plasmonics: fundamentals and applications*. Springer Science & Business Media, 2007.

[17] N. Bärsch, K. Körber, A. Ostendorf, and K. H. Tönshoff, "Ablation and cutting of planar silicon devices using femtosecond laser pulses," *Applied Physics A: Materials Science and Processing*, vol. 77, no. 2, pp. 237–242, 2003.

[18] A. Happonen, A. Stepanov, H. Piili, and A. Salminen, "Innovation Study for Laser Cutting of Complex Geometries with Paper Materials," *Physics Procedia*, vol. 78, no. August, pp. 128–137, 2015.

[19] P. Singh, A. Pramanik, A. K. Basak, C. Prakash, and V. Mishra, *Developments of non-conventional drilling methods a review.* The International Journal of Advanced Manufacturing Technology, 2020.

[20] C. Wang, Q. Wang, Q. Qian, and B. Di, "The development of laser drilling: A review," *IOP Conference Series: Materials Science and Engineering*, vol. 782, no. 2, 2020.

[21] A. F. Kaplan, J. Frostevarg, T. Ilar, H. S. Bang, and H. S. Bang, "Evolution of a Laser Hybrid Welding Map," *Physics Procedia*, vol. 78, no. August, pp. 2–13, 2015.

[22] J. Bekesi, J. J. Kaakkunen, W. Michaeli, F. Klaiber, M. Schoengart, J. Ihlemann, and P. Simon, "Fast fabrication of super-hydrophobic surfaces on polypropylene by replication of short-pulse laser structured molds," *Applied Physics A: Materials Science and Processing*, vol. 99, no. 4, pp. 691–695, 2010.

[23] A. I. Aguilar-Morales, S. Alamri, B. Voisiat, T. Kunze, and A. F. Lasagni, "The role of the surface nano-roughness on the wettability performance of microstructured metallic surface using direct laser interference patterning," *Materials*, vol. 12, no. 7, pp. 1–14, 2019.

[24] T. Baldacchini, J. E. Carey, M. Zhou, and E. Mazur, "Superhydrophobic Surfaces Prepared by Microstructuring of Silicon Using a Femtosecond Laser," no. 9, pp. 4917–4919, 2006.

[25] S. Storm, S. Alamri, M. Soldera, T. Kunze, and A. F. Lasagni, "How to Tailor Structural Colors for Extended Visibility and White Light Generation Employing Direct Laser Interference Patterning," *Macromolecular Chemistry and Physics*, vol. 220, no. 13, 2019.

[26] K. O. Böker, F. Kleinwort, J. H. Klein-Wiele, P. Simon, K. Jäckle, S. Taheri, W. Lehmann, and A. F. Schilling, "Laser ablated periodic nanostructures on titanium and steel implants influence adhesion and osteogenic differentiation of mesenchymal stem cells," *Materials*, vol. 13, no. 16, pp. 1–16, 2020.

[27] S. Rung, K. Bokan, F. Kleinwort, S. Schwarz, P. Simon, J. H. Klein-Wiele, C. Esen, and R. Hellmann, "Possibilities of dry and lubricated friction modification enabled by different ultrashort laser-based surface structuring methods," *Lubricants*, vol. 7, no. 5, 2019.

[28] M. J. Wood, P. Servio, and A. M. Kietzig, "The tuning of lipss wettability during laser machining and through post-processing," *Nanomaterials*, vol. 11, no. 4, 2021.

[29] O. Varlamova, J. Reif, M. Stolz, R. Borcia, I. D. Borcia, and M. Bestehorn, "Wetting properties of LIPSS structured silicon surfaces," *European Physical Journal B*, vol. 92, no. 5, 2019.

[30] A. Ruiz de la Cruz, R. Lahoz, J. Siegel, G. F. de la Fuente, and J. Solis, "Large area, high speed inscription of laser-induced periodic surface structures (LIPSS) in Cr using a high repetition rate fs-laser," *Optics InfoBase Conference Papers*, vol. 39, no. 8, pp. 2491–2494, 2013.

[31] G. Li, J. Li, Y. Hu, C. Zhang, X. Li, J. Chu, and W. Huang, "Femtosecond laser color marking stainless steel surface with different wavelengths," *Applied Physics A: Materials Science and Processing*, vol. 118, no. 4, pp. 1189–1196, 2015.

[32] E. I. Ageev, V. P. Veiko, E. A. Vlasova, Y. Y. Karlagina, A. Krivonosov, M. K. Moskvin, G. V. Odintsova, V. E. Pshenichnov, V. V. Romanov, and R. M. Yatsuk, "Controlled nanostructures formation on stainless steel by short laser pulses for products protection against falsification," *Optics Express*, vol. 26, no. 2, p. 2117, 2018.

[33] C. Florian, S. V. Kirner, J. Krüger, and J. Bonse, "Surface functionalization by laser-induced periodic surface structures," *Journal of Laser Applications*, vol. 32, no. 2, p. 022063, 2020.

[34] J. Heitz, C. Plamadeala, M. Muck, O. Armbruster, W. Baumgartner, A. Weth, C. Steinwender, H. Blessberger, J. Kellermair, S. V. Kirner, J. Krüger, J. Bonse, A. S. Guntner, and A. W. Hassel, "Femtosecond laser-induced microstructures on Ti substrates for reduced cell adhesion," *Applied Physics A: Materials Science and Processing*, vol. 123, no. 12, pp. 1–9, 2017.

[35] L. Schneider, M. Laustsen, N. Mandsberg, and R. Taboryski, "The Influence of Structure Heights and Opening Angles of Micro-and Nanocones on the Macroscopic Surface Wetting Properties," *Scientific Reports*, vol. 6, no. September 2015, pp. 1–9, 2016.

[36] H. J. Jeon, C. G. Simon, and G. H. Kim, "A mini-review: Cell response to microscale, nanoscale, and hierarchical patterning of surface structure," oct 2014.

[37] H. Ibach and H. Lüth, *Festkörperphysik: Einführung in die Grundlagen*. Springer-Verlag, 2009.

[38] W. Nolting, "Elektrodynamik Grundkurs Theoretische Physik 3 Springer Spektrum ," 2011.

[39] M. Göppert-Mayer, "Über Elementarakte mit zwei Quantensprüngen," *Annalen der Physik*, vol. 401, no. 3, pp. 273–294, 1931.

[40] P. Liu, W. L. Smith, H. Lotem, J. H. Bechtel, N. Bloembergen, and R. S. Adhav, "Absolute two-photon absorption coefficients at 355 and 266 nm," *Physical Review B*, vol. 17, no. 12, pp. 4620–4632, 1978.

[41] A. Dragonmir, J. G. Mcinerney, and D. N. Nikogosyan, "Femtosecond measurements of two-photon absorption coefficients at $\lambda = 264$ nm in glasses, crystals, and liquids," *Applied Optics*, vol. 41, no. 27, p. 5655, 2002.

[42] R. H. Ritchie, "Plasma Losses by Fast Electrons in Thin Films," *Physical Review*, vol. 106, pp. 874–881, jun 1957.

[43] A. Klick, S. de la Cruz, C. Lemke, M. Großmann, H. Beyer, J. Fiutowski, H. G. Rubahn, E. R. Méndez, and M. Bauer, "Amplitude and phase of surface plasmon polaritons excited at a step edge," *Applied Physics B: Lasers and Optics*, vol. 122, no. 4, 2016.

[44] S. T. Koev, A. Agrawal, H. J. Lezec, and V. A. Aksyuk, "An Efficient Large-Area Grating Coupler for Surface Plasmon Polaritons," *Plasmonics*, vol. 7, pp. 269–277, jun 2012.

[45] S. Joseph, S. Sarkar, and J. Joseph, "Grating-Coupled Surface Plasmon-Polariton Sensing at a Flat Metal-Analyte Interface in a Hybrid-Configuration," *ACS applied materials & interfaces*, vol. 12, pp. 46519–46529, oct 2020.

[46] E. Kretschmann, "Die Bestimmung optischer Konstanten von Metallen durch Anregung von Oberflächenplasmaschwingungen," *Zeitschrift für Physik*, vol. 241, no. 4, pp. 313–324, 1971.

[47] A. Otto, "Excitation of nonradiative surface plasma waves in silver by the method of frustrated total reflection," *Zeitschrift für Physik*, vol. 216, no. 4, pp. 398–410, 1968.

[48] J. Oltmanns, P. N. Terekhin, F. Kleinwort, A. Blumenstein, D. S. Ivanov, M. E. Garcia, B. Rethfeld, J. Ihlemann, and P. Simon, "Influence of the Laser Beam Shape on Laser-Induced Periodic Surface Structure Formation Assisted by Surface Plasmon Polaritons," *Journal of Laser Micro Nanoengineering*, vol. 16, no. 3, pp. 199–204, 2021.

[49] P. N. Terekhin, J. Oltmanns, A. Blumenstein, D. S. Ivanov, F. Kleinwort, M. E. Garcia, B. Rethfeld, J. Ihlemann, and P. Simon, "Key role of surface plasmon polaritons in generation of periodic surface structures following single-pulse laser irradiation of a gold step edge," *Nanophotonics*, vol. 11, no. 2, pp. 359–367, 2022.

[50] A. Y. Vorobyev, V. S. Makin, and C. Guo, "Periodic ordering of random surface nanostructures induced by femtosecond laser pulses on metals," *Journal of Applied Physics*, vol. 101, no. 3, 2007.

[51] T. Y. Hwang and C. Guo, "Angular effects of nanostructure-covered femtosecond laser induced periodic surface structures on metals," *Journal of Applied Physics*, vol. 108, no. 7, 2010.

[52] E. L. Gurevich, "On the influence of surface plasmon-polariton waves on pattern formation upon laser ablation," *Applied Surface Science*, vol. 278, pp. 52–56, 2013.

[53] R. D. Murphy, B. Torralva, D. P. Adams, and S. M. Yalisove, "Polarization dependent formation of femtosecond laser-induced periodic surface structures near stepped features," *Applied Physics Letters*, vol. 104, no. 23, pp. 102–107, 2014.

[54] K. Miyazaki, G. Miyaji, and T. Inoue, "Nanograting formation on metals in air with interfering femtosecond laser pulses," *Applied Physics Letters*, vol. 107, p. 071103, aug 2015.

[55] S. Maragkaki, T. J. Derrien, Y. Levy, N. M. Bulgakova, A. Ostendorf, and E. L. Gurevich, "Wavelength dependence of picosecond laser-induced periodic surface structures on copper," *Applied Surface Science*, vol. 417, pp. 88–92, 2017.

[56] J. Wang and C. Guo, "Formation of extraordinarily uniform periodic structures on metals induced by femtosecond laser pulses," *Journal of Applied Physics*, vol. 100, no. 2, pp. 1–5, 2006.

[57] A. Y. Vorobyev and C. Guo, "Colorizing metals with femtosecond laser pulses," vol. 041914, no. December 2007, pp. 1–4, 2015.

[58] A. Y. Vorobyev and C. Guo, "Femtosecond laser-induced periodic surface structure formation on tungsten," *Journal of Applied Physics*, vol. 104, no. 6, 2008.

[59] J. P. Colombier, A. Rudenko, E. Silaeva, H. Zhang, X. Sedao, E. Bévillon, S. Reynaud, C. Maurice, F. Pigeon, F. Garrelie, and R. Stoian, "Mixing periodic topographies and structural patterns on silicon surfaces mediated by ultrafast photoexcited charge carriers," *Physical Review Research*, vol. 2, no. 4, pp. 1–15, 2020.

[60] J. Bosne and J. Krüger, "Pulse number dependence of laser-induced periodic surface structures for femtosecond laser irradiation of silicon," vol. 034903, no. May 2010, 2010.

[61] J. Reif, O. Varlamova, S. Uhlig, S. Varlamov, and M. Bestehorn, "On the physics of self-organized nanostructure formation upon femtosecond laser ablation," *Applied Physics A: Materials Science and Processing*, vol. 117, no. 1, pp. 179–184, 2014.

[62] J. Liu, T. Jia, H. Zhao, and Y. Huang, "Two-photon excitation of surface plasmon and the period-increasing effect of low spatial frequency ripples on a GaP crystal in air/water," *Journal of Physics D: Applied Physics*, vol. 49, no. 43, 2016.

[63] D. Dufft, A. Rosenfeld, S. K. Das, R. Grunwald, and J. Bonse, "Femtosecond laser-induced periodic surface structures revisited: A comparative study on ZnO," *Journal of Applied Physics*, vol. 105, no. 3, 2009.

[64] J. Bonse, J. Krüger, S. Höhm, and A. Rosenfeld, "Femtosecond laser-induced periodic surface structures," vol. 042006, no. April, 2012.

[65] K. Bischoff, P. Quigley, A. Hohnholz, P. Jäschke, and S. Kaierle, "Generation of laser-induced periodic surface structures on different glasses by a picosecond-pulsed laser," *Procedia CIRP*, vol. 94, pp. 924–929, 2020.

[66] M. Huang, F. Zhao, Y. Cheng, N. Xu, and Z. Xu, "Origin of laser-induced near-subwavelength ripples: Interference between surface plasmons and incident laser," *ACS Nano*, vol. 3, no. 12, pp. 4062–4070, 2009.

[67] S. K. Das, H. Messaoudi, A. Debroy, E. McGlynn, and R. Grunwald, "Multi-photon excitation of surface plasmon-polaritons and scaling of nanoripple formation in large bandgap materials," *Optical Materials Express*, vol. 3, no. 10, p. 1705, 2013.

[68] F. Garrelie, J.-P. Colombier, F. Pigeon, S. Tonchev, N. Faure, M. Bounhalli, S. Reynaud, and O. Parriaux, "Evidence of surface plasmon resonance in ultrafast laser-induced ripples," *Optics Express*, vol. 19, no. 10, p. 9035, 2011.

[69] J. Bonse and S. Gräf, "Maxwell Meets Marangoni A Review of Theories on Laser Induced Periodic Surface Structures," *Laser and Photonics Reviews*, vol. 14, no. 10, pp. 1–25, 2020.

[70] P. N. Terekhin, O. Benhayoun, S. T. Weber, D. S. Ivanov, M. E. Garcia, and B. Rethfeld, "Influence of surface plasmon polaritons on laser energy absorption and structuring of surfaces," *Applied Surface Science*, vol. 512, no. 3, pp. 1–20, 2020.

[71] E. Sani and A. Dell'Oro, "Spectral optical constants of ethanol and isopropanol from ultraviolet to far infrared," *Optical Materials*, vol. 60, pp. 137–141, oct 2016.

[72] R. L. Olmon, B. Slovick, T. W. Johnson, D. Shelton, S. H. Oh, G. D. Boreman, and M. B. Raschke, "Optical dielectric function of gold," *Physical Review B - Condensed Matter and Materials Physics*, vol. 86, no. 23, pp. 1–9, 2012.

[73] T. J. Derrien, R. Koter, J. Krüger, S. Höhm, A. Rosenfeld, and J. Bonse, "Plasmonic formation mechanism of periodic 100-nm-structures upon femtosecond laser irradiation of silicon in water," *Journal of Applied Physics*, vol. 116, no. 7, 2014.

[74] J. E. Sipe, J. F. Young, J. S. Preston, and H. M. Van Driel, "Laser induced periodic surface structures. I. Theory," *Physical Review B*, vol. 27, no. 2, p. 1141, 1983.

[75] S. Gräf, C. Kunz, and F. A. Müller, "Formation and properties of laser-induced periodic surface structures on different glasses," *Materials*, vol. 10, no. 8, 2017.

[76] A. Rudenko, C. Mauclair, F. Garrelie, and R. Stoian, "Self-organization of surfaces on the nanoscale by topography-mediated selection of quasi- cylindrical and plasmonic waves," vol. 8, no. 3, pp. 459–465, 2019.

[77] E. V. Golosov, A. A. Ionin, S. I. Kudryashov, A. E. Ligachev, S. V. Makarov, L. V. Seleznev, and D. V. Sinitsyn, "Formation of Periodic Nanostructures on Aluminum Surface by Femtosecond Laser Pulses," vol. 6, pp. 237–243, 2011.

[78] S. Sakabe, M. Hashida, S. Tokita, S. Namba, and K. Okamuro, "Mechanism for self-formation of periodic grating structures on a metal surface by a femtosecond laser pulse," *Physical Review B - Condensed Matter and Materials Physics*, vol. 79, no. 3, pp. 1–4, 2009.

[79] K. Okamuro, M. Hashida, Y. Miyasaka, Y. Ikuta, S. Tokita, and S. Sakabe, "Laser fluence dependence of periodic grating structures formed on metal surfaces under femtosecond laser pulse irradiation," *Physical Review B - Condensed Matter and Materials Physics*, vol. 82, no. 16, pp. 1–5, 2010.

[80] T. Tomita, R. Kumai, S. Matsuo, S. Hashimoto, and M. Yamaguchi, "Cross-sectional morphological profiles of ripples on Si, SiC, and HOPG," *Applied Physics A: Materials Science and Processing*, vol. 97, no. 2, pp. 271–276, 2009.

[81] M. Hörstmann-Jungemann, "Nano- and Microstructuring of SiO2 and Sapphire with Fs-laser Induced Selective Etching," *Journal of Laser Micro/Nanoengineering*, vol. 4, no. 2, pp. 135–140, 2009.

[82] F. Liang, R. Vallée, and S. L. Chin, "Physical evolution of nanograting inscription on the surface of fused silica," *Optical Materials Express*, vol. 2, no. 7, p. 900, 2012.

[83] J. Koch, S. Taschner, O. Suttmann, and S. Kaierle, "Surface functionalization under water using picosecond and femtosecond laser pulses - first observations and novel effects," *Procedia CIRP*, vol. 74, pp. 381–385, 2018.

[84] N. A. Smirnov, S. I. Kudryashov, P. A. Danilov, A. A. Nastulyavichus, A. A. Rudenko, A. A. Ionin, A. A. Kuchmizhak, and O. B. Vitrik, "Femtosecond laser ablation of a thin silver film in air and water," *Optical and Quantum Electronics*, vol. 52, no. 2, pp. 2717–2722, 2020.

[85] D. S. Ivanov, A. Blumenstein, J. Ihlemann, P. Simon, M. E. Garcia, and B. Rethfeld, "Molecular dynamics modeling of periodic nanostructuring of metals with a short UV laser pulse under spatial confinement by a water layer," *Applied Physics A: Materials Science and Processing*, vol. 123, no. 12, pp. 1–10, 2017.

[86] M. Trtica, J. Stasic, D. Batani, R. Benocci, V. Narayanan, and J. Ciganovic, "Laser-assisted surface modification of Ti-implant in air and water environment," *Applied Surface Science*, vol. 428, pp. 669–675, jan 2018.

[87] C. Y. Shih, I. Gnilitskyi, M. V. Shugaev, E. Skoulas, E. Stratakis, and L. V. Zhigilei, "Effect of a liquid environment on single-pulse generation of laser induced periodic surface structures and nanoparticles," *Nanoscale*, vol. 12, no. 14, pp. 7674–7687, 2020.

[88] O. S. Heavens, "Optical properties of thin films," *Reports on Progress in Physics*, vol. 23, p. 1, jan 1960.

[89] N. N. Nedialkov, S. E. Imamova, and P. A. Atanasov, "Ablation of metals by ultrashort laser pulses," *Journal of Physics D: Applied Physics*, vol. 37, no. 4, pp. 638–643, 2004.

[90] M. Hashida, A. F. Semerok, O. Gobert, G. Petite, Y. Izawa, and J. F. Wagner, "Ablation threshold dependence on pulse duration for copper," *Applied Surface Science*, vol. 197-198, pp. 862–867, 2002.

[91] D. Ivanov and L. Zhigilei, "Combined atomistic-continuum modeling of short-pulse laser melting and disintegration of metal films," *Physical Review B - Condensed Matter and Materials Physics*, vol. 68, no. 6, pp. 1–22, 2003.

[92] J. Wang and C. Guo, "Numerical study of ultrafast dynamics of femtosecond laser-induced periodic surface structure formation on noble metals," *Journal of Applied Physics*, vol. 102, no. 5, 2007.

[93] B. N. Chichkov, C. Momma, S. Nolte, F. Alvensleben, and A. Tünnermann, "Femtosecond, picosecond and nanosecond laser ablation of solids," *Applied Physics A Materials Science & Processing*, vol. 63, pp. 109–115, aug 1996.

[94] M. V. Shugaev, I. Gnilitskyi, N. M. Bulgakova, and L. V. Zhigilei, "Mechanism of single-pulse ablative generation of laser-induced periodic surface structures," *Physical Review B*, vol. 96, no. 20, pp. 1–9, 2017.

[95] D. S. Ivanov, V. P. Lipp, A. Blumenstein, F. Kleinwort, V. P. Veiko, E. Yakovlev, V. Roddatis, M. E. Garcia, B. Rethfeld, J. Ihlemann, and P. Simon, "Experimental and Theoretical Investigation of Periodic Nanostructuring of Au with Ultrashort UV Laser Pulses near the Damage Threshold," *Physical Review Applied*, vol. 4, no. 6, pp. 1–14, 2015.

[96] A. Blumenstein, M. E. Garcia, B. Rethfeld, P. Simon, J. Ihlemann, and D. S. Ivanov, "Formation of periodic nanoridge patterns by ultrashort single pulse UV laser irradiation of gold," *Nanomaterials*, vol. 10, no. 10, pp. 1–14, 2020.

[97] J. J. Kaakkunen, M. Silvennoinen, K. Paivasaari, and P. Vahimaa, "Water-assisted femtosecond laser pulse ablation of high aspect ratio holes," *Physics Procedia*, vol. 12, no. PART 2, pp. 89–93, 2011.

[98] N. A. Smirnov, S. I. Kudryashov, A. A. Rudenko, A. A. Nastulyavichus, and A. A. Ionin, "Ablation efficiency of gold at fs/ps laser treatment in water and air," *Laser Physics Letters*, vol. 19, p. 026001, jan 2022.

[99] M. Spellauge, C. Doñate-Buendía, S. Barcikowski, B. Gökce, and H. P. Huber, "Comparison of ultrashort pulse ablation of gold in air and water by time-resolved experiments," *Light: Science and Applications*, vol. 11, no. 1, 2022.

[100] C. B. Schaffer, N. Nishimura, E. N. Glezer, A. M.-T. Kim, and E. Mazur, "Dynamics of femtosecond laser-induced breakdown in water from femtoseconds to microseconds," *Optics Express*, vol. 10, no. 3, p. 196, 2002.

[101] J. Zhang, J. Claverie, M. Chaker, and D. Ma, "Colloidal Metal Nanoparticles Prepared by Laser Ablation and their Applications," *ChemPhysChem*, vol. 18, no. 9, pp. 986–1006, 2017.

[102] E. Fazio, B. Gökce, A. De Giacomo, M. Meneghetti, G. Compagnini, M. Tommasini, F. Waag, A. Lucotti, C. G. Zanchi, P. M. Ossi, M. Dell'Aglio, L. D'Urso, M. Condorelli, V. Scardaci, F. Biscaglia, L. Litti, M. Gobbo, G. Gallo, M. Santoro, S. Trusso, and F. Neri, "Nanoparticles Engineering by Pulsed Laser Ablation in Liquids: Concepts and Applications," *Nanomaterials*, vol. 10, p. 2317, nov 2020.

[103] V. Amendola and M. Meneghetti, "Laser ablation synthesis in solution and size manipulation of noble metal nanoparticles," *Physical Chemistry Chemical Physics*, vol. 11, no. 20, pp. 3805–3821, 2009.

[104] R. Trebino, *Frequency-Resolved Optical Gating: The Measurement of Ultrashort Laser Pulses: The Measurement of Ultrashort Laser Pulses*. Springer Science & Business Media, 2000.

[105] B. Rethfeld, D. S. Ivanov, M. E. Garcia, and S. I. Anisimov, "Modelling ultrafast laser ablation," *Journal of Physics D: Applied Physics*, vol. 50, no. 19, 2017.

[106] B. J. Alder and T. E. Wainwright, "Studies in molecular dynamics. I. General method," *The Journal of Chemical Physics*, vol. 31, no. 2, pp. 459–466, 1959.

[107] C. L. Kelchner, S. J. Plimpton, and J. C. Hamilton, "Dislocation nucleation and defect structure during surface indentation," *Physical Review B*, vol. 58, pp. 11085–11088, nov 1998.

[108] D. S. Ivanov, B. Rethfeld, G. M. O'Connor, T. J. Glynn, A. N. Volkov, and L. V. Zhigilei, "The mechanism of nanobump formation in femtosecond pulse laser nanostructuring of thin metal films," *Applied Physics A: Materials Science and Processing*, vol. 92, no. 4, pp. 791–796, 2008.

[109] C. Bischoff, F. Völklein, J. Schmitt, U. Rädel, U. Umhofer, E. Jäger, and A. F. Lasagni, "Design and manufacturing method of fundamental beam mode shaper for adapted laser beam profile in laser material processing," *Materials*, vol. 12, no. 14, pp. 1–13, 2019.

[110] G. M. Hale and M. R. Querry, "Optical Constants of Water in the 200-nm to 200-μm Wavelength Region," *Applied Optics*, vol. 12, no. 3, p. 555, 1973.

[111] D. N. Nikogosyan, A. A. Oraevsky, and V. I. Rupasov, "Two-photon ionization and dissociation of liquid water by powerful laser UV radiation," *Chemical Physics*, vol. 77, no. 1, pp. 131–143, 1983.

[112] J. Glinski, G. Chavepeyer, J. Platten, and P. Smet, "Surface properties of diluted aqueous solutions of normal short-chained alcohols," *The Journal of Chemical Physics*, vol. 109, pp. 5050–5053, 09 1998.

[113] M. Spellauge, C. Doñate-buendía, and S. Barcikowski, "Ultrafast pump-probe microscopy reveals the influence of a water layer on the early stage ablation dynamics of gold," pp. 2–6, 2021.

[114] S. Dittrich, M. Spellauge, S. Barcikowski, H. P. Huber, and B. Gökce, "Time resolved studies reveal the origin of the unparalleled high efficiency of one nanosecond laser ablation in liquids," *Opto-Electronic Advances*, vol. 5, no. 6, pp. 1–11, 2022.

[115] S. V. Starinskiy, Y. G. Shukhov, and A. V. Bulgakov, "Laser-induced damage thresholds of gold, silver and their alloys in air and water," *Applied Surface Science*, vol. 396, pp. 1765–1774, 2017.

[116] D. Du, X. Liu, G. Korn, J. Squier, and G. Mourou, "Laser-induced breakdown by impact ionization in SiO2 with pulse widths from 7 ns to 150 fs," *Applied Physics Letters*, vol. 64, no. 23, pp. 3071–3073, 1994.

[117] A. Vogel, J. Noack, K. Nahen, D. Theisen, S. Busch, U. Parlitz, D. X. Hammer, G. D. Noojin, B. A. Rockwell, and R. Birngruber, "Energy balance of optical breakdown in water at nanosecond to femtosecond time scales," *Applied Physics B: Lasers and Optics*, vol. 68, no. 2, pp. 271–280, 1999.

[118] E. V. Barmina, M. Barberoglou, V. Zorba, A. V. Simakin, E. Stratakis, C. Fotakis, and G. A. Shafeev, "Laser control of the properties of nanostructures on Ta and Ni under their ablation in liquids," *Journal of Optoelectronics and Advanced Materials*, vol. 12, no. 3, pp. 496–499, 2010.

[119] X. Y. Chen, J. Lin, J. M. Liu, and Z. G. Liu, "Formation and evolution of self-organized hexagonal patterns on silicon surface by laser irradiation in water," *Applied Physics A: Materials Science and Processing*, vol. 94, no. 3, pp. 649–656, 2009.

[120] H. W. Kang and A. J. Welch, "Enhanced coupling of optical energy during liquid-confined metal ablation," *Journal of Applied Physics*, vol. 118, no. 15, 2015.

[121] S. Bashir, M. S. Rafique, A. A. Ajami, C. S. Nathala, W. Husinsky, and K. Whitmore, "Femtosecond laser ablation of Zn in air and ethanol: effect of fluence on the surface morphology, ablated area, ablation rate and hardness," *Applied Physics A: Materials Science and Processing*, vol. 127, no. 4, 2021.

[122] L. Jiang, A. D. Wang, B. Li, T. H. Cui, and Y. F. Lu, "Electrons dynamics control by shaping femtosecond laser pulses in micro/nanofabrication: Modeling, method, measurement and application," *Light: Science and Applications*, vol. 7, no. 2, pp. 1–27, 2018.

[123] C. A. Zuhlke, G. D. Tsibidis, T. Anderson, E. Stratakis, G. Gogos, and D. R. Alexander, "Investigation of femtosecond laser induced ripple formation on copper for varying incident angle," *AIP Advances*, vol. 8, no. 1, 2018.

[124] R. Stoian and J. P. Colombier, "Advances in ultrafast laser structuring of materials at the nanoscale," *Nanophotonics*, vol. 9, no. 16, pp. 4665–4688, 2020.

[125] J. Huang, L. Jiang, X. Li, A. Wang, Z. Wang, Q. Wang, J. Hu, L. Qu, T. Cui, and Y. Lu, "Fabrication of highly homogeneous and controllable nanogratings on silicon via chemical etching-assisted femtosecond laser modification," *Nanophotonics*, vol. 8, no. 5, pp. 869–878, 2019.

[126] H. Zhang, J. P. Colombier, and S. Witte, "Laser-induced periodic surface structures: Arbitrary angles of incidence and polarization states," *Physical Review B*, vol. 101, no. 24, pp. 1–15, 2020.

[127] A. Y. Vorobyev, V. S. Makin, and C. Guo, "Brighter light sources from black metal: Significant increase in emission efficiency of incandescent light sources," *Physical Review Letters*, vol. 102, no. 23, pp. 1–4, 2009.

[128] Y. Liu, Y. Brelet, Z. He, L. Yu, S. Mitryukovskiy, A. Houard, B. Forestier, A. Couairon, and A. Mysyrowicz, "Ciliary white light: Optical aspect of ultrashort laser ablation on transparent dielectrics," *Physical Review Letters*, vol. 110, no. 9, pp. 1–5, 2013.

[129] X. Wang, Y. Deng, Q. Li, Y. Huang, Z. Gong, K. B. Tom, and J. Yao, "Excitation and propagation of surface plasmon polaritons on a non-structured surface with a permittivity gradient," *Light: Science and Applications*, vol. 5, no. 12, pp. 1–6, 2016.

[130] T. Zou, B. Zhao, W. Xin, Y. Wang, B. Wang, X. Zheng, H. Xie, Z. Zhang, J. Yang, and C. L. Guo, "High-speed femtosecond laser plasmonic lithography and reduction of graphene oxide for anisotropic photoresponse," *Light: Science and Applications*, vol. 9, no. 1, 2020.

[131] R. D. Murphy, B. Torralva, D. P. Adams, and S. M. Yalisove, "Laser-induced periodic surface structure formation resulting from single-pulse ultrafast irradiation of Au microstructures on a Si substrate," *Applied Physics Letters*, vol. 102, no. 21, 2013.

[132] E. L. Gurevich and S. V. Gurevich, "Laser Induced Periodic Surface Structures induced by surface plasmons coupled via roughness," *Applied Surface Science*, vol. 302, pp. 118–123, 2014.

[133] N. Ackerl and K. Wegener, "Observation of single ultrashort laser pulse generated periodic surface structures on linelike defects," *Journal of Laser Applications*, vol. 32, no. 2, p. 022049, 2020.

[134] Y. Chen, T. Luo, C. Ma, W. Huang, and S. Gao, "Spectral analysis of irregular roughness artifacts measured by atomic force microscopy and laser scanning microscopy," *Microscopy and Microanalysis*, vol. 20, no. 6, pp. 1682–1691, 2014.

[135] P. B. Johnson and R. W. Christy, "Optical Constant of the Nobel Metals," *Physical Review B*, vol. 6, no. 12, pp. 4370–4379, 1972.

[136] A. Blumenstein, E. S. Zijlstra, D. S. Ivanov, S. T. Weber, T. Zier, F. Kleinwort, B. Rethfeld, J. Ihlemann, P. Simon, and M. E. Garcia, "Transient optics of gold during laser irradiation: From first principles to experiment," *Physical Review B*, vol. 101, no. 16, pp. 1–9, 2020.

[137] H. Wang, J. Jürgensen, P. Decker, Z. Hu, K. Yan, E. L. Gurevich, and A. Ostendorf, "Corrosion behavior of NiTi alloy subjected to femtosecond laser shock peening without protective coating in air environment," *Applied Surface Science*, vol. 501, p. 144338, jan 2020.

[138] I. Gnilitskyi, T. J. Derrien, Y. Levy, N. M. Bulgakova, T. Mocek, and L. Orazi, "High-speed manufacturing of highly regular femtosecond laser-induced periodic surface structures: Physical origin of regularity," *Scientific Reports*, vol. 7, dec 2017.

Danksagungen

Viele Leute haben zu dieser Arbeit beigetragen und ihnen allen gebührt Dank.
Zuallererst möchte ich Dr. Peter Simon danken, der als Abteilungsleiter und Teil der Betreuungsausschuss immer für Hilfe und Tipps zur Verfügung stand und die Arbeit korrekturgelesen hat. Im gleichen Atemzug möchte ich danken Dr. Jürgen Ihlemann der ebenfalls immer mit Rat zur Seite stand und die Arbeit ebenfalls korrekturgelesen hat.

Den gegenwärtigen und früheren Mitarbeitern der Abteilung Kurze Pulse / Nanostrukturen möchte ich ebenfalls danken sowie dem gesamten IFNANO und besonders herausheben möchte ich Frederik Kleinwort, der im Labor immer eine große Hilfe war.

Des weiteren möchte ich den Mitarbeitern am DFG-Projekt aus Kassel und Kaiserslautern danken, besonders zu nennen sind hier Dr. Pavel Terekhin und Dr. Dmitry Ivanov.

Ebenfalls möchte ich Prof Egner danken, für die Betreuung der Arbeit und das er als Referent für die Arbeit fungiert.
Auch dem Rest der Prüfungskommission möchte ich danken, namentlich Prof. Roper, Prof. Mathias und Prof. Rizzi. Besonderer Dank gilt Prof. Hofsäss danken, der sich bereit erklärt hat Korreferent zu sein.

Zu guter Letzt will ich auch noch meiner Familie und meinen Freunden danken, die immer ein offenes Ohr hatten und häufig eine willkommene Ablenkung waren. Hier möchte ich auch meine Eltern Alfred und Else, sowie meine Schwester Anke namentlich erwähnen.